



HAL
open science

Statistical shape analysis of the anatomical variability of the human hippocampus in large populations.

Claire Cury

► **To cite this version:**

Claire Cury. Statistical shape analysis of the anatomical variability of the human hippocampus in large populations.. *Neurons and Cognition [q-bio.NC]*. Université Pierre et Marie Curie - Paris VI, 2015. English. NNT: 2015PA066021 . tel-01133165

HAL Id: tel-01133165

<https://theses.hal.science/tel-01133165>

Submitted on 18 Mar 2015

HAL is a multi-disciplinary open access archive for the deposit and dissemination of scientific research documents, whether they are published or not. The documents may come from teaching and research institutions in France or abroad, or from public or private research centers.

L'archive ouverte pluridisciplinaire **HAL**, est destinée au dépôt et à la diffusion de documents scientifiques de niveau recherche, publiés ou non, émanant des établissements d'enseignement et de recherche français ou étrangers, des laboratoires publics ou privés.

**THÈSE DE DOCTORAT DE
L'UNIVERSITÉ PIERRE ET MARIE CURIE**

Spécialité

Neurosciences

École Doctorale Cerveau, Cognition, Comportement (ED3C)

Présentée par

Claire CURY

**Analyse statistique de la variabilité anatomique de
l'hippocampe à partir de grandes populations.**

soutenue le 12 Février 2015

Membres du jury

Dr. Arnaud CACHIA	Rapporteur
Dr. Olivier COULON	Rapporteur
Dr. Habib BENALI	Examineur
Dr. Jean-François MANGIN	Examineur
Dr. Roberto TORO	Membre invité
Dr. Joan Alexis GLAUNÈS	Co-encadrant
Dr. Olivier COLLIOT	Directeur de thèse

CONTENTS

Contents	3
Résumé français	1
1 Introduction	13
I Background	21
2 The human hippocampus	23
2.1 Anatomy, development and variability	24
2.1.1 Terminology	24
2.1.2 Spatial localisation	25
2.1.3 Anatomy	27
2.1.4 Development	30
2.1.5 Incomplete hippocampal inversion	35
2.2 Visualisation in MRI	38
2.3 Role	41
2.3.1 Memory	42
2.3.2 Spatial navigation	45
2.3.3 Pathologies	46
2.4 Conclusion	50
3 Computational anatomy	51
3.1 Shapes and their numerical representation in medical imaging	53

3.1.1	Data acquisition	53
3.1.2	Segmentation	54
3.2	Shape descriptors and dissimilarity	55
3.2.1	Common shape descriptors	56
3.2.2	Deformation-based descriptors	59
3.3	Chosen mathematical model	61
3.3.1	Currents	62
3.3.2	LDDMM framework	67
	3.3.2.1 Large Diffeomorphic Deformations.	67
	3.3.2.2 Geodesic equations and local encoding.	70
3.4	Statistical shape analysis	71
3.4.1	Geometry based methods	72
	3.4.1.1 Distance matrix approximation	72
3.4.2	Principal component analysis on initial momentum vectors	74
3.5	Template estimation	75
3.6	Conclusion	78

II Contributions 81

4	Evaluation of Incomplete Hippocampal Inversions	83
4.1	Introduction	84
	4.1.1 Review of the Incomplete Hippocampal Inversion	86
	4.1.2 Criteria used in the literature	89
4.2	Participants and MRI data	92
4.3	Simplified individual criteria and global criterion for IHI assesment	93
	4.3.1 Criterion <i>C1</i> : verticality and roundness of the hippocampus body	93
	4.3.1.1 Description	93
	4.3.1.2 Examples	95
	4.3.2 Criterion <i>C2</i> : collateral sulcus	97
	4.3.2.1 Description	97
	4.3.2.2 Examples	100
	4.3.3 Criterion <i>C3</i> : medial positioning	101
	4.3.3.1 Description	101
	4.3.3.2 Examples	102
	4.3.4 Criterion <i>C4</i> : subiculum	103
	4.3.4.1 Description	103
	4.3.4.2 Examples	104

4.3.5	Criterion C_5 : sulci of the fusiform gyrus (T4)	104
4.3.5.1	Description	104
4.3.5.2	Examples	105
4.3.6	Global criterion C_0	105
4.4	Hippocampus segmentation	106
4.5	Experiments	107
4.5.1	Java application	107
4.5.2	IHI assesment	109
4.5.3	Intra- and inter-observer reproducibility	109
4.5.4	Statistical analysis	110
4.6	Results	110
4.6.1	Intra- and inter-observer reproducibility	110
4.6.2	Global criterion C_0	111
4.6.3	Individual criteria	113
4.6.4	Impact of IHI on the automatic segmentation	115
4.7	Discussion and conclusion	117
5	Diffeomorphic iterative centroid method for template estimation on large datasets	121
5.1	Introduction	122
5.2	An Iterative Centroid method	125
5.2.1	Mathematical justification	126
5.2.2	Diffeomorphic Centroid methods	128
5.2.2.1	Direct iterative centroid	129
5.2.2.2	Centroid with averaging in the space of current	130
5.2.2.3	A pairwise centroid	131
5.2.3	Implementation	132
5.3	Results	135
5.3.1	Data	135
5.3.2	Effect of subject ordering	137
5.3.3	Position of the centroids within the population	141
5.3.4	Effects of initialization on estimated variational template	142
5.3.5	Effect of the number of iterations for Iterative Centroids	145
5.3.6	Computation time	146
5.4	Discussion	147
6	Statistical shape analysis using diffeomorphic iterative centroids	151
6.1	Introduction	152
6.2	Evaluation of iterative centroids	153

6.2.1	Statistical Analysis	153
6.2.1.1	Principal Component Analysis on initial momentum vectors	153
6.2.1.2	Distance matrix approximation	154
6.2.2	Data	155
6.2.3	Experiments	157
6.2.4	Synthetic dataset SD	158
6.2.4.1	Computation time	158
6.2.4.2	Centring of the centres	159
6.2.4.3	PCA	161
6.2.4.4	Distance matrices	161
6.2.5	The real dataset RD50	164
6.2.5.1	Computation time	165
6.2.5.2	Centring of the centres	165
6.2.5.3	PCA	167
6.2.5.4	Distance matrices	170
6.3	Variability analysis and prediction of IHI	173
6.3.1	Centroid estimation	173
6.3.2	Prediction of IHI using shape analysis	176
6.4	Discussion and conclusion	180
7	Shape analysis applied to the Alzheimer's disease	183
7.1	Dataset and experiments	184
7.2	Results: analysis of variability	185
7.3	Results: prediction of clinical variables	189
7.4	Conclusion	192
8	Conclusion and discussion	195
	List of Figures	200
	List of Tables	207
	Bibliography	211

RÉSUMÉ FRANÇAIS

introduction L'analyse statistique de la forme des structures anatomiques est un enjeu essentiel pour de nombreuses applications : modélisation de la variabilité normale et pathologique, prédiction de paramètres cliniques et biologiques à partir de données anatomiques. Ces dernières années ont vu l'émergence de grandes bases de données en neuroimagerie, offrant une puissance statistique considérablement accrue.

Cette thèse a pour thème l'étude statistique de la variabilité anatomique de l'hippocampe à partir de grandes bases de données. Après un état de l'art, la première partie de la thèse porte sur l'étude d'une variante anatomique appelée inversion incomplète de l'hippocampe (IHI). Pour ce faire, nous avons mis au point une échelle de cotation des inversions incomplètes de l'hippocampe (IHI). Elle a été ensuite appliquée à 2000 sujets sains jeunes de la base données multicentrique IMAGEN. C'est la première fois que ces variants anatomiques sont étudiés sur une grande population de sujets sains.

La seconde partie de la thèse porte sur la mise au point d'une méthode d'analyse statistique de formes utilisant les grandes déformations difféomorphiques et les courants mathématiques, qui soit utilisable pour l'analyse de grandes bases de données. Nous avons en particulier introduit une nouvelle approche rapide pour construire des prototypes anatomiques. Cette approche a été validée sur 1000 sujets sains jeunes de la base de données IMAGEN et environ 300 sujets (sujets sains âgés et patients atteints de maladie d'Alzheimer) de la base de données ADNI.

Chapitre 2 : présentation de l'hippocampe L'hippocampe est une structure du cerveau bilatérale située dans le lobe temporal, dont la forme a d'abord évoqué une virgule avant d'être comparée à un hippocampe en 1587 par un anatomiste italien (G C Aranzio). La tête (la partie renflée) est suivie d'un corps allongé (le corps) et d'une extrémité dentée (la queue). Il est composé de 2 lames de cortex enroulées l'une sur l'autre, la Corne d'Ammon et le Gyrus Denté, séparés par le sillon hippocampique. L'hippocampe appartient au système limbique, véritable interface entre le tronc cérébral et le neocortex. Les informations neuronales circulent entre le cortex entorhinal et le neocortex et vice versa (circuit de Papez) et sont impliquées dans les processus de mémorisation.

Lors du développement embryonnaire, l'hippocampe commence à être différencié aux alentours de la 10ème semaine d'aménorrhée (SA) pour certains. A 30 SA l'hippocampe est pratiquement comme chez l'adulte. Pendant la gestation, l'hippocampe va s'inverser c'est à dire que la corne d'Ammon et le gyrus denté vont s'enrouler l'un autour de l'autre, pour former comme deux "U" emboîtés. Cette inversion n'est en réalité pas toujours complète, ce qui amène à un variant anatomique appelé inversion

incomplète de l'hippocampe. Ce variant anatomique à été fréquemment observé chez des patients épileptiques mais aussi chez des sujets non épileptiques. Cette inversion incomplète est retrouvée plus généralement chez les hippocampes gauches.

Les techniques d'imagerie par résonnance magnétique (IRM) permettent de constituer de grandes bases de données et d'observer l'hippocampe in vivo grâce notamment à des séquences 3D pondérées en T1.

La fonction de l'hippocampe est essentielle dans les mécanismes de la mémoire et pour la localisation spatiale. Des études sur des patients ayant subi une ablation des hippocampes ont montré que l'hippocampe serait alors impliqué dans la création de nouveaux souvenirs et dans la mémoire épisodique.

On retrouve l'hippocampe impliqué dans des pathologies comme la maladie d'Alzheimer dont il est l'une des premières structures à être atteinte par atrophie ; l'épilepsie dont il peut être le foyer des crises dans le cas des épilepsies du lobe temporal ; et la dépression pour laquelle son volume serait un facteur de risque tout comme pour les patients atteints de schizophrénie.

Chapitre 3 : l'anatomie numérique Une fois la forme globale de l'hippocampe décrite, nous allons nous intéresser à la variabilité de sa forme, afin de pouvoir différencier les formes correspondant à un sujet normal de celles correspondant à une pathologie ou de pouvoir étudier les variations anatomiques de la structure étudiée. Il faut avant tout définir ce qu'est une forme. En effet ce terme est assez mal défini et pour analyser la forme nous avons besoin d'un descripteur de forme et d'une mesure de dissimilarité qui dans certains cas découle du descripteur ; il faut trouver un équilibre entre la capacité du descripteur à garder l'information de la forme et une mesure

de dissimilarité proche d'une vraie distance invariante par transformations rigides. Ici une forme est le contour d'un objet 2D ou 3D représenté par un masque binaire ou par des points 2D ou 3D. Pour obtenir notre forme, il faut isoler la structure de l'hippocampe du reste du cerveau, par segmentation pour ainsi obtenir un masque binaire 3D que l'on convertit en maillage 3D. Il faut ensuite choisir un descripteur permettant de décrire la forme. Plusieurs choix de modèle sont possibles, et nous avons choisi de travailler dans le cadre des grandes déformations diffeomorphiques (LDDMM), déjà utilisées dans de nombreux travaux de recherche pour l'étude de la variabilité des structures cérébrales car les déformations sont des diffeomorphismes qui permettent de prendre en compte des formes assez différentes tout en respectant l'organisation de la structure et en captant des variations locales non linéaires. L'inconvénient d'utiliser de telles déformations est que la phase d'optimisation est très coûteuse en terme de temps de calcul. Pour représenter nos formes d'hippocampe nous avons choisi d'utiliser les « courants », objet mathématique qui sert à modéliser des objets géométriques sans correspondance point à point. Les formes ainsi décrites ont l'avantage de se trouver dans un espace vectoriel, qui permet alors d'additionner ou soustraire des formes entre elles. Glaunès et al. ont introduit cet objet mathématique pour l'analyse anatomique numérique en 2005.

La combinaison des LDDMM et des "courants" nous permet alors de construire un modèle de la population. Généralement les formes sont analysées par leurs déformations depuis le modèle de la population. Pour l'analyse statistique de ces formes nous utilisons une ACP sur les vecteurs moments initiaux venant du modèle et allant vers les formes. Ces vecteurs moments initiaux ont l'avantage de déterminer entiè-

rement la déformation de la forme, tel un vecteur vitesse initial lors d'un lancer de projectile.

Pour ce qui est du calcul du modèle de la population (la partie la plus imposante du processus d'analyse de la forme basée sur un modèle en terme de temps de calcul), il y a plusieurs méthodes proposées dans la littérature qui sont toutes coûteuses en temps de calcul, ce qui est un frein à l'analyse de grandes bases de données. Nous allons nous intéresser à une méthode qui n'admet aucun a priori sur la forme du modèle. De cette méthode va découler la méthode que nous allons présenter au chapitre 5 puis utiliser dans les analyses de cette thèse.

Chapitre 4 : Étude des inversions incomplètes de l'hippocampe Dans ce chapitre nous présentons les critères utilisés pour l'évaluation des Inversions Hippocampique Incomplètes (IHI). La fréquence des IHI dans la population saine est mal connue. On sait seulement que ce variant anatomique de l'hippocampe semble plus présent chez les sujets épileptiques et qu'il est présent chez les sujets sains, mais cette fréquence varie beaucoup suivant les critères utilisés pour déterminer si l'hippocampe présente une IHI et suivant la population utilisée. Nous allons donc étudier les IHI sur une grande base de données (pour une bonne puissance statistique) composée de 2008 sujets, et nous allons faire en sorte d'avoir des critères simples et reproductibles. Dans la littérature beaucoup de critères ont été utilisés, souvent de manière très subjective, pour décrire les IHI. Nous avons choisis d'utiliser les critères les plus récurrents qui semblent aussi les plus faciles à caractériser afin d'en faire des critères reproductibles pour l'évaluation d'une grande base de données. Les critères retenus sont : le critère C1, qui porte sur la rondeur et la ver-

ticalisation de l'hippocampe dans les coupes coronales du corps, le critère C2 qui porte sur la profondeur du sillon collatéral et son orientation, le critère C3 qui porte sur la position plus ou moins médiale de l'hippocampe, le critère C4 qui porte sur un potentiel épaissement anormal du subiculum, et finalement le critère C5 qui porte sur les deux sillons du gyrus fusiforme et qui indique si l'un de ces sillons dépassent latéralement l'hippocampe au niveau du subiculum. Un critère global C0 a aussi été utilisé ; il note l'aspect général de l'hippocampe et indique si il présente une IHI ou non. Ces critères ont été notés sur 2008 sujets de la base européenne IMAGEN composée de jeunes (entre 13 et 15 ans) sujets sains. Les notes ont été données par 2 observateurs CC et FC, ainsi que la qualité des segmentations des hippocampes faites par le logiciel de segmentation automatique SACHA. 42 sujets ont été utilisés pour tester la reproductibilité inter et intra observateurs des critères de IHI. Un kappa test nous permet de dire que ces critères, comme détaillé dans ce chapitre, sont reproductibles ($\text{kappa} > 0.64$ pour tous les critères). Dans ce chapitre on remarque aussi que les segmentations sont corrélées aux IHI : plus l'hippocampe présente une IHI, moins sa segmentation est fiable. Cependant certains hippocampes présentant des IHI ont tout de même eu une segmentation correcte. Le critère global C0 donne une prévalence de 17% de IHI à gauche et de 6.5% à droite avec de chaque côté des intervalles de confiance assez petits. On a aussi observé qu'il n'y avait pas de différences entre hommes et femmes, ni entre droitiers et gauchers. L'analyse des critères individuels nous indique que les répartitions des notes de chacun de ces critères sont différentes entre le côté droit et le côté gauche ; les notes sont généralement plus élevées à gauche qu'à droite. La somme des 5 critères individuels (IHI score),

montre qu'il y a une sorte de continuum entre les notes ; il n'y a pas de coupure évidente. Cette somme de critères peut être utilisée comme un indicateur du degré de l'IHI. Cependant en catégorisant par le critère global, on a remarqué que les hippocampes sans IHI se séparent plutôt correctement bien des hippocampes avec IHI. Un seuil a donc été calculé pour déterminer à partir de quel score l'hippocampe semble avoir probablement une IHI, afin de pouvoir faire des études de groupes en utilisant uniquement les critères individuels présentés ici.

Chapitre 5 : Barycentre difféomorphique itéré Dans ce chapitre nous présentons la méthode des barycentres itérés basée sur la théorie des déformations difféomorphiques. Comme énoncé dans le chapitre 3, le modèle de forme utilise une représentation en tant que courants mathématiques. L'idée de la méthode est d'améliorer l'initialisation de la méthode présentée par Glaunès et al. (2006) en fournissant à la méthode une meilleure initialisation, plus proche du résultat final. L'idée de cette méthode est de calculer un barycentre itératif dans l'espace des déformations. Le barycentre est initialement choisi comme l'un des sujets de la population, puis on effectue un recalage de ce sujet vers un autre sujet et on stoppe la déformation au milieu de la trajectoire pour ainsi obtenir le barycentre de 2 sujets. On ajoute d'autres sujets au barycentre en itérant le processus : on recalcule le barycentre actuel vers un troisième sujet et on stoppe la déformation à $1/3$ de la trajectoire de déformation pour obtenir le barycentre de 3 sujets. Le barycentre ainsi calculé dans un espace euclidien, est le centre exact de la population, et son calcul ne dépend pas de l'ordre des sujets. Mais ici nous utilisons des recalages inexacts (du fait des maillages différents, et de la différence trop importante entre certaines formes)

dans des espaces courbes, ce qui ne permet pas d'atteindre le centre exact et rend le calcul du barycentre dépendant de l'ordre des sujets. Nous proposons 3 algorithmes différents pour la mise à jour du barycentre. Pour connaître l'impact de l'ordre des sujets sur le centrage du barycentre nous avons fait des expériences sur trois bases de données. Data1 est composé de 500 maillages simples (135 sommets) d'hippocampes formés à partir d'un maillage d'hippocampe et de déformations principalement diffeomorphiques, Data2 est composé de 95 hippocampes avec les mêmes maillages (1001 sommets), et RealData est composé des mêmes 95 hippocampes que Data2, avec des maillages différents pour chaque hippocampe. 10 ordres différents ont été utilisés pour générer 10 barycentres différents pour chaque dataset. Les distances entre les différents barycentres sont petites comparées aux distances de la population. Visuellement ces différences sont à peine visibles. On a évalué le centrage des barycentres en utilisant le ratio entre la norme des vecteurs moments initiaux et la moyenne des normes des vecteurs moments initiaux. Le centrage est meilleur pour le dataset Data1 que pour les deux autres datasets car il comporte des maillages plus simples. Le centrage pour Data2 est similaire au centrage pour RealData, ce qui nous permet de dire que la différence de maillages utilisés a très peu d'influence sur le résultat final. On a aussi observé que ces barycentres utilisés comme initialisation d'une méthode variationnelle d'estimation de template permettent un meilleur résultat final. Cependant le temps de calcul de la méthode du barycentre itéré est beaucoup plus petit que celui de la méthode variationnelle d'estimation de template ; de plus la méthode des barycentres fournit déjà un assez bon résultat de centrage, ce qui permet d'envisager d'utiliser un barycentre directement comme un template de

la population, pour par la suite analyser cette population par rapport à ce template.

Chapitre 6 : analyse de formes statistique basée sur le barycentre itéré

Dans ce chapitre nous utilisons le barycentre itéré d'une population comme template pour l'analyse de la variabilité anatomique par analyse en composantes principales (ACP) sur les vecteurs moments initiaux ou les matrice de distances approximées. On utilise ici 3 datasets, le premier est un dataset synthétique (SD50) calculé à partir d'un maillage d'hippocampe. Les 50 formes de ce dataset sont construites en utilisant des déformations difféomorphiques, de sorte que le maillage d'hippocampe initial se trouve exactement au centre de la population, et que le centre de cette population est connu. Le dataset RD50 est un sous ensemble de 50 maillages d'hippocampes de la base IMAGEN, et le dataset RD1000 est un sous ensemble de 1000 maillages d'hippocampes de la base IMAGEN. Des expériences ont été faites sur les datasets SD50 et RD50. Nous avons testé le centrage des barycentres de ces populations à l'aide du ratio décrit dans le paragraphe précédent. Pour SD les barycentres, ainsi que les templates variationnels calculés à partir de la méthode de Glaunès et al. sont très proches du vrai centre de cette population, mais aucun n'est à sa position exacte. Pour RD50, les ratios de centrage des templates (barycentre et template variationnels) sont évidemment moins bons, mais sont tous du même ordre et semblent proche les uns des autres par rapport au reste de la population. Ils sont tous plus proches du centre que n'importe quel sujet du dataset. Pour le dataset SD50, les résultats de l'ACP sur les vecteurs moments initiaux depuis les barycentres sont très similaires au résultat de l'ACP obtenu à partir du vrai centre du dataset. Pour RD50, les courbes de variance expliquée cumulative sont très si-

milaires entre celles calculées à partir des barycentres et celles calculées à partir des templates variationnels. De même pour les matrices de distances approximées, elle sont également différentes de la matrice de distances directes (calculée en déformant les sujets 2 à 2). l'analyse de formes en utilisant les barycentres donne des résultats similaires, de plus le calcul du barycentre est beaucoup plus rapide que le template variationnel. Pour appliquer ce pipeline, on applique ce calcul de barycentre sur le dataset RD1000 issu de IMAGEN, dont les sujets ont tous reçu un IHI score (voir chapitre 4). On a pu remarquer que le barycentre était plutôt bien centré dans la population, et que l'ACP pouvait expliquer plus de 97% de la variabilité anatomique de cette population à l'aide de 50 dimensions. Il est intéressant de noter que ce nombre de dimensions est stable quand on inclut un nombre de sujets suffisamment élevé. Nous avons par la suite utilisé quarante dimensions de l'ACP pour essayer de prédire les scores IHI à l'aide d'une régression linéaire multiple. On a réussi en utilisant entre 20 et 40 dimensions à prédire les score IHI avec une corrélation de 69%. Les modales de régression linéaire ont été validées par une méthode de validation croisée k-fold avec $k=100$.

Chapitre 7 : analyse de formes appliquée à des patients Alzheimer Dans ce chapitre nous appliquons la méthode rapide d'analyse de forme utilisant un barycentre à des hippocampes de la base ADNI composée de sujets âgés sains (groupe CN) et de sujet atteints de la maladie d'Alzheimer (groupe AD). La population est composée de 160 CN et de 134 AD. Tous ces sujets ont un score MMSE (Mini Mental State Examination) indicateur global de démence et un score ADNI-MEM qui est un score composite reflétant les performances des sujets à des tests de mé-

moire. Dans un premier temps nous comparons le barycentre du groupe CN à celui du groupe AD, et nous constatons que le premier axe de variation est très différent entre ces deux groupes. De plus le groupe AD a besoin de moins de dimensions pour expliquer sa variance anatomique (environ 60 contre 80 pour le groupe CN). A l'aide du barycentre de la population totale, nous projetons ensuite le premier axe de chaque groupe sur les 2 premiers axes des groupes, ce qui nous permet de voir que ces 2 groupes se différencient déjà sur les 2 premières dimensions de l'espace ACP de la population totale. Nous nous sommes ensuite intéressés à la prédiction des notes MMSE et ADNI-MEM dans la sous population des sujets âges sains en utilisant les 50 premières dimensions de l'espace ACP. Nous observons alors que comme prévu la prédiction du résultat du test MMSE est mauvaise et la prédiction de ADNI-MEM score est assez bonne ; une trentaine de dimensions suffisent à prédire le score ADNI-MEM. Le résultat est logique, car le ADNI-MEM score reflète les performances de mémoire pour lesquelles l'hippocampe joue un rôle central, alors que le score MMSE est un indicateur global de la démence. Il serait donc bien étonnant que l'hippocampe seul arrive à prédire un tel indicateur. On en conclut donc que notre méthode d'analyse de forme produit des résultats cohérents.

conclusion Pour ce travail de thèse qui consistait à analyser la variabilité anatomique de l'hippocampe sur de grandes bases de données, nous avons d'une part mis au point une méthode d'analyse de forme de l'hippocampe applicable à de grandes populations. D'autre part, nous avons étudié une forme anatomique particulière de l'hippocampe, l'IHI qui pourrait être d'origine développementale et qui a été surtout étudiée dans des populations épileptiques. Nous avons mis au point des critères

robustes d'évaluation des IHI, qui permettront par la suite de comparer les études. On a pu remarquer dans ce travail que les IHI ne sont pas rare puisque présentent dans environ 20% de la population. L'analyse de forme utilisant un template de la population que nous avons mise au point est capable de capturer la variabilité anatomique des hippocampes avec peu de variables et est capable de prédire certains paramètres biologiques comme la présence ou non d'IHI ou certain paramètres cliniques comme le score ADNI-MEM chez les sujets âgés sains. Il reste des questions auxquelles il serait intéressant de trouver une réponse. Premièrement, est ce que les IHI sont des variants anatomique qui affectent uniquement l'hippocampe ou non. Il serait intéressant de s'intéresser aux relations entre IHI et les sillons adjacents. D'autres parts, les facteurs génétiques et/ou environnementaux du développement de ces IHI sont encore inconnus. D'un point de vue méthodologique, il y a aussi plusieurs perspectives. Il serait intéressant de comparer la méthode des barycentres à d'autres méthodes de création de template. Il serait aussi intéressant de regarder l'impact du calcul de barycentre sur une population constituée de structures plus complexes comme les sillons par exemples.

CHAPTER 1

INTRODUCTION

The hippocampus is a brain structure involved in important cognitive functions as memory processes, long term memorisation and in spatial navigation. Another fascinating feature of the hippocampus is that it preserves its ability to generate neurons throughout life ([Eriksson et al., 1998](#)) by dividing progenitor cells in the dentatus gyrus, one of the two cortical lamina composing the hippocampus. Studies found that hippocampi are involved in many pathologies and psychiatric disorders such as Alzheimer's disease, epilepsy, depression and schizophrenia.

The anatomy of the human brain is highly variable. The genetic and environmental bases of this variability remain largely unclear. So does the influence of anatomical variability on the development of pathologies or cognitive functions. The anatomy of the hippocampus is also variable. A particularly remarkable anatomical variant of the hippocampus is the Incomplete Hippocampal Inversion (IHI). Indeed an inversion of the hippocampus occurs around the 25 gestational week. When the inversion is not completed, this results in the anatomical variant named IHI. This Incomplete Hippocampal Inversion is characterized by shape changes visible on Magnetic Resonance Images. IHI have been mostly described in patients with epilepsy, in which they are highly frequent ([Baulac et al., 1998](#)). However, they are also present in healthy subjects although their prevalence and characteristics have not been rigorously studied.

Magnetic Resonance Images (MRI) allows exploring brain anatomy in vivo. The generalization of MRI has made it possible to study anatomical variability in large populations. This allows studying statistically normal and abnormal developmental patterns and their correlation with cognitive, behavioural, genetic or environmental variables.

The objective of Computational Anatomy (CA) is to mathematically model and analyse the anatomical variability of biological structures. The study of biological shape variability has been first introduced by the famous biologist but also mathematician D'Arcy Thompson ([D'Arcy Thompson, 1917](#)). Since that time significant efforts have been made to develop a theory for statistical shape analysis. In the past years, a large number of statistical shape analysis methods have been proposed to

quantitatively analyse the variability of biological shapes. Among these, an interesting framework for anatomical shape analysis is the Large Diffeomorphic Deformation Metric Mapping (LDDMM) framework that quantifies differences between shapes via smooth deformations which capture the global and local non-linear variations while preserving the anatomical structure organisation. Another attracting feature of the LDDMM framework is that deformations are entirely parametrised by vectors lying in vector space, providing a natural setting for statistical analysis. Moreover, the framework of currents can be used to represent the shapes without assuming point-to-point correspondence across subjects. A now classical method is to compare shapes to a template of the population, this is named template-based shape analysis. These last years we have seen the emergence in neuro-imaging of large databases. However, the application of LDDMM approaches to large datasets is difficult because of their high computational load. Faster approaches for LDDMM-based template estimation are then needed for the analysis of large databases.

* *

*

The goal of this thesis is to develop and evaluate methods to study the anatomical variability of the hippocampus using large databases. Our developments were made in the framework of LDDMM for modeling deformations, and of currents for modeling anatomical surfaces. Within these frameworks, we aimed to develop fast approaches for template-based shape analysis. Our goal was then to apply these approaches to predict the presence of specific anatomical variants as well as the variation of cognitive or clinical variables. In particular, we were interested in the

prediction of the presence of Incomplete Hippocampal Inversions (IHI). To that aim, we also needed to visually characterize the presence of this variant in a given population.

We first focused on the evaluation of the Incomplete Hippocampal Inversions (IHI). To this aim, we proposed a new set of criteria to evaluate IHI, by adapting criteria from the literature. This new set of criteria is adapted to the evaluation of large datasets. These criteria were applied to study the prevalence and characteristics of IHI in a database of over 2000 MRI of young healthy subjects from the multi-centric European database IMAGEN. We also explored the impact of IHI on automatic hippocampal segmentation, the differences between males and females, and between right and left sides. This is the first time that this anatomical variant has been studied on a large dataset of healthy subjects.

Then, we developed and evaluated a new statistical shape analysis method adapted to the study of large databases. Its principle is that of template-based shape analysis, in which every individual shape is characterized through its deformation from a template of the population. In particular, we proposed new approaches for fast estimation of population templates. They are based on the estimation of population centroid using iterative diffeomorphic matchings. The centroid can then be directly used as a template, or as an initialization for another template estimation method. We performed various experiments to evaluate the properties of the centroid, its robustness and its impact on statistical results. We then applied this method to a template-based statistical shape analysis on 1000 young healthy subjects of the IMAGEN database, in which we aimed to predict the IHI score pre-

viously evaluated. We also applied this method to a dataset composed of around 300 subjects of the Alzheimer’s Disease Neuroimaging Initiative (ADNI) database (Alzheimer’s disease patient and elderly controls), in which we aimed to predict the memory score in Alzheimer’s disease patients population.

* *
*

The rest of this manuscript contains the following chapters.

Chapter 2 In this chapter, we briefly review the anatomy, development and roles of the hippocampus. We also quickly present Incomplete Hippocampal Inversions.

Chapter 3 This chapter first presents different ways to describe a shape and different methods to analyse these shapes. We then present with more details the LDDMM framework and the use of currents for shape representation.

Chapter 4 This chapter presents a study of Incomplete Hippocampal Inversion on a large dataset of healthy subjects using visual criteria. We first present the criteria used in the literature to describe Incomplete Hippocampal Inversions, before introducing a new set of criteria. These are used for the evaluation of more than 2000 subjects of the database IMAGEN. We finally present results on the prevalence of IHI in the healthy population, the influence of the IHI on the quality control of segmentations, and results on the IHI score.

Chapter 5 In this chapter, we present the diffeomorphic iterative centroid method used to compute a centroid of the population. In this chapter the centroid is used to improve the initialization of a variational template estimation method.

Chapter 6 In this chapter, we use the diffeomorphic iterative centroid method directly as a template of the population. We show that using the centroid as a template is sufficient for a template-based shape analysis of the hippocampus. We then use the result of the analysis to predict the IHI score.

Chapitre 7 In this chapter, we apply the pipeline described in the previous chapter to 298 subjects of the ADNI database (Alzheimer’s disease(AD) patients and elderly controls). We study anatomical differences between the two groups, and predict clinical parameters in the AD population.

Publications related to this thesis

Journal paper

Cury C., Glaunès J. A., Chupin M., Colliot O., and ADNI. (2015). Analysis of anatomical variability using diffeomorphic iterative centroid in patients with Alzheimer’s disease. Accepted for publication in *Computer Methods in Biomechanics and Biomedical Engineering: Imaging and Visualisation*.

Book chapter (peer-reviewed)

Cury, C., Glaunès, J. A., and Colliot, O. (2014). Diffeomorphic Iterative Centroid Methods for Template Estimation on Large Datasets. In F. Nielsen (Ed.), *Geometric Theory of Information, Signals and Communication Technology* (pp. 273–299). Springer International Publishing.

Conference papers (peer-reviewed)

Cury, C., Glaunès, J. A., Chupin, M. and Colliot, O., and ADNI. (2014). Fast Template-based Shape Analysis using Diffeomorphic Iterative Centroid. In C. C. Reyes-Aldasoro & G. Slabaugh (Eds.), *MIUA 2014-Medical Image Understanding and Analysis 2014*, (pp. 39-44), Egham, UK. (Best oral presentation award)

Cury, C., Glaunès, J. A., and Colliot, O. (2013). Template Estimation for Large Database: A Diffeomorphic Iterative Centroid method using Currents. In F. Nielsen & F. Barbaresco (Eds.), *GSI2013 - Geometric Science of Information*, volume 8085 of *Lecture Notes in Computer Science* (pp. 103-111).: Springer. Paris, France. (Oral presentation)

Conference abstract

Cury C., Glaunès J., Gerardin E., Chupin M. and Colliot O. (2012). Modelling morphological variability of the hippocampus using manifold learning and large deformations. *OHBM 2012 - 18th Annual Meeting of the Organization for Human Brain Mapping*, Beijing, China. (Poster presentation)

Submitted journal paper

Cury C., Glaunès J. A., Toro R., Chupin M., Schumann G., Frouin V., Poline J.-B., and Colliot O. (2015). Statistical shape analysis of large datasets using Diffeomorphic iterative centroids. Submitted to *IEEE Journal of biomedical and health Informatics*.

FIRST PART



BACKGROUND

CHAPTER 2



THE HUMAN HIPPOCAMPUS

The hippocampus is a bilateral brain structure of the temporal lobe which is implicated in memory processes, spatial navigation and in some pathologies as Alzheimer's disease, epilepsy depression or schizophrenia.

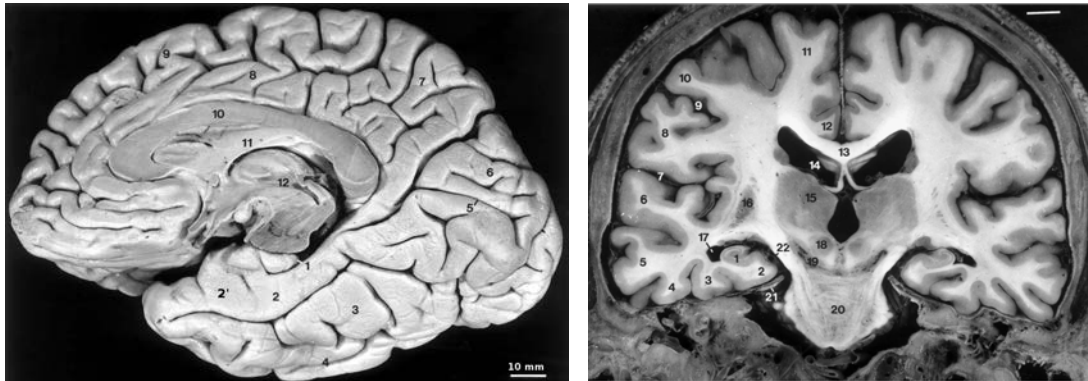
This chapter is organized as follows. In section 2.1 the description of the anatomical structure of the hippocampal formation, his development, and a certain anatomical variation of the hippocampus are presented. In section 2.2 we describe how hippocampal anatomy can be studied in vivo using Magnetic Resonance Images.

We finally present the roles played by the hippocampus in memory processes, spatial navigation, and its implication in different neurological and psychiatric diseases in section 2.3.

2.1 Anatomy, development and variability

2.1.1 Terminology

Let's start with a brief history of the origins of the term "hippocampus": this anatomical structure forms an arc with the anterior part larger than the posterior part, as a "comma". This identification as a comma did not become the reference, since in 1587 the anatomist Guilio Cesare Aranzio compared this structure to a "sea horse" (hippocampus in latin) or a "silkworm": the larger part corresponding to the head of the hippocampus and the narrower to the tail. Georges Duvernoy, in 1729, also compared this structure to a hippocampus or a silkworm. The physician J.B. Winslow in 1732 suggested the term "ram's horn". Then the surgeon R-J C de Garengot used the term cornu Ammonis in reference to the egyptian god Ammon Kneph represented with ram's horn and lion's tail. Today it is the term "hippocampus" which refers to this cerebral structure located on the temporal lobe protruding in the lateral ventricles. The term cornu Ammonis is still used to describe one of the two cortical U-shaped lamina rolled up one inside the other which compose the hippocampus with the gyrus dentatus. In general the term "hippocampus proper" refers to the cornu Ammonis, the term "hippocampus" refers to the hippocampus proper plus the gyrus dentatus and the alveus (see section 2.1), and the term "hip-



(a) 1 - hippocampus, 2 - parahippocampal gyrus (T5), 2' - entorhinal cortex, 3 - fusiform gyrus (T4), 4 - infero temporal gyrus (T3), 5 - calcarine sulcus, 6 - occipital lobe, 7 - medial part of the parietal lobe, 8 - cingulate gyrus, 9 - medial part of the frontal lobe, 10 - corpus callosum, 11 - fornix, 12 - third ventricle

(b) 1 - hippocampus, 2 - parahippocampal gyrus (T5), 3 - fusiform gyrus (T4), 4 - infero temporal gyrus (T3), 5 - middle temporal gyrus (T2), 6 - superior temporal gyrus, 7 - lateral fissure, 12 - cingulate gyrus, 13 - corpus callosum, 14 - lateral ventricle, 15 - thalamus, 18 - red nucleus, 20 - pons, 22 - ambient cistern

Figure 2.1: Dissection of the inferomedial part of the right hemisphere (a), and coronal section of a brain (b). From [Duvernoy \(2005\)](#).

"pocampal formation" includes the hippocampus and the subiculum.

2.1.2 Spatial localisation

The brain is composed of two hemispheres and each hemisphere is composed by different lobes:

- the frontal lobe located just behind the forehead is implicated in planning, voluntary movements and language
- the parietal lobe located to the rear is a sort of associative cortex of the sensory system and integrates information coming from vision, touch or hearing.

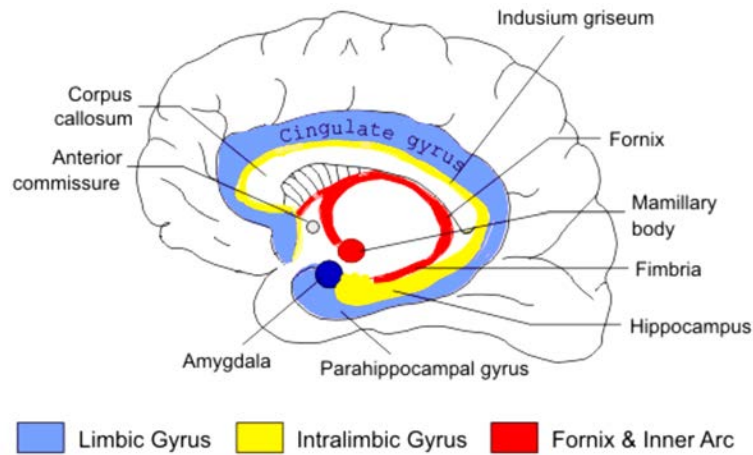


Figure 2.2: The limbic system

- the occipital lobe situated at the occipital bone is the center of the vision.
- the temporal lobe situated behind each ear is related to multiple cognitive processes such as language recognition and visual memory. It is divided in five convolutions.

The human hippocampus is a bilateral cerebral structure located in these temporal lobes, in the fifth convolution (T5) which has an internal positioning. Figure 2.1(b) shows the medial positioning of the hippocampus. The hippocampi form the medial and the bottom borders of the lateral ventricles. Figure 2.1(a) shows that they have a longitudinal shape in a sagittal view. The anterior part of T5 is composed of the entorhinal cortex, directly connected to the anterior part of the hippocampus.

The hippocampus is also part of the limbic system, a "brain into the brain" (see Figure 2.2) described and discussed by Broca in 1877, Papez in 1937, Mac Lean in 1952 and Nauta in 1972. The limbic system corresponds to the deep and internal

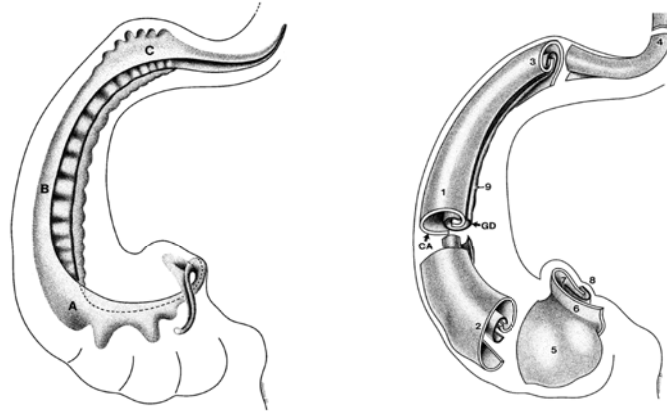


Figure 2.3: Anatomy of the hippocampus. Left: general shape of the gyrus dentatus in an axial point of view. Right: the two cortical U-shaped lamina of the gyrus dentatus (GD on the figure) and the cornu Ammonis (CA). A: head, B: body, C: tail, and right: the general shape of the hippocampus. Drawings are from [Duvvernoy \(2005\)](#)

regions of each hemisphere, such as T5 and the cingulate gyrus. It is composed of many structures (nuclei and primitive cortical areas) implicated in the memorisation process and emotions. The limbic system is the interface between the very "old" (from an evolutionary point of view) brain, the brainstem, and the very recent brain, the neocortex.

2.1.3 Anatomy

The hippocampus has an elongated shape in the rostro-caudal direction as shown in [Figure 2.3](#) with a length of 4 to 4.5 cm and a width of 1 to 2 cm. The hippocampus can be divided in three parts: the head, which is the anterior and largest part of the structure, presenting digitations, the body which is the middle part with a sagittal orientation, and the tail which is the posterior and narrowest part of the structure

and differs from the body with its transversal orientation.

The hippocampus is composed of two cortical lamina rolled up one inside the other the cornu Ammonis (CA) and the Gyrus Dentatus (GD) as shown in Figure 2.3.

The Cornu Ammonis is composed of three layers of grey matter (stratum oriens, stratum pyramidal and the stratum moleculare) of pyramidal cells which can be divided into four Ammonian fields, as introduced by Lorente de Nó (1934), which are: CA1, the largest one, is composed of pyramidal cells and triangular soma, CA2, very dense, is composed by large and ovoid soma, CA3, is less dense and is composed of mossy fibres which connect the gyrus dentatus to the cornu Ammonis, and CA4, even less dense in soma cells because of large number by mossy fibres, is directly in contact with the gyrus dentatus from which mossy fibres receive inputs. All these areas are recovered by a structure named alveus containing the output channels of the hippocampus, that is the axons of the pyramidal cells. The pyramidal cells are effectors and their axons in the alveus are perpendicular to the long axis of the hippocampus, and then are changing of direction and going parallel to the long axis of the hippocampus, to the fimbria. They send informations from CA1 and CA3 through the fimbria or from CA3 through the subiculum. The subiculum is the transitory region between the archicortex and the neocortex as shown in Figure 2.4. It is also an output channel of the hippocampus.

The gyrus dentatus is separated from the CA by the vestigial hippocampal sulcus, and is a prolongation of the induseum griseum (yellow area in Figure 2.2).

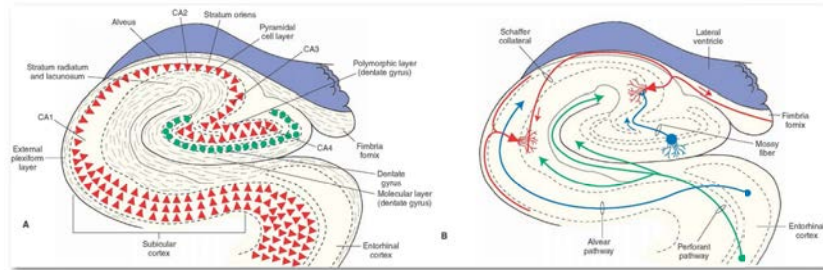


Figure 2.4: Anatomy of the hippocampus. Schema of the internal organisation of the hippocampus

The DG owes its name to its toothed aspect in its external part, as we can see in Figure 2.3(a). It is composed by a stratum of granular cells and a stratum of granular neurons, small and round. Contrarily to the pyramidal neurons of the cornu Ammonis, the granular neurons are afferent and receive the information directly from the entorhinal cortex (Figure 2.1 and Figure 2.4) via the perforant path which perforates the subiculum to reach the granular cells of the gyrus dentatus. The DG then sends the information to cornu Ammonis via the mossy fibres before leaving the hippocampus through the subiculum and through the alveus and fimbria. The gyrus dentatus is also responsible of neurogenesis in adulthood. For a long time, we believed that the neurogenesis was occurring only during the embryological state and the childhood. Eriksson et al. (1998) demonstrated that new neurons, are generated in the dentate gyrus of adult humans and that the human hippocampus retains its ability to generate neurons throughout life. An other study Parent et al. (1997) suggests that in case of epilepsy, prolonged seizure discharges stimulate dentate granule cell neurogenesis.

This polysynaptic intrahippocampal pathway is part of a more global system of

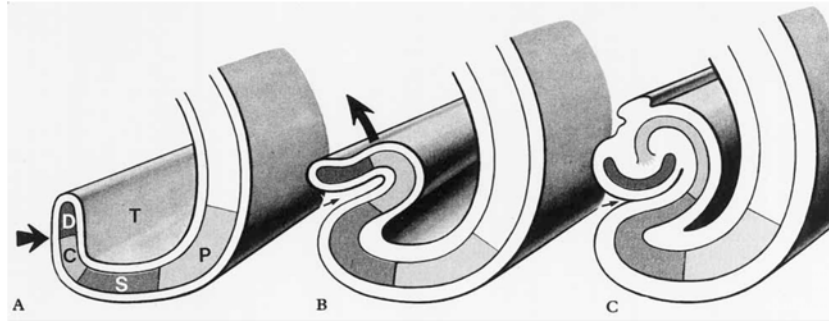


Figure 2.5: Schematic diagram of the temporal lobe in the coronal plane during the development of the hippocampus. D: gyrus dentatus, C: cornu Ammonis, S: subiculum, P: parahippocampal gyrus. Drawing from [Baker & Barkovich \(1992\)](#).

information processing named the Papez circuit, in the limbic system. The Papez circuit is composed of the entorhinal cortex, the gyrus dentatus, the cornu Ammonis, then the mammillary body is reached via the fimbria, and next the information goes to the thalamus which communicates with the neocortex, before going back to the enthorinal cortex.

2.1.4 Development

Various studies have described the development of the hippocampus, among others we can note [Humphrey \(1967\)](#) [Kier et al. \(1995\)](#) [Righini et al. \(2006\)](#) [Radoš et al. \(2006\)](#) [Baker & Barkovich \(1992\)](#). The hippocampal formation is the first cortical area to differentiate ([Humphrey, 1967](#)), and at 30 gestational weeks (GW), the hippocampus formation has acquired most of the features observed in the adult population. Figure 2.5 gives a schematic overview of the development of the hippocampus.

The beginning of hippocampal development is not very well known for now, but

seems to start before 10 gestational weeks. Baker & Barkovich (1992) observed primordial hippocampi on 7 GW fetuses. At 10 GW the gyrus dentatus and the cornu Ammonis are rudimentary structures situated in the postero-medial wall of the lateral ventricles as shown in Humphrey (1967).

At 13 GW, the hippocampus goes from the frontal lobe to the temporal lobe on the postero-medial wall of the lateral ventricles, and surrounds a widely open hippocampal sulcus as observed in the studies of Humphrey (1967) and Kier et al. (1997). At this stage of brain development, the corpus callosum is not yet formed. Figure 2.6 shows a sagittal photography of a brain from a 13 GW foetus where the hippocampus is clearly visible. In a coronal view, as seen on the MRI on Figure 2.6(b), we can see that the hippocampus, indicated by the white arrows, is still unfolded. Although, it is between 12 to 14 GW that the gyrus dentatus is starting to fold toward the cornu Ammonis.

The studies of Kier et al. (1997) and Humphrey (1967) show that, three weeks later so at 16 GW, the hippocampus reduces in size (relatively to the size of the brain which increases), pushed by the growth of the corpus callosum and therefore has to leave the frontal lobe to only occupy the temporal lobe. In Kier et al. (1997) they also showed that this is at this period that the gyrus dentatus and the cornu Ammonis start their in-folding, and the sub-fields, CA1 CA2 and CA3 are arranged linearly as shown on Figure 2.7(c), the alveus is also visible.

From 20 GW, the relationship between the hippocampus and the surrounding structures is becoming similar to the adult population. This is the time for the hippocampi to terminate their in-folding. Righini et al. (2006) study the in-folding

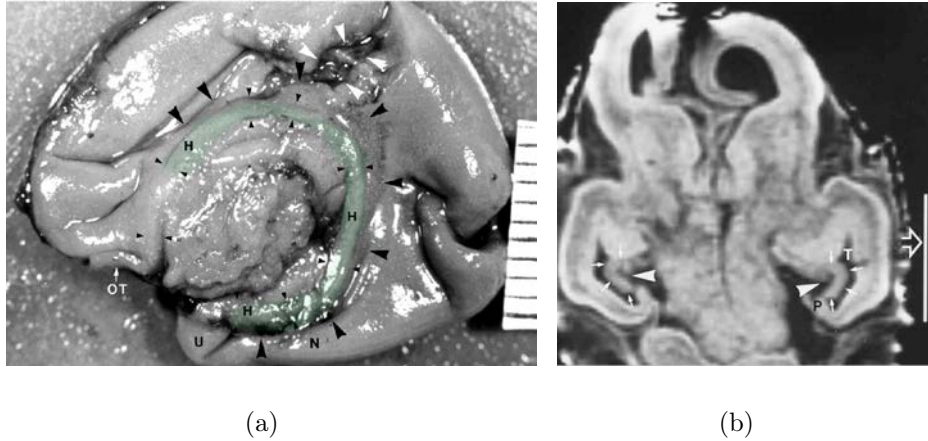


Figure 2.6: 13 GW. (a) Photography from [Kier et al. \(1995\)](#) in sagittal plane of the medial brain surface of a 13 GW foetus. The frontal lobe is on the left side of the photography and the temporal lobe on the bottom part and the hippocampus is highlighted in green. The corpus callosum is not yet formed. Large arrowheads, hippocampal sulcus; small arrowheads, the inner limbic arch of the hippocampal formation; OT, olfactory tract. The distance between two graduations is 1 mm. (b) Coronal T1-weighted spoiled gradient-echo MR image (45/8/2; 45° flip angle) of an intact 13 GW foetus from [Kier et al. \(1997\)](#). The neocortical parahippocampal gyrus region (P) is small, (T) is the temporal horn. The white vertical line measures 10 mm.

of the hippocampus on 62 foetal Magnetic Resonance Images from 20 to 37 GW with normal neuro-developmental examination at postnatal age. They found a correlation between the in-folding angle of the hippocampus and the gestational week. This angle is measured between the line connecting the lateral border of the cornu Ammonis with the medial superior border of the subiculum and the line passing through the midline structures. This angle takes values inferior to 70 degrees for foetuses of less than 25 GW, and superior to 70 degrees for foetuses of more that 30 GW. [Okada et al. \(2003\)](#) investigated the morphological development of the hippocampal formation in children. They showed that this angle increases by ap-

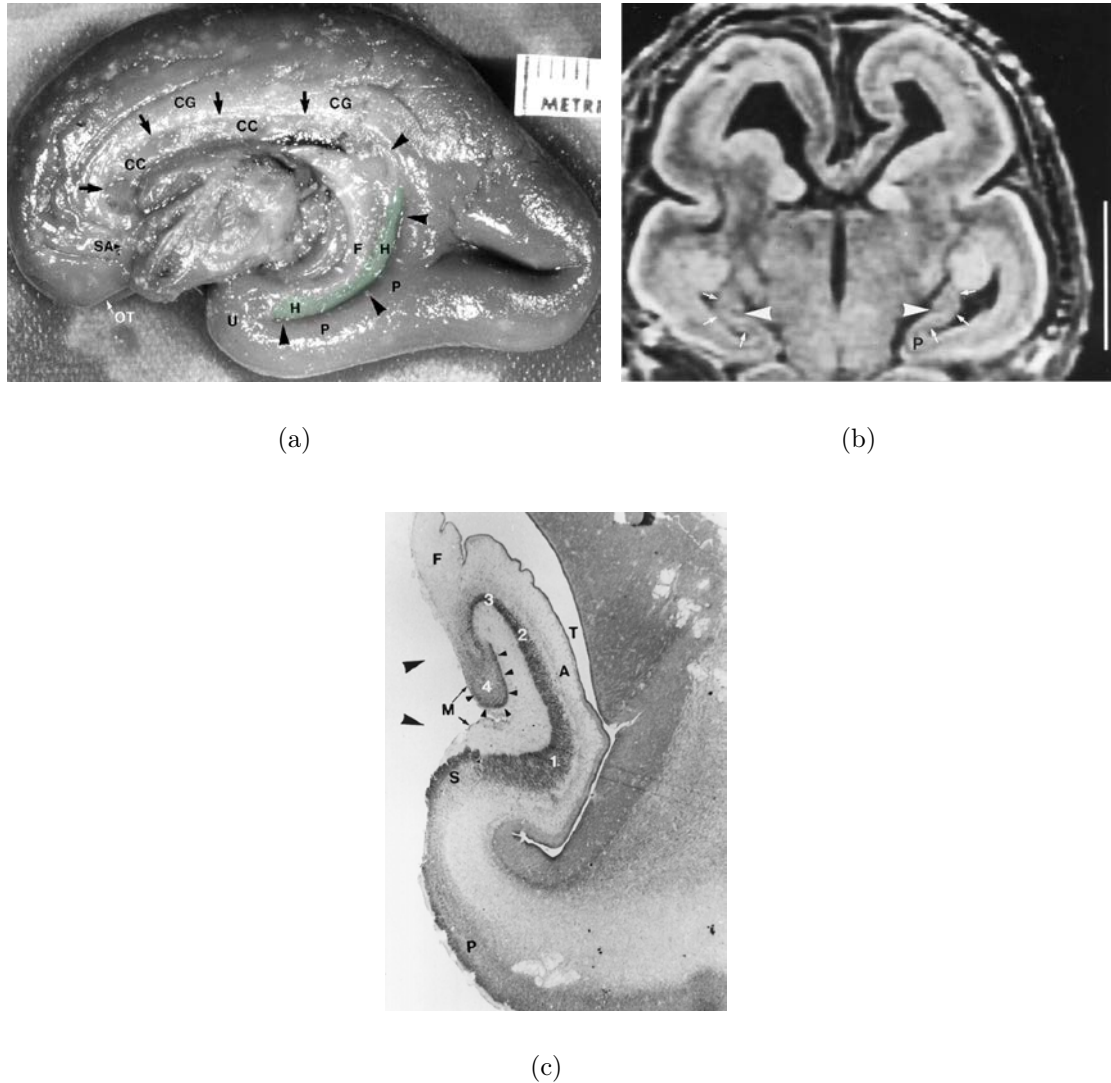


Figure 2.7: 16 GW. (a) Photography from [Kier et al. \(1995\)](#) in sagittal plane of the medial brain surface of a 16 GW foetus. Large arrowheads, hippocampal sulcus; small arrowheads, the inner limbic arch of the hippocampal formation; CC, corpus callosum; F, fornix; OT, olfactory tract. The distance between two graduations is 1 mm. (b) Coronal T1-weighted spoiled gradient-echo MR image (45/8/2; 45° flip angle) of intact 13 GW old foetus from [Kier et al. \(1997\)](#). The neocortical parahippocampal gyrus region (P) is small. The white vertical line measures 10 mm. (c) coronal histological section (Nissl, original magnification $\times 24$ from [Kier et al. \(1997\)](#)), the CA1 (1), CA2 (2), and CA3 (3) fields of the cornu Ammonis are arranged linearly. The dentate gyrus (small arrowheads) has a tight U-shaped configuration around the CA4 (4) field of the cornu Ammonis. The very thin molecular stratum (M) of the dentate gyrus is separated from the larger molecular stratum of the cornu Ammonis by the very wide hippocampal sulcus (large arrowheads).

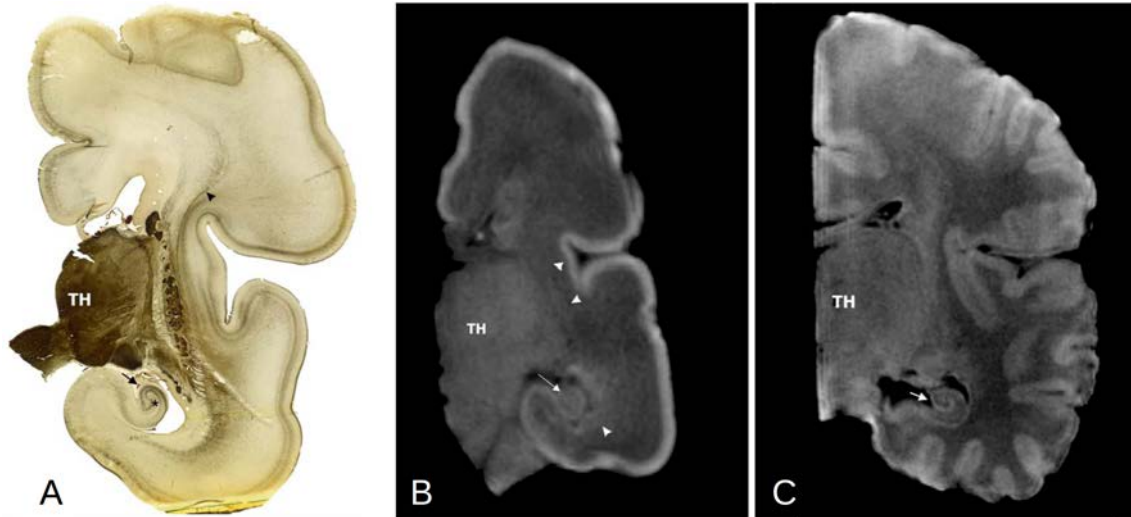


Figure 2.8: (A) acetylcholinesterase histochemistry of a 25 GW. (B) a T1-weighted MRI from a 25 GW, and (C), T1-weighted MRI from a full term new born. TH: Thalamus. Images are from [Radoš et al. \(2006\)](#).

proximately 5° during the 2 first decades after birth, against around 15° during the 17 weeks of gestation observed in [Righini et al. \(2006\)](#). In [Okada et al. \(2003\)](#) they also found that the mean angle was significantly larger for right hippocampus than for left hippocampus, but this result was not replicated in the study of [Righini et al. \(2006\)](#) on fetuses. Figure 2.8(A) and (B) shows a 25 GW, where we can see that the hippocampus has not achieved its inversion, and in (C) a full term new born in which we can see that the hippocampus has almost terminated its inversion.

[Bajic et al. \(2010\)](#) studied, using an ultra sound modality, the development of the hippocampus in pre-term neonates aged between 23 and 35 GW. They found, in a coronal view, a rounded shape of the hippocampus in 50% of the neonates aged between 23 to 24 GW, in 24% of the neonates aged between 25 to 28 GW and in 14% on the neonates aged between 29 and 36 GW. This rounded shape was mainly

left sided. Therefore, there are already developmental differences between the left hippocampus and the right hippocampus.

2.1.5 Incomplete hippocampal inversion

As we have seen, [Baker & Barkovich \(1992\)](#) observed that during the rotational growth of the telencephalic vesicle, the major portion of the hippocampus is carried dorso-laterally and then ventrally to lie in the medial aspect of the temporal lobe. As the neocortex expands and evolves, the allocortex is displaced inferiorly, medially and internally into the temporal horn. This is why we can observe an inversion of the hippocampus during the development.

There exists a remarkable anatomical variant of the hippocampus which has received various names including "malrotation" and "Incomplete Hippocampal Inversion". As proposed in [Raininko & Bajic \(2010\)](#), we use the term "Incomplete Hippocampal Inversion" (IHI) which better describes the incomplete inversion of the hippocampus than the term malrotation. These Incomplete Hippocampal Inversions have been initially observed in healthy subjects by [Bronen & Cheung \(1991\)](#), who showed that the anatomical variant of the hippocampus which presents a rounded shape in a coronal view on MRI (a criterion to describe these Incomplete Hippocampal Inversion) is a normal anatomical variation of the hippocampus. This particular anatomical variation has been mostly observed in patients with epilepsy (([Lehéricy et al., 1995](#); [Baulac et al., 1998](#))). In these studies they describe hippocampi with a rounded shape in a coronal view in MRI, a protruding collateral sulcus and a medial position of the hippocampus as shown in Figure 2.9. [Barsi et al. \(2000\)](#) wondered

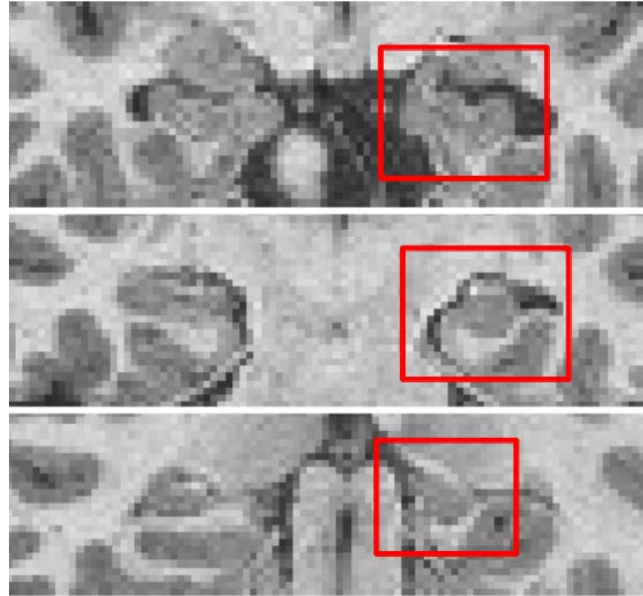


Figure 2.9: Coronal point of view of hippocampi, the 3 images are from the same subject, the top image shows the heads of the hippocampi, the middle image shows the bodies of hippocampi and the bottom one, the tails. The left hippocampus framed in red presents a rounded shape, a medial positioning and a deep collateral sulcus which are typical criteria for an IHI.

if this particular hippocampal shape has a developmental origin since they observe these IHI in subjects with corpus callosum agenesis. Finally, some studies demonstrate that this anatomical variant of the hippocampus, which mainly presents a rounded or vertical shape, a medial positioning and a deep collateral sulcus, has in fact a developmental origin (Righini et al., 2006; Bajic et al., 2010).

IHI have been mostly observed and studied in pathological cases such as epilepsy (Lehéricy et al. (1995), Barsi et al. (2000), Baulac et al. (1998), Bernasconi et al. (2005), Peltier et al. (2005), Stiers et al. (2010), Bajic et al. (2009), Friedman & Tandon (2013)) or congenital brain malformations (Donmez et al. (2009), Sato et al. (2001), Baker & Barkovich (1992)). These studies found very different frequencies

of IHI. In [Barsi et al. \(2000\)](#), they found 6% of IHI in a population composed of 597 patients with suspicion of epilepsy 69% of the IHI were left-sided, 19% right-sided and 12% bilateral. In [Peltier et al. \(2005\)](#), 14% of 97 epileptic patients had IHI. In [Bernasconi et al. \(2005\)](#), 43% of the 30 temporal lobe epileptic patients had IHI, and 49% of 76 patients with malformations of cortical development had IHI. In [Bajic et al. \(2009\)](#), 30% of the 201 patients with epilepsy had IHI, 67% of the IHI were left-sided, 7% right-sided and 27% bilateral. For the developmental brain malformations, [Baker & Barkovich \(1992\)](#) found IHI in 36% of 36 patients, [Sato et al. \(2001\)](#) found IHI in 64% of 44 patients and [Donmez et al. \(2009\)](#) 56% of IHI for 62 patients. These frequencies of IHI are different because of the chosen populations, but also because the criteria used to identify IHI are not identical, therefore do not allow reproducible or comparable results.

Some studies tried to determinate the frequency in the normal population. In [Bernasconi et al. \(2005\)](#) they found 10% of IHI in 50 healthy controls. In [Peltier et al. \(2005\)](#), IH were found in 6% of the control population composed of 50 subjects including 11 patients without epilepsy but including other pathologies. In [Bajic et al. \(2009\)](#) authors used 150 subjects including 116 patients, and found 18% of IHI, mostly left-sided. In one study ([Bronen & Cheung, 1991](#)) authors found that 21% of the 29 volunteers had a shape different than the usual flat appearance as the right hippocampus on Figure 2.9.

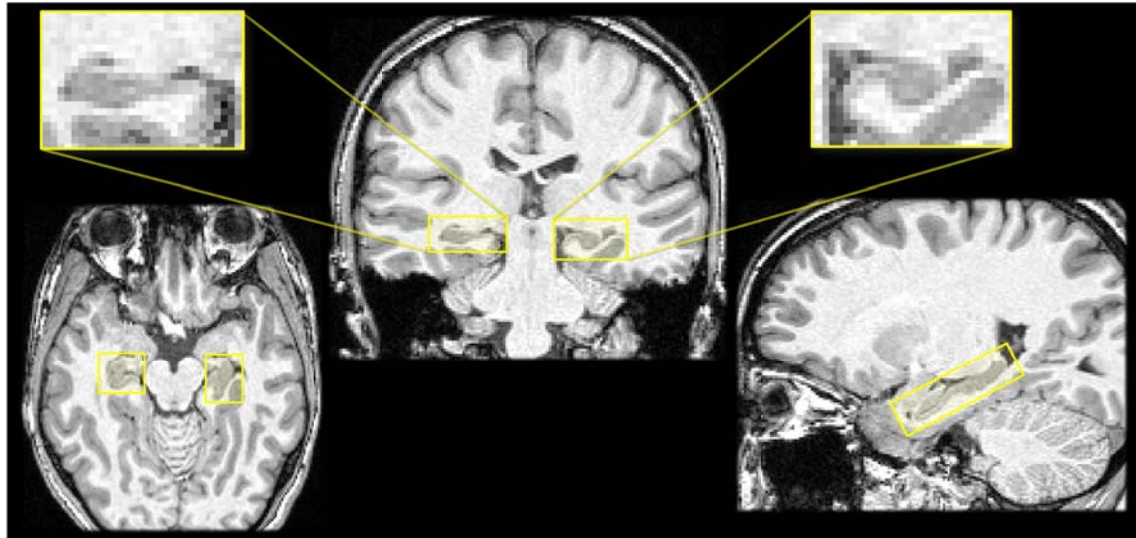
The limitations of these studies are that they not only include healthy controls but also patients without epilepsy nor developmental brain malformations but with various conditions; the size of the populations used which makes difficult a good

estimation of the frequency of IHI; the criteria used are not the same.

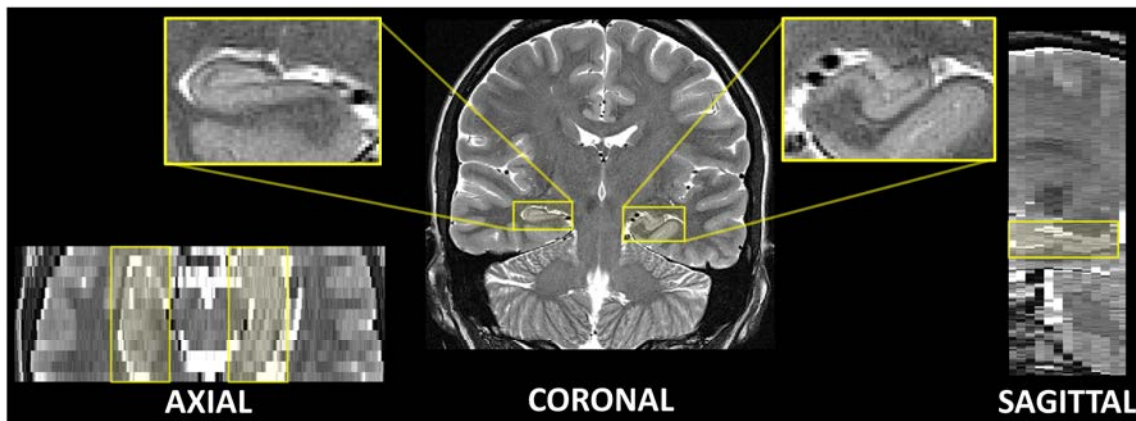
2.2 Visualisation in MRI

In vivo, the first choice of imaging techniques to observe brain structures as the hippocampus is Magnetic Resonance Images (MRI) with 3D T1-weighted sequences, with roughly $1mm$ isotropic resolution (Figure 2.10(a)). T1-weighted MRI measures the time of longitudinal relaxation (T1) i.e. the time needed by the hydrogen atoms (present in large quantities in molecules of biological tissues) to recover their initial balance after excitation by a magnetic field (1.5 or 3 Tesla in general), this time is different depending on the tissue property. Hypo-signal indicates liquids such as cerebro-spinal fluid and blood, the gray matter is in dark gray and the white matter in light gray. This sequence allows a good overview in 3 dimensions of the anatomical structures of the brain. Figure 2.10(a) shows three views (from left to right) axial, coronal and sagittal of the hippocampus on a 3D T1-weighted MRI. These three views allow to show the medial positioning of the hippocampus and its global elongated shape. They also allow a visualisation in 3 dimensions of the neighbouring structures, and a good overview of the whole brain. But this MRI sequence do not allow the identification of finer details of the hippocampus, as the cornu Ammonis or the gyrus dentatus; only the fimbria can be seen (in white in T1 MRI) but not clearly in every image.

It is also possible to use other MRI sequences such as the T2-weighted spin echo sequences to observe a particular structure or to detect variations of contrast in a tissue. This sequence measures the time of transversal relaxation (T2) which is



(a) T1-weighted with resolution $1mm \times 1mm \times 1mm$



(b) T2-weighted with resolution $0.3mm \times 0.3mm \times 4mm$

Figure 2.10: Two visualizations of hippocampus of a same subject from the IRMA7 database. (a) Magnetic Resonance Images with a T1-weighted acquisition and (b) T2-weighted acquisition. Views are (from left to right) axial, coronal and sagittal.

the time required for the spins (of the hydrogen atoms) to return to their phase coherence due to the spin-spin interactions. Hypo-signal indicates blood and air, the cerebro-spinal fluid is in hyper-signal, the white matter is in dark gray and the gray matter in light gray. This MRI sequence provides a better contrast of the inner structures of the hippocampus, but does not allow an isotropic resolution because of the acquisition time. In Figure 2.10(b), the sequence was acquired to have a good resolution in the coronal plane around the hippocampus. We can see a coronal view (in the middle) of the hippocampus: the cornu Ammonis, the gyrus dentatus, the hippocampus sulcus and even the alveus are clearly identifiable. Due to the anisotropic resolution, the axial and sagittal views are very difficult to interpret and do not permit a representation in three dimensions of any structure.

It is also possible to have an ultra-high resolution of the hippocampus in coronal view, with a good resolution in axial and sagittal, by using several T2-weighted sequences at 7 Tesla. Then a registration method is applied to these MRIs to co-register all sequences in order to obtain a good resolution in axial and sagittal. In Figure 2.11, we can observe the registration of different T2-weighted MR images at 7T (Marrakchi et al., submitted paper), on the same subject as in Figure 2.10. Figure 2.11 allows a good 3D visualization of the hippocampus subfields; the sagittal view shows the fimbria which is the dark line over the hippocampus, and as in the axial view one can observe the hippocampal sulcus which separates the cornu Ammonis from the gyrus dentatus. But the acquisition of such MRI is not always available since this is a reserche sequence and there is in France only two centre equipped by 7T systems adapted for humans.

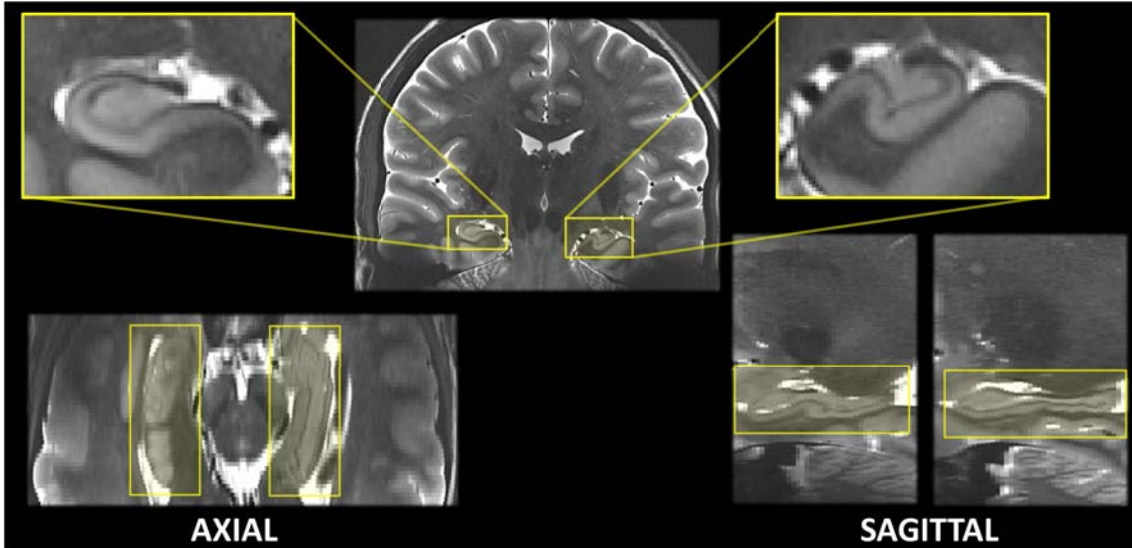


Figure 2.11: Visualization of the hippocampi of a same subject of the IRMA7 database in Figure 2.10. The volumetric image have been computed by Marrakchi et al. (submitted paper) from different T2-weighted sequence in 7T MRI, by registering the different acquisition using the 3T MRI.

We can see in all these images (figures 2.10 and 2.11) that the left hippocampus of the subject presents an incomplete hippocampal inversion.

The 3D T1 weighted MRI sequence allows a good visualization of the external boundaries of the hippocampus and to form large databases, which is exactly what we need to analysis the shape of the hippocampus.

2.3 Role

The medial part of the temporal lobe receives input from different regions. The perirhinal cortex and the parahippocampal cortex receive the information from the neocortical areas. These cortex are inter-connected and connected to the entorhi-

nal cortex which is itself the principal source of afferents of the hippocampus. The perirhinal and the parahippocampal cortex receive the efferents from the hippocampus and the entorhinal cortex and then project on the associative cortex. These structures are more than a simple interface for the communication between the hippocampal formation and the neocortical areas, these structures play a key role in the memorisation processes.

2.3.1 Memory

The term "memory" groups together different concepts and processes. The information processing is different according to the quantity of information to integrate and to the type of information. [Alvarez & Squire \(1994\)](#) developed a theory of the consolidation of the mnesic marks which supposes that the consolidation process starts when the informations coming from different sensory modalities are linked between each other under the form of a mnesic mark by the hippocampus and others structures of the temporal lobe. [Nadel & Moscovitch \(2001\)](#) and [Nadel et al. \(2000\)](#) proposed a different theory which is based on multiple mnesic marks. The hippocampus is a need for the recovery of episodic memories requiring a spatial context.

The different types of memories are listed below. A review of all memory types can be found in [Tulving \(1995\)](#).

Short term memory This mnesic system contains the working memory, and is a limited mnesic system in terms of capacity. This system keeps in memory

informations needed for a short term processing.

Long term memory This a mnesic system not limited in capacities, which allows the processing of informations from anterior learnings kept in memory. Long term memory can be divided in two types of memories: declarative (or explicit) memory and implicit memory.

Implicit memory This is a non-conscious process which permits the acquisition of motor abilities as riding a bike.

Declarative memory This memory requires the use of the temporal lobe, and is a conscious process. This mnesic system is based on informations that can be declared and are accessible to the conscience. Declarative memory can be divided into semantic memory and episodic memory.

Semantic memory This is the memory of general informations. This is the memory of the words, ideas and knowledge on the world regardless of the temporo-spatial information, without reference to the learning context.

Episodic memory According to [Wheeler et al. \(1997\)](#), episodic memory allows to mentally travel in time, and to consciously have a representation of past events to integrate them into a future project. This mnesic system allows the storage and the recovery of personal events situated in their temporal and spatial context.

The study of patients who have suffered brain lesions has made a significant contribution to the understanding of memory processes. First of all, this is the study of the famous amnesic patient known as H.M. which allowed a better understanding of the implication of temporal lobes in memories. H.M. was epileptic since childhood and to reduce its seizures, in adulthood he finally underwent a bilateral resection (in 1953) of its hippocampi, amygdala and a part of the neighbouring cortex (Scoville & Milner, 1957). After his surgery, H.M. lost his capability to form new long term memories. He was able to remind a sequence of words, but he forgot this sequence after stopping saying it. Furthermore, he lost the memory of events that happened during the three years before the resection. On the other hand, his procedural and implicit memories were intact. The many studies on this patient (Corkin, 2002; Squire, 2009) allow to conclude that short term memory, long term memory, procedural memory and declarative memory processes are different. These studies also showed the role of the temporal lobes in the consolidation of new informations in declarative memory, that is a long process since memory of years before the resection were lost. The declarative memory seems to be blocked by the absence of hippocampi. An other patient named K.C. and presented in the study of Tulving (2002), suffered a cranial trauma in 1981 at the age of 30. The MRI of his brain showed bilateral hippocampal lesions, but the sub-hippocampal structures were spared during the resection. K.C. cannot recollect any personal events whereas his semantic knowledge is intact: he knows many facts about himself and can learn new factual informations without any episodic memories. He can not imagine his future any more than he can remember the past. Unlike H.M., his semantic mem-

ory is preserved as his sub-hippocampal structures, and like H.M. he suffered very severe damage to his episodic memory. As suggested in [Rosenbaum et al. \(2005\)](#) and [Tulving \(2002\)](#), a distinction can be made between the hippocampi which play a critical role in episodic memory and the sub-hippocampal structures which appear to be more involved in semantic memory. This theory has been exposed in other works as in [Vargha-Khadem et al. \(1997\)](#) and [Warrington \(1975\)](#) with other patients with brain lesions.

2.3.2 Spatial navigation

Hippocampi also plays a role in spatial memory and navigation. In animal studies as in rats or mice ([O'Keefe & Dostrovsky, 1971](#)), they found that hippocampi present a type of neurons that becomes active when the rat enters in a particular place in the environment. These neurons are named place cells and have been identified in humans by [Ekstrom et al. \(2003\)](#). Furthermore the study of [Maguire et al. \(2000\)](#) on the taxi drivers of London, before the appearance of Global Positioning System (GPS), showed that the gray matter of the posterior part of the hippocampus was larger in taxi drivers than in control subjects, but in the anterior part of the hippocampus the gray matter was larger in control subjects than in taxi drivers. Authors also found a correlation between the amount of time an individual worked as a taxi driver and the volume of gray matter of the posterior and anterior part of the hippocampus. An other study on the role of hippocampi ([Burgess et al., 2002](#)), showed that the visualization of spatial scenes in virtual reality involves the parahippocampal gyrus. The right hippocampus seems to be involved in

memory for locations within an environment whereas the left hippocampus seems to be involved in context-dependant episodic memory or in autobiographical memory (Burgess et al., 2002; Maguire, 2001).

2.3.3 Pathologies

We will make a short description of the main pathologies in which the hippocampus is involved.

Temporal Lobe Epilepsy The first document about epilepsy dates from 2000 BC: epilepsy is described as a supernatural characteristic, since the sick persons were thought to be under the influence of a god. Even if Hippocrates suggests in a treatise, in 400 BC, that this sacred disease is not spiritual but a disease caused by a brain impairment (and named it the grand mal (great disease)), it is only from the 17-18th century that epilepsy was considered as a neurological disease.

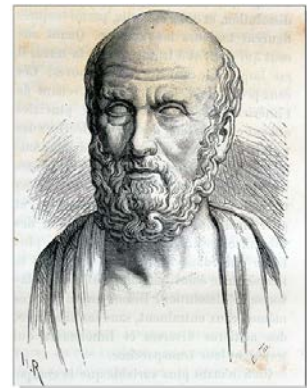


Figure 2.12: Hippocrates

Now epilepsy is considered as a brain disorder characterized by generalized or focal epileptic seizures. Among the different forms of focal epilepsies, the most frequent is temporal lobe epilepsy (TLE), which is present in around 40% of cases (Engel Jr, 1996). Seizures generally start in the hippocampus (Spencer et al., 1990) and continue during one or two minutes with or without alteration of conscious-

ness. The association between hippocampal abnormalities and TLE is well-known, hippocampal sclerosis (atrophy of the hippocampus with altered signal intensity in MRI) is a frequent finding in patients with TLE (Eriksson et al., 2008). Even if it is not yet clear whether epilepsy is caused by hippocampal abnormalities, or whether the hippocampus is damaged by cumulative effects of seizures, TLE is resistant to medications in 89% of cases when patients present hippocampal sclerosis, in 75% of cases when patients present a malformation of cortical development and in 97% of cases of malformation of cortical development and hippocampal sclerosis (Semah et al., 1998). In carefully selected patients, epilepsy surgery can effectively control seizures as shown in Wiebe et al. (2001). MRI plays an important role in the pre-surgical evaluation to determine the presence or not of atrophy, since in case of atrophy, more than 70% of surgically treated TLE patients achieve to be seizures free after surgery (Wiebe et al., 2001; Wiebe, 2003). On the other hand, one case of resection of an hippocampal malformation has been reported in Dericioglu et al. (2009).

Alzheimer's Disease In the antiquity, Greeks and Romans associated old age with mental decline (Berchtold & Cotman, 1998), but it is in 1901 that the psychiatrist Alois Alzheimer described the first case in a fifty-year-old woman of what became known as Alzheimer's disease. He publicly reported this case after the death of the patient on 1906.

Alzheimer's disease (AD) is a neuro-degenerative disorder (progressive loss of neurons) which mainly causes impairment of memory, and disorientation followed by other cognitive symptoms. AD patients present two types of lesions caused by

an accumulation of proteins leading to a cellular dysfunction, the amyloid plaques at an extra-cellular level and the neurofibrillary tangles (NFT) at an intra-cellular level. The medial temporal lobe and the hippocampus are affected by NFT and neuronal loss at the earliest stages of the disease. [Braak & Braak \(1991\)](#) divided the progression of NFT in the brain into six stages. Lesions are first located in the trans-entorhinal cortex area (stage I), then spread into the entorhinal cortex (stage II), extend to the hippocampus and the limbic lobe (stage III and IV), involve the associative neocortex (stage V) and finally the primary cortex (stage VI). These stages are related to cognitive impairments reflecting the degeneration of the brain related with these functions.

At present, the only way to obtain a definite diagnosis for AD is to perform an autopsy of the brain of probable AD sufferers, revealing the density and distribution of amyloid plaques and NFT. The diagnosis of probable AD relies on neuropsychological examination. It is thus important to make progress towards earlier and more accurate diagnosis of AD, by discovering markers of early AD. Volumetric MRI studies ([Laakso et al., 1995](#); [Convit et al., 1997](#); [Devanand et al., 2007](#)) highlighted the increased atrophy of the hippocampus. Shape studies allow to show a relation between hippocampal shape and AD in the earliest stages of the disease as in [Csernansky et al. \(2005\)](#); [Gerardin et al. \(2009\)](#).

Depression Depression is a mental disorder characterized by a decline of mood (as sadness), with a weak self-esteem and a loss of interest in normally pleasant activities. On MRI, differences between healthy subjects and depressed patients exist. Depressed patients present larger lateral ventricles, and smaller thalami, basal

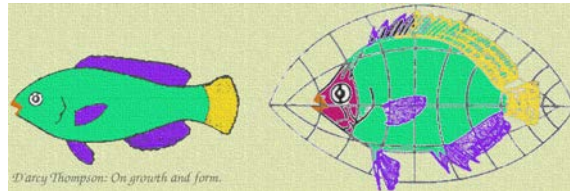
ganglia, frontal lobes and hippocampi. According to [Minkel \(2007\)](#) in a study with rats, there could exist a link between depression and neurogenesis. Furthermore, studies show a loss of hippocampal volume in major depression ([Bremner et al., 2000](#); [Sheline et al., 1996](#)). The loss of hippocampal neurons found in some depressed patients is related to a memory dysfunction and mood disorders. Medications may increase serotonin levels in the brain, stimulating neurogenesis and thus increasing the total mass of the hippocampus ([Duman et al., 1997](#)). This increase may help patients to improve mood and memory ([Sheline et al., 2003](#)).

Schizophrenia The term of schizophrenia was introduced by the psychiatrist Eugen Bleuler in 1911 to denote what was previously called "dementia praecox". Schizophrenia is a mental disorder usually developing in the beginning of the adulthood, and is often characterized by difficulties to recognize the real, which leads to abnormal social behaviours. Its origins can be genetics, social, and / or psychological. A post-mortem study ([Shenton et al., 1992](#)) showed that patients with schizophrenia had significant reductions in the volume of gray matter in the left anterior part of the hippocampus, the left parahippocampal gyrus and the left superior temporal gyrus. This result on hippocampi has been also observed by [Nelson et al. \(1998\)](#) who showed an association between schizophrenia and a bilateral volumetric reduction of the hippocampi and probably of the amygdalae as well.

2.4 Conclusion

We described the anatomy of the hippocampus and its embryological development. We also briefly reviewed its role in memory and cognition, and in some pathologies. We saw that there exists an anatomical variant of the hippocampus named Incomplete Hippocampal Inversion (IHI) which seems to be of developmental origin. This anatomical variant is present in healthy population and frequent in epilepsy patients. It is thought to be a normal and non-pathological variation of the hippocampus. We saw that IHI are not very well characterised since criteria used are not always the same, and the prevalence of IHI is not well known in the healthy population.

CHAPTER 3



COMPUTATIONAL ANATOMY

In 1917 with his book "On growth and form" (D'Arcy Thompson, 1917), the biologist and mathematician Sir D'Arcy Thompson became the pioneer of computational anatomy by using mathematics to explain biological patterns and variability. In this book he describes morphological changes between species of the same genus by simple geometric transformations. Therefore he introduced the problem of studying biological shapes variability.

Computational Anatomy is the study of the anatomy via the numerical analysis

of medical images. It aims at developing tools for the analysis of features of interest like volume in biological shapes, and the study of their variability within a population, to learn about shape differences between healthy and diseased populations or for the detection and the classification of pathologies using shapes of particular anatomical structures. Today, with the advances in medical imaging technology and the wider availability of neuroimaging facilities to acquire 3D images of the human brain like the non-invasive Magnetic Resonance Imaging (MRI). Thanks to the wider availability of neuroimaging facilities and the development of computing infrastructures there is more and more imaging datasets and larger ones, therefore Computational Anatomy is more and more used.

Many studies focus on the statistical analysis of volume measurements as for example [Hogan et al. \(2014\)](#) for the study of epilepsy, or [Hänggi et al. \(2011\)](#) for the study of Alzheimer's disease. But such studies do not capture the shape complexity of the structures observed in MRI. Analysing shapes of structures can provide a better understanding of the anatomical variability of the brain, which is a very challenging problem since healthy brains have a high variability, and it is important to understand the mechanisms, the morphological changes and the impacts of diseases, malformations or atypical variants of anatomical structures such as the Incomplete Hippocampal Inversion.

But before analysing the variability of an anatomical structure shape set, we have to define what we call a shape, how to represent the biological variability, and we need to know how to characterise them to define differences between shapes. Then we have to choose a way to analyse this shape set.

In this chapter I will first present the concept of shape and an overview of different ways to describe a shape, then I will present the shape descriptor we chose, before introducing the statistical shape analysis methods and the template estimation methods needed for the shape analysis.

3.1 Shapes and their numerical representation in medical imaging

The concept of shape is not well defined in the scientific community. Here we will define the shape of an object as the 2D or 3D outside contour which delimits the object from the background or from other objects.

3.1.1 Data acquisition

To study the anatomical variability of biological structures, we first need to acquire images. There are many ways to acquire images of structures (microscopes, ultra sound, X rays, magnetic resonance,...), but all of them are not appropriate or feasible, depending on the structure we are interested in. For the study of anatomical brain structures, the most common way to acquire images are volumetric MRI and CT-scan. In this work we only work with the non invasive T1 weighted MRI. Each subject recruited for the study has to be scanned by the MRI machine, in order to obtain a volumetric image of the brain.

3.1.2 Segmentation

After the acquisition it is now possible to identify the structure of interest. To extract the shape of the desired anatomical structure, we have different options: manual segmentation which is very time consuming and can lead to different results when made by another person, semi automatic segmentation which is more robust but still time consuming, and automated segmentation. In this work, we used an automated segmentation method to extract the hippocampus shapes from the MR images of our subjects. There are many methods for the segmentation of the hippocampus, some of them are based on anatomical landmark detection as [Chupin et al. \(2009\)](#) and [Fischl et al. \(2002\)](#) from the FreeSurfer software. Others are based on non linear alignment of an image to a probabilistic atlas as [Akhondi-Asl et al. \(2011\)](#) or [Pardoe et al. \(2009\)](#), or based on multi atlas approaches as [Collins & Pruessner \(2010\)](#). For our study we chose to use the SACHA software ([Chupin et al. \(2009\)](#)) which provides good segmentations in healthy populations as shown in the [Kim et al. \(2012\)](#) study. The segmentation methods provide a binary mask that will allow to represent the shape of the anatomical structure of interest.

A shape can be represented by a binary mask which represent the contour of the object, or by points in \mathbb{R}^2 or \mathbb{R}^3 eventually connected to each others to form piecewise smooth curves or piecewise smooth surfaces to form triangular meshes (tessellation of the shape surface by regular triangles), or by varifolds or currents, a concept I will present later in section 3.3.1. The representation of the shape depends on the choice of the shape descriptor required for the study.

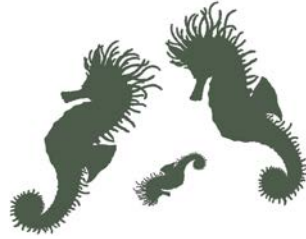


Figure 3.1: Three similar shapes.

3.2 Shape descriptors and dissimilarity

Shape descriptors as numerical quantities (scalars, vectors or matrices) extracted from the important features / information of the anatomical structures studied. A shape descriptor may be invariant to translation, scale and rotation. In Figure 3.1, the three objects have similar shapes: by applying a translation, a rotation and a scaling to two of these animals we can perfectly superimpose them on the third one. However in medical imaging, the scale of a shape should be part of the shape description, since anatomical structures vary in volume and shape, and abnormal variation of these features often characterises disease or malformation.

The choice of the descriptor has to be adapted to the data and the purpose. A shape descriptor is usually associated with a measure of dissimilarity. This dissimilarity function corresponds intuitively to a distance between shapes, and should indeed satisfy some of the mathematical properties of a distance function $dist$. As a reminder these properties are:

1. Symmetry, $dist(x, y) = dist(y, x)$ for any objects x and y
2. Positivity, $dist(x, y) \geq 0$ for any objects x and y .
3. Triangular inequality, for any objects x, y, z , $dist(x, y) \leq dist(x, z) + dist(z, y)$

4. $dist(x, x) = 0$ for any object x .
5. $dist(x, y) = 0 \Rightarrow x = y$ for any objects x and y .

The symmetry property and the triangular inequality may not be always satisfied in a dissimilarity function d . The symmetry property is not always necessary or wanted as explained in [Tangelder & Veltkamp \(2008\)](#). In fact, one has to choose between the quantity of shape information captured by the shape descriptor, and a dissimilarity function being closer to a distance function. Moreover, one may choose to incorporate invariance with respect to rigid transformations: $d(T(x), x) = 0$ for any described shape x and rigid transformation T , in which case the last property of a distance will not be satisfied. However in general, a rigid transformation is applied to all shapes before computing dissimilarities ; hence this last property is less crucial.

In the next two sections I will briefly present different shape descriptors, to give a short overview of the possible descriptors used in medical imaging.

3.2.1 Common shape descriptors

Basic descriptors Among the most basic shape descriptors, we can find measurements such as volume, length, perimeter, which are scalar values, and thus simply use the absolute value of the difference as dissimilarity. Another basic shape descriptor, which directly uses the segmentation, is the Voxel Based Morphometry (VBM) [Ashburner & Friston \(2000\)](#), which compares voxel by voxel the smoothed segmentation of the gray matter from brains of the subjects normalized in the same stereotactic space. In this method, the voxel-wise comparison is local and there is

no global dissimilarity.

Point Distribution Model This descriptor has been used in studies as [Becker et al. \(2010\)](#) to segment the cerebellum of fetuses. In the Point Distribution Model framework, the descriptors are specific 2D or 3D points which are points of correspondences named landmarks as in [Cootes et al. \(1995\)](#). These landmarks can be anatomical points specified by an expert corresponding to biological interest points, they can be located according to some geometrical properties such as curvature, or voxel intensity for example, as described in [Dryden & Mardia \(1998\)](#). Point Distribution Model (PDM) gives a local description of the shape which does not take into account some geometric informations such as tangents or normals to the shape. The main problem of such a descriptor is the use of landmarks which sometimes are very difficult to identify due to the complexity and variability of shapes such as for example human brain sulci.

Medial representation This descriptor has been used in studies such as [Styner et al. \(2004\)](#) in which they combine medial representation and spherical harmonics (section 3.2.1) for the study of the hippocampus in a pathological case, or as [Pouch et al. \(2012\)](#) to model mitral valve. Medial representation has been introduced by [Pizer et al. \(1999\)](#). It uses as descriptor the medial axis or skeleton of the shape, which captures the geometry in a compact manner. It allows to build low dimension statistical models of curves and surfaces. The principle is to link a set of primitives called medial atoms to form a graph. Medial atoms model a region of an object via its position, width and local orientation; a medial atom $m = (x, r, n_0, n_1)$ is a

4-tuple in $\mathbb{R}^3 \times \mathbb{R}^+ \times \mathbb{R}^3 \times \mathbb{R}^3$, with x a medial primitive which is the central position of the atom, r the radius of the maximal inscribed ball, n_1 and n_0 are two unit vectors tangents to the object boundary. This descriptor is not robust to changes of connectivity of the surfaces and is sensitive to the variations in the segmentation method used.

Spherical harmonic decomposition This descriptor is currently used in medical imaging to describe rounded or closed structures, as used in [Gerardin et al. \(2009\)](#) to classify Alzheimer disease patients from ageing subjects using hippocampal shape, or in [Ong et al. \(2012\)](#) for the analysis of the caudate nucleus. The spherical harmonic decomposition, is a global multi scale descriptor that can only represent objects of spherical topology. Spherical harmonics are the angular portions of the solution to Laplace equation in spherical coordinates and form an orthonormal set of basis function on the sphere. Truncating the spherical harmonic series at different degrees results in object representations at different levels of details. But this descriptor is not invariant to translations, rotations and scaling.

Intrinsic shape context This is a geometric descriptor introduced by [Shi et al. \(2007\)](#) used to capture global characteristics of shapes to guide the mapping between hippocampal surfaces by automatically detecting landmarks for the analysis of the hippocampal shape in Alzheimer Disease. The Intrinsic shape context (ISC) attributes to each point on the surface a measure reflecting its relative position to the other points by partitioning the surface in small areas. The ISC defines for each point p a histogram of the area around p , so it is invariant to rigid transformations.

A global partition of the shape can also be computed.

Moments representation Moments representation have been used in [Mangin et al. \(2004\)](#) to study the morphometry of cortical sulci. In 2D or 3D images, they indicate the shape distribution of each axis. First moments describe global and local geometric information of the shape, as the volume and the coordinates of the centre of mass. Moments are invariant to rigid transformations when using normalized central moments. It can be enough to consider the three first order moments to describe a shape, as they embed simple shape information like bending, tapering and pinching. The advantage of using moments of order up to three, is that a shape can be described by a small set of values. But the interpretation of such descriptors is not an easy task.

3.2.2 Deformation-based descriptors

In this section is presented another sort of descriptors: the deformation-based descriptors describe a shape by studying its non-rigid matching onto another one, or onto a template of the population. Indeed, in deformation-based analysis, we generally compute the deformations between the shapes to a template of the population. I will present in section 3.5 some methods used in the literature to estimate a template. With such a descriptor we build a metric on shapes via a metric on the space of deformations, so the dissimilarity is related to the deformation needed to match a surface to another. This sort of descriptor follows the idea of D'Arcy Thompson and was taken over by [Grenander & Miller \(1998\)](#). Here the distance

between shapes is determined using the quantity of deformation from a shape to another. Deformation-based descriptors can deal with any representation of shapes : images, surfaces, points and curves.

Here I quickly give an overview of the deformations models that have been widely used in medical images.

Free Form Deformation Free Form Deformations (FFD) have been introduced by [Sederberg & Parry \(1986\)](#) and applied to recover the motions and deformations of the breast in MRI in [Rueckert et al. \(1999\)](#). FFD deforms a shape by manipulating an underlying mesh of control points. Deformations are based on B-splines. A physical analogy is to consider a parallelepiped in flexible plastic (the control points) in which is embedded the object of interest which is also flexible; the object is then deformed along with the plastic.

Large Deformation Diffeomorphic Metric Mapping The Large Deformation Diffeomorphic Metric Mapping (LDDMM) framework has been used in many studies as in [Durrleman et al. \(2008b\)](#) for the study of the brain variability, or in [Auzias et al. \(2009\)](#) for the brain registration under sulcal constraints and used in [Vaillant et al. \(2004\)](#) to define tangent-space statistics using geodesics. The LDDMM framework introduced by [Trounev \(1998\)](#), is based on flows of diffeomorphisms which are the non-linear extension of linear isomorphisms, and allow the registration of different shapes. The main issue with using such a framework is the computation time which is very high, but the advantages make this framework very interesting (details in section 3.3.2).

Large Deformation High Dimensional Brain Mapping Wang et al. (2007b)

characterized the basal ganglia and the thalamus in patient with Tourette syndrome and Tepest et al. (2003) the hippocampal anatomy in schizophrenia using Large Deformation High Dimensional Brain Mapping (HDBM-LD) to quantify anatomical changes. Csernansky et al. (1998) introduced this method to study hippocampal abnormalities in schizophrenia using MRI. HDBM-LD consists in analysing transformations fields between landmarks of individual MRI and a template. Template is transformed with a diffeomorphic registration guided by the landmarks towards the MRIs of the subjects, then shapes are described by the vectors of displacements located on the template.

3.3 Chosen mathematical model

For our analysis we have decided to use a deformation-based descriptor, which is the most natural choice to use in computational anatomy, where the comparison of two shapes can be performed by the analysis of the deformation bringing one shape to another (Grenander & Miller, 1998). Morphological changes of anatomical brain structures are under physical properties constraints, such as rules of elastic deformations of fluid dynamics. The LDDMM framework (presented in section 3.3.2) appears to be the easiest to interpret, and the model has nice properties as we will see in section 3.3.2. To represent our shapes we have chosen to use the framework of currents Vaillant & Glaunès (2005) presented in section 3.3.1, which can be used with binary masks or meshes, does not require point to point correspondences or landmarks, and is robust to different samplings and topologies. The main advantage

of this framework is that shapes are embedded into a vector space.

3.3.1 Currents

The idea of the mathematical object named “currents” is related to the theory of distributions as presented by Schwartz in 1952 [Schwartz \(1952\)](#), in which distributions are characterized by their action on any smooth functions with compact support. In 1955, De Rham [De Rham \(1955\)](#) generalized distributions to differential forms to represent submanifolds, and called this representation currents. This mathematical object serves to model geometrical objects using a non parametric representation.

The use of currents in computational anatomy was introduced by [Vaillant & Glaunès \(2005\)](#) (see also [Glaunès \(2005\)](#)) and subsequently developed by Durrleman ([Durrleman, 2010](#)) in order to provide a dissimilarity measure between meshes which does not assume point-to-point correspondence between anatomical structures,. A very good presentation of the concept of currents in mathematics can be found in [Durrleman \(2010\)](#). The approach proposed by Vaillant and Glaunès is to represent meshes as objects in a linear space and supply it with a computable norm. Using currents to represent surfaces has some benefits. Firstly it avoids the point correspondence issue : one does not need to define pairs of corresponding points between two surfaces to evaluate their spatial proximity. Moreover, metrics on currents are robust to different samplings and topologies and take into account not only the global shapes but also their local orientations. Another important benefit is that the space of currents is a vector space, which allows to consider linear combinations

such as means of shapes in the space of currents. This property will be used in the centroid and template methods that we introduce in the following.

We limit the framework to surfaces embedded in \mathbb{R}^3 . Let S be an oriented compact surface, possibly with boundary. Any smooth and compactly supported differential 2-form ω of \mathbb{R}^3 - i.e. a mapping $x \mapsto \omega(x)$ such that for any $x \in \mathbb{R}^3$, $\omega(x)$ is a 2-form, an alternated bilinear mapping from $\mathbb{R}^3 \times \mathbb{R}^3$ to \mathbb{R} - can be integrated over S

$$\int_S \omega = \int_S \omega(x)(u_1(x), u_2(x)) d\sigma(x). \quad (3.1)$$

where $(u_1(x), u_2(x))$ is an orthonormal basis of the tangent plane at point x , and $d\sigma$ the Lebesgue measure on the surface S . Hence one can define a linear form $[S]$ over the space of 2-forms via the rule $[S](\omega) := \int_S \omega$. If one defines a Hilbert metric on the space of 2-forms such that the corresponding space is continuously embedded in the space of continuous bounded 2-forms, this mapping will be continuous [Vaillant & Glaunès \(2005\)](#), which will make $[S]$ an element of the space of 2-currents, the dual space to the space of 2-forms.

Note that since we are working with 2-forms on \mathbb{R}^3 , we can use a vectorial representation via the cross product: for every 2-form ω and $x \in \mathbb{R}^3$ there exists a vector $\bar{\omega}(x) \in \mathbb{R}^3$ such that for every $\alpha, \beta \in \mathbb{R}^3$,

$$\omega(x)(\alpha, \beta) = \langle \bar{\omega}(x), \alpha \times \beta \rangle = \det(\alpha, \beta, \bar{\omega}(x)), \quad (3.2)$$

Therefore we can work with vector fields $\bar{\omega}$ instead of 2-forms ω . In the following, with a slight abuse of notation, we will use $\omega(x)$ to represent both the bilinear alternated form and its vectorial representative. Hence the current of a surface S

can be re-written from equation 3.1 as follows:

$$[S](\omega) = \int_S \langle \omega(x), n(x) \rangle d\sigma(x) \quad (3.3)$$

with $n(x)$ the unit normal vector to the surface: $n(x) := u_1(x) \times u_2(x)$.

Then we define a Hilbert metric $\langle \cdot, \cdot \rangle_W$ on the space of vector fields of \mathbb{R}^3 , and require the space W to be continuously embedded in $C_0^1(\mathbb{R}^3, \mathbb{R}^3)$. The space of currents we consider is the space of continuous linear forms on W , i.e. the dual space W^* , and the required embedding property ensures that for a large class of oriented surfaces S in \mathbb{R}^3 , comprising smooth surfaces and also triangulated meshes, the associated linear mapping $[S]$ is indeed a current, i.e. it belongs to W^* .

The central object from the computational point of view is the reproducing kernel of space W , which we introduce here. For any point $x \in \mathbb{R}^3$ and vector $\alpha \in \mathbb{R}^3$ one can consider the Dirac functional $\delta_x^\alpha : \omega \mapsto \langle \omega(x), \alpha \rangle$ which is an element of W^* . The Riesz representation theorem then states that there exists a unique $u \in W$ such that for all $\omega \in W$, $\langle u, \omega \rangle_W = \delta_x^\alpha(\omega) = \langle \omega(x), \alpha \rangle$. u is thus a vector field which depends on x and linearly on α , and we write it $u = K_W(\cdot, x)\alpha$. Thus we have the rule

$$\langle K_W(\cdot, x)\alpha, \omega \rangle_W = \langle \omega(x), \alpha \rangle. \quad (3.4)$$

Moreover, applying this formula to $\omega = K_W(\cdot, y)\beta$ for any other point $y \in \mathbb{R}^3$ and vector $\beta \in \mathbb{R}^3$, we get

$$\begin{aligned} \langle K_W(\cdot, x)\alpha, K_W(\cdot, y)\beta \rangle_W &= \langle K_W(x, y)\beta, \alpha \rangle \\ &= \alpha^T K_W(x, y)\beta = \langle \delta_x^\alpha, \delta_y^\beta \rangle_{W^*}. \end{aligned} \quad (3.5)$$

$K_w(x, y)$ is a 3×3 matrix, and the mapping $K_w : \mathbb{R}^3 \times \mathbb{R}^3 \rightarrow \mathbb{R}^{3 \times 3}$ is called the reproducing kernel of the space W . Now, note that we can rewrite equation 3.3 as

$$[S](\omega) = \int_S \delta_x^{n(x)}(\omega) d\sigma(x) \quad (3.6)$$

Thus using equation 3.5, one can prove that for two surfaces S and T ,

$$\langle [S], [T] \rangle_{W^*}^2 = \int_S \int_T \langle n_S(x), K_w(x, y)n_T(y) \rangle ds(x)ds(y) \quad (3.7)$$

This formula defines the metric we use for evaluating spatial proximity between shapes. It is clear that the type of kernel one uses fully determines the metric and therefore will have a direct impact on the behaviour of the algorithms. We use scalar invariant kernels of the form $K_w(x, y) = h(\|x - y\|^2/\sigma_w^2)I_3$, where h is a real function such as $h(r) = e^{-r}$ (gaussian kernel) or $h(r) = 1/(1 + r)$ (Cauchy kernel), and σ_w a scale factor. In practice this scale parameter has a strong influence on the results; we will go back to this point later.

We can now define the optimal match between two currents $[S]$ and $[T]$, which is the diffeomorphism minimizing the functional

$$J_{S,T}(v) = \gamma E(v) + \|[\varphi_v(S)] - [T]\|_{W^*}^2 \quad (3.8)$$

This functional is non convex and in practice we use a gradient descent algorithm to perform the optimization, which cannot guarantee to reach a global minimum. We have observed empirically that local minima can be avoided by using a multi-scale approach in which several optimization steps are performed with decreasing values of the width σ_w of the kernel K_w (each step provides an initial guess for the next one).

In practice, surfaces are given as triangulated meshes, which we discretize in the space of currents W^* by combinations of Dirac functionals : $[S] \simeq \sum_{f \in S} \delta_{c_f}^{n_f}$, where the sum is taken over all triangles $f = (f^1, f^2, f^3)$ of the mesh S , and $c_f = \frac{1}{2}(f^1 + f^2 + f^3)$, $n_f = \frac{1}{2}(f^2 - f^1) \times (f^3 - f^1)$ denotes respectively the center and normal vector of the triangle. Given a deformation map φ and a triangulated surface S , we also approximate its image $\varphi(S)$ by the triangulated mesh obtained by letting ϕ act only on the vertices of S . This leads us to the following discrete formulation of the matching problem:

$$\begin{aligned}
J_{S,T}^d(\alpha) &= \gamma \int_0^1 \sum_{i=1}^n \alpha_i(t)^T K_V(x_i(t), x_j(t)) \alpha_j(t) dt \\
&+ \sum_{f, f' \in S} n_{\varphi(f)}^T K_W(c_{\varphi(f)}, c_{\varphi(f')}) n_{\varphi(f')} \\
&+ \sum_{g, g' \in T} n_g K_W(c_g, c_{g'}) n_{g'} - 2 \sum_{f \in S, g \in T} n_{\varphi(f)}^T K_W(c_{\varphi(f)}, c_g) n_g \quad (3.9)
\end{aligned}$$

where φ denotes the diffeomorphism associated to momentum vectors $\alpha_i(t)$ and trajectories $x_i(t)$, $x_i = x_i(0)$ being the vertices of mesh S , and where we have noted for any face f , $\varphi(f) = (\varphi(f^1), \varphi(f^2), \varphi(f^3))$. We note 3 important parameters, γ which controls the regularity of the map, σ_V which controls the scale in the space of deformations and σ_W which controls the scale in the space of currents.

There exist other frameworks similar to currents, such as varifolds which have been studied for Computational Anatomy by [Charon & Trounev \(2013\)](#), and which present a similar spirit to currents but without taking into account the shape orientation. Indeed, currents need to define orientations of curves or surfaces, which may be an issue when studying for example white matter fibers (in which orientation is ambiguous), or surfaces with spikes (because spikes in the currents have a ten-

dency to vanish in the currents framework). Indeed, in some cases, as for the study of fibres or surfaces with acute pikes, currents need to define orientations which is not required in the first case, cancelled in the second case and lead to registration problems. For hippocampal shapes, orientation of shapes is not a problem, since hippocampi do not present acute pikes.

3.3.2 LDDMM framework

3.3.2.1 Large Diffeomorphic Deformations.

The Large Diffeomorphic Deformation Metric Mapping framework allows to quantify the difference between shapes and provides a shape space representation: shapes of the population are seen as points in an infinite dimensional smooth manifold, providing a continuum between shapes of the population. In this framework a diffeomorphism deforms the whole space, not only a shape. We briefly recall that a diffeomorphism between two smooth manifolds, is a bijective map that has a smooth inverse, and a smooth manifold is a space that locally looks like to an euclidian space in which one can do calculus.

Diffeomorphisms as flows of vector fields. In the LDDMM framework, deformation maps $\varphi : \mathbb{R}^3 \rightarrow \mathbb{R}^3$ are generated by integration of time-dependent vector fields $v(x, \cdot)$ in an Hilbert space V , with $x \in \mathbb{R}^3$ and $t \in [0, 1]$. If $v(x, t)$ is regular enough, i.e. if we consider the vector fields $(v(\cdot, t))_{t \in [0, 1]}$ in $L^2([0, 1], V)$, where V is a Reproducing Kernel Hilbert Space (R.K.H.S.) embedded in the space of $C^1(\mathbb{R}^3, \mathbb{R}^3)$

vector fields vanishing at infinity, then the transport equation:

$$\begin{cases} \frac{d\phi_v}{dt}(x, t) = v(\phi_v(x, t), t) & \forall t \in [0, 1] \\ \phi_v(x, 0) = x & \forall x \in \mathbb{R}^3 \end{cases} \quad (3.10)$$

has a unique solution, and one sets $\varphi_v = \phi_v(\cdot, 1)$ the diffeomorphism induced by $v(x, t)$. The induced set of diffeomorphisms \mathcal{A}_V is a subgroup of the group of C^1 diffeomorphisms. To enforce velocity fields to stay in this space, one must control the energy

$$E(v) := \int_0^1 \|v(\cdot, t)\|_V^2 dt. \quad (3.11)$$

Metric structure on the diffeomorphisms group The induced subgroup of diffeomorphisms \mathcal{A}_V is equipped with a right-invariant metric defined by the rules: $\forall \varphi, \psi \in \mathcal{A}_V$,

$$\begin{cases} D(\varphi, \psi) = D(Id, \varphi^{-1} \circ \psi) \\ D(Id, \varphi) = \inf \left\{ \int_0^1 \|v(\cdot, t)\|_V dt ; v \in L^2([0, 1], V), \varphi_v = \varphi \right\} \end{cases} \quad (3.12)$$

$D(\varphi, \psi)$ represents the shortest length of paths connecting φ to ψ in the diffeomorphisms group. Moreover, as in the classical Riemannian theory, minimizing the length of paths is equivalent to minimizing their energy, and one has also:

$$D(Id, \varphi) = \inf \{ E(v) ; v \in L^2([0, 1], V), \varphi_v = \varphi \} \quad (3.13)$$

Discrete matching. Considering two surfaces S and T , the optimal matching between them is defined in an ideal setting, as the map φ_v minimizing $E(v)$ under the constraint $\varphi_v(S) = T$. In practice such an exact matching is often not feasible

and one writes inexact unconstrained matching functionals which minimize both $E(v)$ and a matching criterion which evaluates the spatial proximity between $\varphi_v(S)$ and T , as we will see in the next section.

In a discrete setting, when the matching criterion depends only on φ_v via the images $\varphi_v(x_i)$ of a finite number of points x_i (such as the vertices of the mesh S) one can show that the vector fields $v(x, t)$ which induce the optimal deformation map can be written via a convolution formula over the surface involving the reproducing kernel K_V of the R.K.H.S. V . This is due to the reproducing property of V ; indeed V is the closed span of vectors fields of the form $K_V(x, \cdot)\alpha$, and therefore $v(x, t)$ writes

$$v(x, t) = \sum_{i=1}^n K_V(x, x_i(t))\alpha_i(t), \quad (3.14)$$

where $x_i(t) = \phi_v(x_i, t)$ are the trajectories of points x_i , and $\alpha_i(t) \in \mathbb{R}^3$ are time-dependent vectors called momentum vectors, which parametrize completely the deformation. Trajectories $x_i(t)$ depend only on these vectors as solutions of the following system of ordinary differential equations:

$$\frac{dx_j(t)}{dt} = \sum_{i=1}^n K_V(x_j(t), x_i(t))\alpha_i(t), \quad (3.15)$$

for $1 \leq j \leq n$. This is obtained by plugging formula 3.14 for the optimal velocity fields into the flow equation 3.10 taken at $x = x_j$. Moreover, the energy $E(v)$ takes an explicit form as expressed in terms of trajectories and momentum vectors:

$$E(v) = \int_0^1 \sum_{i,j=1}^n \alpha_i(t)^T K_V(x_i(t), x_j(t))\alpha_j(t) dt. \quad (3.16)$$

These equations reformulate the problems in a finite dimensional Riemannian setting. Indeed $E(v)$ appears as the energy of the path $t \mapsto (x_i(t))_{1 \leq i \leq n}$ in the space

of landmarks $\mathcal{L}^n = \{\mathbf{x} = (x_i)_{1 \leq i \leq n}, x_i \neq x_j \quad \forall i, j\}$ equipped with local metric $g(\mathbf{x}) = K(\mathbf{x})^{-1}$, where $K_V(\mathbf{x})$ is the $3n \times 3n$ matrix with block entries $K_V(x_i, x_j)$, $1 \leq i, j \leq n$.

3.3.2.2 Geodesic equations and local encoding.

As introduced previously, the minimization of the energy $E(v)$ in matching problems can be interpreted as the estimation of a length-minimizing path in the group of diffeomorphisms \mathcal{A}_V , and also additionally as a length-minimizing path in the space of landmarks when considering discrete problems. Such length-minimizing paths obey some geodesic equations [Vaillant et al. \(2004\)](#) (distances are defined as in 3.12), which we write as follows in the case of landmarks (using matrix notations):

$$\begin{cases} \frac{d\mathbf{x}(t)}{dt} = K_V(\mathbf{x}(t))\boldsymbol{\alpha}(t) \\ \frac{d\boldsymbol{\alpha}(t)}{dt} = -\frac{1}{2}\nabla_{\mathbf{x}(t)} [\boldsymbol{\alpha}(t)^T K_V(\mathbf{x}(t))\boldsymbol{\alpha}(t)] , \end{cases} \quad (3.17)$$

Note that the first equation is nothing more than equation 3.15 which allows to compute trajectories $x_i(t)$ from any time-dependant momentum vectors $\alpha_i(t)$, while the second equation gives the evolution of the momentum vectors themselves. This new set of ODEs can be solved from any initial conditions $x_i(0), \alpha_i(0)$, which means that the initial momentum $\alpha_i(0)$ fully determines the subsequent time evolution of the system (since the $x_i(0)$ are fixed points). As a consequence, these initial momentum vectors encode all information of the optimal diffeomorphism. This is a very important point for applications, specifically for group studies, since it allows to analyse the set of deformation maps from a given template to the observed shapes by performing statistics on the initial momentum vectors located on the template

shape. We also can use geodesic shooting from initial conditions $x_i(0)\alpha_i(0)$ in order to generate any arbitrary deformation of a shape in the shape space.

3.4 Statistical shape analysis

Statistical models are needed to compare shapes. As in [Grenander \(1995\)](#) in this work, we consider the quantity of deformation from a shape to another, to be the distance between these two shapes, whereas the leftover of the deformation is considered as noise due to the absence of point to point correspondences.

A first strategy (presented in section 3.4.1) based on the manifold geometry consists in analysing the set of pairwise distances between subjects. Then, the distance matrix can be entered into analysis methods such as Isomap [Tenenbaum et al. \(2000\)](#), Locally Linear Embedding [Roweis & Saul \(2000\)](#), [Yang et al. \(2011a\)](#) or spectral clustering algorithms [Von Luxburg \(2007\)](#). A second strategy (presented in section 3.4.2) consists in analysing the deformations between the template of the population and the individual subjects. This is done by analysing the initial momentum vectors $\boldsymbol{\alpha}^i(0) = (\alpha_p^i(0))_{p=1\dots n} \in \mathbb{R}^{3 \times n}$ which encode the optimal diffeomorphisms computed from the matching between a centroid and the subjects S_i . Initial momentum vectors all belong to the same vector space and are located on the vertices of the centroid.

3.4.1 Geometry based methods

3.4.1.1 Distance matrix approximation

In the LDDMM setting, distances can be computed by using diffeomorphic distances: $\rho(S_i, S_j) = D(id, \varphi_{ij})$. However, for large datasets, computing all pairwise deformation distances is computationally very expensive, as it involves $O(N^2)$ matchings. An alternative is to approximate the pairwise distance between two subjects through their matching from a template shape (see next section 3.5). This approach has been introduced in Yang et al [Yang et al. \(2011b\)](#). One can use a first order approximation to estimate the diffeomorphic distance between two subjects:

$$\tilde{\rho}(S_i, S_j) = \sqrt{\langle \boldsymbol{\alpha}^j(0) - \boldsymbol{\alpha}^i(0), K_V(\mathbf{x}(0))(\boldsymbol{\alpha}^j(0) - \boldsymbol{\alpha}^i(0)) \rangle}, \quad (3.18)$$

with $\mathbf{x}(0)$ the vertices of the estimated centroid or template and $\boldsymbol{\alpha}^i(0)$ is the vector of initial momentum vectors computed by matching the template to S_i . Using such approximation allows to compute only N matchings instead of N^2 .

Note that $\rho(S_i, S_j)$ is in fact the distance between S_i and $\varphi_{ij}(S_i)$, and not between S_i and S_j due to the non exactness of matchings. $\rho(S_i, S_j)$ is a dissimilarity between S_i and S_j .

ISOMAP This method was introduced by [Tenenbaum et al. \(2000\)](#) and tries to encode the global geometry of the manifold in a lower dimensional space. The ISOMAP method uses a distance matrix, which in the LDDMM setting is composed by the approximated geodesic distances described above. The matrix is then thresholded using a threshold or by using the k nearest neighbours to form a graph. The Multidimensional Scaling (MDS) method (a linear embedding method aiming at

conserving pairwise distances of a given distance matrix [Cox & Cox \(2010\)](#)) is then applied to the resulting graph in order to compute the low-dimensional embedding. ISOMAP is sensitive to populations with low density or with density differences as some of the next methods.

Locally linear embedding This local method (LLE) was introduced by [Roweis & Saul \(2000\)](#) and also builds a graph from a distance matrix by using the k nearest neighbours of each subject. Then the linear reconstruction in the high dimensional space is built using the graph by minimizing the sum of the reconstruction errors of the local neighbourhood. The low dimensional embedding is built by using the local information of each point, so the global aspect of the manifold is not necessarily respected.

Hessian eigenmaps This method is inspired by the previous LLE. It is also a local method based on a graph built using the k nearest neighbours, presented by [Donoho & Grimes \(2003\)](#). Then a tangent space is computed via a Principal Component Analysis (PCA) to each point of the manifold. The low dimensional embedding is computed using the Hessian operator.

Local tangent space alignment Another local method based on a graph computed using the k -NN from the approximated distances matrix, this method was presented by [Zhang & Zha \(2004\)](#). Tangent spaces are computed on each point of the manifold via a PCA, then the method tries to optimize the alignment of the local tangent spaces to compute the low dimensional embedding.

3.4.2 Principal component analysis on initial momentum vectors

The Principal Component Analysis (PCA) on initial momentum vectors from a template (see next section 3.5) to the subjects of the population, is an adaptation of Principal Component Analysis (PCA) in which Euclidean scalar products between observations are replaced by scalar products using the kernel K_V of the deformation space V , associated to the R.K.H.S. V . This adaptation can be seen as a Kernel PCA method (Schölkopf et al., 1997) on initial momentum vectors. PCA on initial momentum vectors has previously been used in morphometric studies in the LD-DMM setting Vaillant et al. (2004); Wang et al. (2007a); Durrleman et al. (2009), and it is sometimes referred to tangent PCA.

We briefly recall that, in PCA, the principal components of a dataset of N observations $\mathbf{a}^i \in \mathbb{R}^P$ with $i \in \{1, \dots, N\}$ are defined by the eigenvectors of the covariance matrix C with entries:

$$C(i, j) = \frac{1}{N-1} (\mathbf{a}^i - \bar{\mathbf{a}})^t (\mathbf{a}^j - \bar{\mathbf{a}}) \quad (3.19)$$

with \mathbf{a}^i given as a column vector, $\bar{\mathbf{a}} = \frac{1}{N} \sum_{i=1}^N \mathbf{a}^i$, and \mathbf{x}^t denotes the transposition of a vector \mathbf{x} .

In our case, our observations are initial momentum vectors $\boldsymbol{\alpha}^i \in \mathbb{R}^{3 \times n}$ and instead of computing the Euclidean scalar product in $\mathbb{R}^{3 \times n}$, we compute the scalar product with matrix K_V , which is a natural choice because it corresponds to the inner product of the corresponding initial vector fields in the space V . The covariance

matrix then writes:

$$C_V(i, j) = \frac{1}{N-1}(\boldsymbol{\alpha}^i - \bar{\boldsymbol{\alpha}})^t K_V(\boldsymbol{x})(\boldsymbol{\alpha}^j - \bar{\boldsymbol{\alpha}}) \quad (3.20)$$

with $\bar{\boldsymbol{\alpha}}$ the vector of the mean of momentum vectors, and \boldsymbol{x} the vector of vertices of the template surface. We denote $\lambda_1, \lambda_2, \dots, \lambda_N$ the eigenvalues of C in decreasing order, and $\boldsymbol{\nu}^1, \boldsymbol{\nu}^2, \dots, \boldsymbol{\nu}^N$ the corresponding eigenvectors. The k -th principal mode is computed from the k -th eigenvector $\boldsymbol{\nu}^k$ of C_V , as follows:

$$\boldsymbol{m}^k = \bar{\boldsymbol{\alpha}} + \sum_{j=1}^N \nu_j^k (\boldsymbol{\alpha}^j - \bar{\boldsymbol{\alpha}}). \quad (3.21)$$

The cumulative explained variance CEV_k for the k first principal modes is given by the equation:

$$CEV_k = \frac{\sum_{h=1}^k \lambda_h}{\sum_{h=1}^N \lambda_h} \quad (3.22)$$

We can use geodesic shooting along with any principal mode \boldsymbol{m}^k to visualise the corresponding deformations.

We chose to use this statistical approach since Kernel-PCA is widely used in shape analysis as in [Vaillant et al. \(2004\)](#), [Pennec \(2006\)](#), [Durrleman et al. \(2009\)](#), [Shen et al. \(2012\)](#) or [Mansi et al. \(2011\)](#), and provides a low dimensional generative space which allows visualizing the effect of each principal component by using geodesic shootings.

3.5 Template estimation

A central notion in computational anatomy is the generation of registration maps, mapping a large set of anatomical data to a common coordinate system to study

intra-population variability and inter-population differences.

Several methods have been proposed to estimate templates in the LDDMM framework [Vaillant et al. \(2004\)](#); [Glaunès & Joshi \(2006\)](#); [Durrleman et al. \(2008a, 2012\)](#); [Ma et al. \(2008\)](#). [Vaillant et al. \(2004\)](#) proposed a method based on geodesic shooting which iteratively updates a shape by shooting towards the mean of directions of deformations from this shape to all shapes of the population. A different approach was proposed by [Durrleman et al. \(2008a, 2012\)](#). The method initializes the template with a standard shape, in practice it is often an ellipsoid. The method uses a forward scheme: deformations are defined from the template to the subjects. Again, it optimizes at the same time the deformations and the template. The template is composed by one surface which presents the same configuration as the initial ellipsoid. The method proposed by [Beg et al. \(2005\)](#) initializes the template with one subject of the population. The method computes the momentum vectors from the template to the subjects of the population, the template is updated by shooting in the direction of the mean of the momentum vectors until convergence. The method presented by [Ma et al. \(2008\)](#) introduces an hyper template which is an extra fixed shape (which can be a subject of the population). The method aims at optimizing at the same time deformations from the hyper template to the template and deformations from the template to subjects of the population. The template is optimized via the deformation of the hyper template, not directly.

In the following studies, we used the method introduced by [Glaunès & Joshi \(2006\)](#) which estimates a variational template given a collection of unlabelled points sets or surfaces in the framework of scalar measures and currents. In our case we use

the framework of currents. This method is posed as a minimum mean squared error estimation problem and uses the metric on the space of diffeomorphisms. Let S_i be N surfaces in \mathbb{R}^3 (i.e. the whole surface population). Let $[S_i]$ be the corresponding current of S_i , or its approximation by a finite sum of vectorial Diracs. The problem is formulated as follows:

$$\{\hat{v}_i, \hat{\mathcal{T}}\} = \arg \min_{v_i, \mathcal{T}} \sum_{i=1}^N \{\|\mathcal{T} - [\varphi_{v_i}(S_i)]\|_{W^*}^2 + \gamma E(v_i)\}, \quad (3.23)$$

where the minimization is performed over the spaces $L^2([0, 1], V)$ for the velocity fields v_i and over the space of currents W^* for \mathcal{T} . The method uses an alternated optimization i.e. surfaces are successively matched to the template, then the template is updated and this sequence is iterated until convergence. One can observe that when φ_i is fixed, the functional is minimized when \mathcal{T} is the average of $[\varphi_i(S_i)]$ in space W^* :

$$\mathcal{T} = \frac{1}{N} \sum_{i=1}^N [\varphi_{v_i}(S_i)], \quad (3.24)$$

which makes the optimization with respect to \mathcal{T} straightforward. This optimal current is not a surface itself; in practice it is constituted by the union of all surfaces $\varphi_{v_i}(S_i)$, and the $\frac{1}{N}$ factor acts as if all normal vectors to these surfaces were weighted by $\frac{1}{N}$. At the end of the optimization process however, all surfaces being co-registered, the $\hat{\varphi}_{v_i}(S_i)$ are close to each other, which makes the optimal template $\hat{\mathcal{T}}$ close to being a true surface.

In practice, we stop the template estimation method after P loops, and with the datasets we use, $P = 7$ seems to be sufficient to obtain an adequate template: the

algorithm has converged, and adding more loops does not increase significantly the quality of the template.

As detailed in section 3.4, obtaining a template allows to perform statistical analysis of the deformation maps via the initial momentum representation from template to subjects to characterize the population.

In the present case, the optimal template for the population is not a true surface but is defined, in the space of currents, by the mean $\hat{\mathcal{T}} = \frac{1}{N} \sum_{j=1}^N \hat{\varphi}_{v_j} [S_j]$. However this makes no difference from the point of view of statistical analysis, because this template can be used in the LDDMM framework exactly as if it was a true surface.

One may speed up the estimation process and avoid local minima issues by defining a good initialization of the optimization process. Standard initialization consists in setting $\mathcal{T} = \frac{1}{N} \sum_{i=1}^N [S_i]$, which means that the initial template is defined as the combination of all unregistered shapes in the population. Alternatively, if one gives a good initial guess \mathcal{T} , the convergence speed of the method can be improved. This was the primary motivation for the introduction of the iterative centroid method which we present in chapter 5.

3.6 Conclusion

Various methods for shape analysis have been proposed in computational anatomy for the analysis of anatomical variability of brain structures. There is currently no consensus on the shape representation neither on the shape descriptor; this choice depends on the structure considered. In our case we chose to use the framework of currents to represent our hippocampal shapes, and the LDDMM framework to

describe them. In the following, we will see that template estimations methods in the LDDMM framework are computationally expensive, which makes difficult the analysis of large databases. We will present in Chapter 5 a method which computes a centroid shape and allows to save computation time. This centroid computation will be used further as a starting point for our statistical analyses.

SECOND PART



CONTRIBUTIONS

CHAPTER 4



EVALUATION OF INCOMPLETE HIPPOCAMPAL INVERSIONS

In this chapter, we will study Incomplete Hippocampal Inversion (IHI) in young and healthy subjects. To that purpose, we will propose a new set of criteria for the visual evaluation of IHI, adapted from existing criteria from the literature. Using these criteria, we will then study the prevalence and characteristics of IHI in healthy subjects using over 2000 subjects from the IMAGEN database.

This chapter is organised as follow: I first present and discuss in section 4.1 the criteria used in the literature and in section 4.2 the population who served for the

study, before presenting in section 4.3 the simplified criteria used to evaluate the 2042 subjects of the IMAGEN database. A short section in 4.4, expose how hippocampi have been segmented and the quality control. Experimentations are exposed in section 4.5 and results are finally presented in the section 4.6 and discussed in section 4.7.

4.1 Introduction

Incomplete hippocampal inversion (IHI) is an atypical anatomical pattern of the hippocampus which prominent features are a round, verticalized, medially positioned hippocampus and a deep collateral sulcus. Different terms have been used to refer to this atypical pattern including “incomplete hippocampal inversion” (Bajic et al., 2008; Raininko & Bajic, 2010), “hippocampal malrotation” (Barsi et al., 2000; Peltier et al., 2005; Gamss et al., 2009), “abnormal hippocampal formation” (Bernasconi et al., 2005), “developmental changes of the hippocampal formation” Baulac et al. (1998). IHI are thought to be of developmental origin, as shown by studies in neonates (Righini et al., 2006; Raininko & Bajic, 2010). IHI were mostly described in patients with epilepsy, in particular with malformations of cortical development but also in temporal lobe epilepsy Baulac et al. (1998); Lehericy et al. (1995); Bernasconi et al. (2005); Bajic et al. (2009), with a prevalence of 30%-50%. However, IHI are not specific of patients with epilepsy and are also found in healthy subjects, although with an apparently lower frequency (Bronen & Cheung, 1991; Bajic et al., 2008; Bernasconi et al., 2005). Several studies have investigated the prevalence of IHI in subjects without seizures (Peltier et al., 2005; Bernasconi et al., 2005; Bajic et al.,

2009; Gamss et al., 2009; Bajic et al., 2008). However, these studies included a small number of healthy subjects (Bajic et al., 2008; Bernasconi et al., 2005), leading to an imprecise estimation of the prevalence of IHI, or included patients without epileptic seizures but referred for other neurological conditions (Gamss et al., 2009; Bajic et al., 2008). Therefore, the prevalence of IHI in healthy subjects remains unclear. The purpose of our study was to investigate the prevalence of IHI in a large population of healthy subjects. We used the European database IMAGEN (Schumann et al., 2010) composed of young healthy subjects. An advantage of using such database is the number of subjects (over 2000 subjects), the small age range, and the youth of the subjects which avoids the occurrence of age-related morphological changes that can make more difficult the visual assessment of IHI. The presence of IHI can be assessed visually on magnetic resonance imaging (MRI) data, usually using T1-weighted sequences. However, different criteria have been used in the literature to assess IHI, making it difficult to compare results across studies (Gamss et al., 2009; Raininko & Bajic, 2010). Moreover, these visual scales differ in terms of number of features to assess; those with many features are not practical for application to larger series of over 1,000 subjects. In this chapter, we adapted existing criteria from the literature in order to propose a new visual scale of IHI that includes the most representative published criteria of IHI (Bernasconi et al., 2005; Baulac et al., 1998), includes a reasonable number of items and leads to a robust assessment.

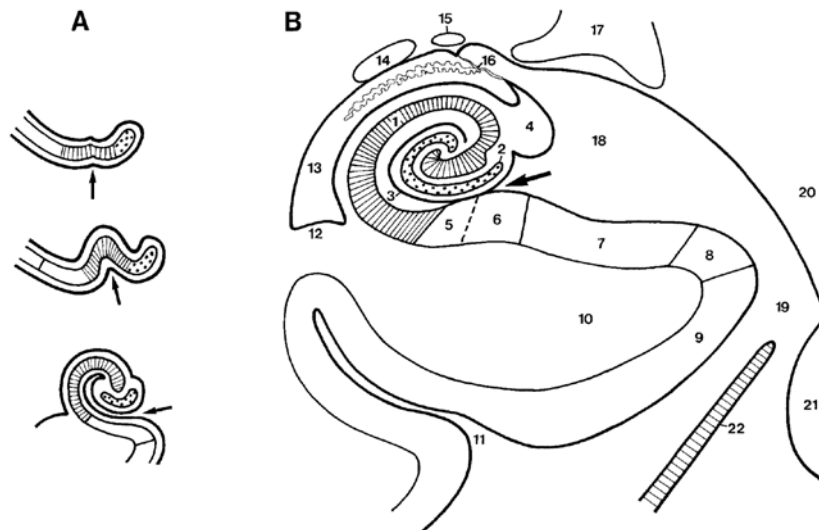


Figure 4.1: Figure from the third edition of *The Human Hippocampus* book of Duvernoy [Duvernoy \(2005\)](#). Figure A: Development of the gyrus dentatus (dotted area) and the Cornus Ammonis (hatched area). Figure B: Their definitive disposition. Arrows indicate the hippocampal sulcus (superficial part). 1, Cornus Ammonis; 2, gyrus dentatis; 3, hippocampal sulcus (deep or vestigial part); 4, fimbria; 5, prosubiculum; 6, subiculum proper; 7, presubiculum; 8, parasubiculum; 9, entorhinal oarea; 10, parahippocampal gyrus; 11, collateral sulcus; 12, collateral eminence; 13, temporal (inferior) horn of the lateral ventricle; 14, tail of caudate nucleus; 15, stria terminalis; 16, choroid fissure and choroid plexuses; 17, lateral geniculate body; 18, lateral part of the transverse fissure; 19, ambient cistern; 20, mesencephalon; 21, pons; 22, tentorium cerebelli.

4.1.1 Review of the Incomplete Hippocampal Inversion

As presented previously on the section 2.1 of Chapter 2, the Incomplete Hippocampal Inversion (IHI) is a normal anatomical variation of the standard hippocampus shape, which is not pathological. Some studies ([Humphrey \(1967\)](#), [Kier et al. \(1995\)](#), [Kier et al. \(1997\)](#), [Righini et al. \(2006\)](#), [Bajic et al. \(2010\)](#), [Radoš et al. \(2006\)](#), [Baker & Barkovich \(1992\)](#)) show an interest in the development of the hippocampus (see Figure 4.1) which starts before 10 gestational weeks. When

the corpus callosum grows at 16 GW, the gyrus dentatus and the cornu Ammonis start to infold, the hippocampus fissure remains open, and the hippocampus reduces in size to only occupy the medial part of the temporal lobe and then begins its inversion which will be ended around the 30th GW. 14% of neonates present an incomplete inversion of the hippocampus (characterized by a rounded shape) after 29 GW against 50% around 23-24 GW (Bajic et al. (2010)); the aspect of the hippocampus and the frequency of IHI seem to be similar to the adult hippocampi from 25 GW. Furthermore, the angle between the line connecting the lateral border of the cornu Ammonis with the medial superior border of the subiculum and the midline of the brain, is inferior to 70 degrees for fetuses before 25 GW, and superior to 70 degrees around 30 GW and more (Righini et al. (2006)). All these studies tell us that incomplete inversions of the hippocampus found in adult population of developmental origin, and that rounded shape and vertical orientation are characteristics of foetal hippocampi which inversion is still not completed.

In studies on patients with epilepsy or brain malformations the prevalences of IHI found in the literature are very different.

- In Barsi et al. (2000), they found 6% of IHI in the population composed by 597 patients with suspicion of epilepsy, 69% of the IHI were left-sided, 19% right-sided and 12% bilateral.
- In Peltier et al. (2005), 14% of 97 epileptic patients present IHI. In Bernasconi et al. (2005), 43% of the 30 temporal lobe epilepsy patients had IHI, and 49% of 76 patients with malformations of cortical development had IHI.
- In Bajic et al. (2009), 30% of the 201 patients with epilepsy had IHI, 67% of

the IHI were left-sided, 7% right-sided and 27% bilateral.

- For the developmental brain malformations [Baker & Barkovich \(1992\)](#) found IHI on 36% of 36 patients.
- [Sato et al. \(2001\)](#) found IHI on 64% of 44 patients with congenital brain malformations.
- [Donmez et al. \(2009\)](#) found IHI on 56% of 62 patients with congenital brain malformations.

In studies with control population (or patients without seizures nor brain malformations) we also find very different IHI prevalences.

- In [Bernasconi et al. \(2005\)](#) they found 10% of IHI in the control population composed by 50 healthy controls.
- In [Peltier et al. \(2005\)](#), 6% of the control population composed by 50 subjects including 11 patients without epilepsy nor brain malformations.
- In [Bajic et al. \(2009\)](#) authors used 150 subjects including 116 patients without brain malformation nor epilepsy, and found 18% of IHI, mostly left-side and no right-side.
- In [Gamss et al. \(2009\)](#), the population is composed by 497 patients without epilepsy seizures, only 6 patients present IHI.
- In [Bajic et al. \(2008\)](#), the population is composed by 20 volunteers and 80 patients without brain malformations, 19% had IHI.
- In one study ([Bronen & Cheung, 1991](#)) authors used 29 volunteers for the study of the normal variations of the hippocampal shape in the healthy population, authors found that 21% of the population do not have the usual flat appearance

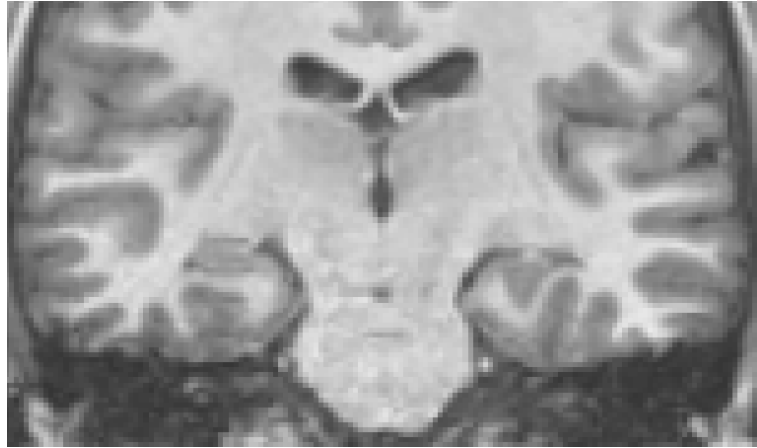


Figure 4.2: coronal view of a T1-weighted MRI in the MNI space from a subject of the database IMAGEN. On the right (left hippocampus) an IHI, and on the left a standard hippocampus

as in Figure 4.2.

We can note that the estimated frequencies, both for patient populations and control populations, are substantially different even if we can sometimes observe a higher frequency on epileptic population and developmental brain malformation population. But as previously said, these frequencies are not comparable since they are not using the same criteria to define IHI, and generally, populations are too small.

4.1.2 Criteria used in the literature

[Baker & Barkovich \(1992\)](#) were the first to mention abnormal shape, vertical orientation and incomplete inversion in the case of populations of patients with developmental brain anomalies, but this study was an observation, therefore they do not define criteria to evaluate IHI.

Presently the criteria used in the literature to define IHI are mainly inspired by those listed by [Baulac et al. \(1998\)](#) to describe, at the level of the hippocampus body in a coronal view, isolated (with normal temporal lobe) hippocampal formation development changes:

1. A medial position of the hippocampus close to the midline, leaving empty the choroid fissure, which was not enlarged and displayed the form of a thin crescent.
2. Round or pyramidal shape and vertical orientation by opposition to the ovoid shape and transversal orientation of the normal hippocampus.
3. Deep collateral sulcus inducing a very marked protrusion, or collateral eminence into the temporal horn.
4. The hippocampal fissure could not be identified or was abnormally deep.
5. The fimbria was less well delineated or misplaced on the dorsolateral edge of cornu Ammonis.
6. A thickened subicular cortical ribbon.

The study of [Barsi et al. \(2000\)](#) used similar criteria to the *2nd* and the *3rd* criterion presented by Baulac et al.. Other criteria are: blurred internal structure (which reminds the first part of the *4th* criterion of [Baulac et al. \(1998\)](#): "hippocampal fissure could not be identified"), normal signal intensity on T2-weighted images, abnormal position and size of the fornix. The main problem of all these criteria is that none of them is proposed with a threshold, each estimation is entirely subjective, and authors do not say why they chose these specific criteria as the size of the fornix for example. In the study of [Bernasconi et al. \(2005\)](#), authors based their criteria on the

[Baulac et al. \(1998\)](#) study, and aimed at better defining some criteria, such as the medial positioning and the vertical orientation of the hippocampus. But authors are still not precise, indeed for the medial positioning they expect a distance they defined to be shortened, without a threshold. For the vertical orientation they measure an angle, and for this criterion this angle has to be acute without more precision, this angle seems to be difficult to estimate in case of rounded shape (see figure 3C of the study, the description of the angle is at figure 3E). This study evaluated IHI on the head, the body and the tail of the hippocampus, they illustrated some of the criteria in the head and the tail, but criteria were exposed for hippocampal body. In [Peltier et al. \(2005\)](#), they used similar criteria to those presented in Baulac et al. to evaluate their hippocampi: the rounded shape, abnormal orientation, the visibility of internal structures (on T2-weighted MRI), a deep and verticalised collateral sulcus and a medial positioning. Authors do not give more informations. The study [Bajic et al. \(2008\)](#) used the following criteria: round or pyramidal shape, hippocampus on the medial part of the choroidal fissure (which corresponds to the medial position), the tip of the temporal horn, the orientation of the collateral sulcus, the long axis of the choroidal fissure (impossible to evaluate on T1-weighted MRI), and the medial position of the fimbria which is used to evaluate the criterion of medial positioning in [Baulac et al. \(1998\)](#) and [Bernasconi et al. \(2005\)](#).

There are different ways to evaluate the positioning of the hippocampi for example, or to determine its verticality. But we can note that in those studies there are recurring criteria, as 1; the roundness, 2; the verticality of the collateral sulcus, 3; the medial positioning and 4; the thickened subiculum, and these criteria also have

Table 4.1: Characteristics of the studied population

Imaging centres	Number of subjects	Gender	Age (years) mean \pm SD (range)	Handedness (Right/Left/Both)
Total	2008	1029 F (51%)	14.5 \pm 0.4(12.9 – 17.2)	1740/218/14

the advantage to be evaluable on a large database because they are always visible. That is why we decided to base our description on these 4 criteria. We added a 5th criterion on the depth of sulci of the fusiform gyrus (T4), since we observed that it is not always the collateral sulcus which is deep and close to the hippocampus.

4.2 Participants and MRI data

We studied young healthy subjects from the multi-centric European database IMAGEN¹ (Schumann et al., 2010). The database comprises 2462 subjects with high-resolution T1-weighted anatomical MRI. For all subjects, T1-weighted MRI were acquired on 3 Tesla scanners (Siemens Verio and TimTrio, Philips Achieva, General Electric Signa Excite and Signa HDx) using a 3D Magnetization Prepared Rapid Acquisition Gradient Echo (MPRAGE) sequence (TR = 2,300 msec; TE = 2.8 msec, flip angle = 9°; resolution: 1x1x1 mm³). We performed quality control of the MRI data, checking for general quality as well as specific visibility of the hippocampal formations. The MRI was judged of sufficient quality for assessment of IHI for 2008 subjects, which were entered into the study (characteristics of the subjects are given in Table 4.1). T1-weighted MRIs were registered towards the MNI152 atlas using the FSL software (Jenkinson & Smith, 2001; Smith et al., 2004)

1. <http://www.imagen-europe.com/>

in order to perform IHI assessment with a standardized orientation.

4.3 Simplified individual criteria and global criterion for IHI assesment

An IHI is globally characterized by a round and vertical shape of the hippocampus, a deep collateral sulcus and a medial positioning. For rating IHI, five individual criteria and a global criterion named $C0$ were defined.

4.3.1 Criterion $C1$: verticality and roundness of the hippocampus body

4.3.1.1 Description

Criterion $C1$ assesses both the roundness of the hippocampal body and its verticality. Some studies have considered roundness and verticality simultaneously (Bernasconi et al., 2005; Lehericy et al., 1995), while others have considered them separately (Baulac et al., 1998) or have considered only the roundness (sometimes referred to as pyramidal shape) (Bajic et al., 2008; Barsi et al., 2000; Gamss et al., 2009; Stiers et al., 2010). In our case, we considered roundness and verticality as a single criterion, in order to limit the number of criteria.

Criterion $C1$ was evaluated on the hippocampal body, on coronal slices. The principles used to evaluate this criterion are illustrated on Figure 4.3 Two segments $C1_a$ and $C1_b$ are determined. Segment $C1_a$ represents the width of the hippocampus

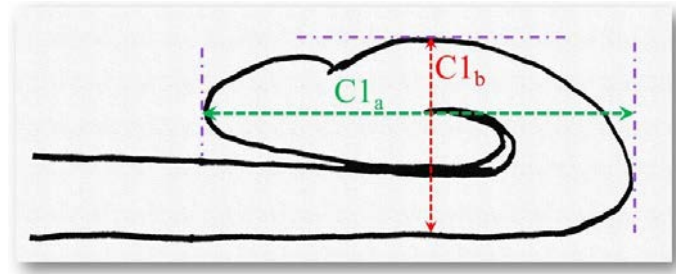


Figure 4.3: Criterion $C1$: roundness and verticality of the hippocampus. For roundness, the hippocampus is considered flat when $C1_a \gg C1_b$, round when $C1_a \simeq C1_b$, and ovoid when $C1_a \ll C1_b$. The verticality of the hippocampus is determined by the verticality of the segment $C1_a$

in a coronal view; it is parallel to the ventral part of CA1/subiculum and goes from the medial part of the gyrus dentatus to the lateral part of CA1. Segment $C1_b$ measures the height of the hippocampal body in a coronal view; $C1_b$ must be perpendicular to segment $C1_a$ and goes from the dorsal part of the hippocampus to the ventral part of CA1.

The roundness is evaluated on three levels, flat ($C1_a > C1_b$) round ($C1_a = C1_b$) or oval ($C1_a < C1_b$). For the verticality three levels were used: horizontal if the segment $C1_a$ is horizontal (with a tolerance of around 10 degrees), oblique if $C1_a$ is neither horizontal nor vertical (around 45 degrees) and vertical if segment $C1_a$ is vertical with also a tolerance of around 10 degrees. Segments $C1_a$ and $C1_b$ are here to illustrate and help the new observer to understand the criterion. The evaluation of the MRI is made without tracing such segments. When roundness and verticality have been determined, they are reported to determine the grade for the $C1$ criterion following the rules defined in Table 4.2.

Table 4.2: Evaluation of the criterion $C1$, based on the verticality and roundness of the hippocampus.

		Verticality of segment a		
		horizontal	oblique	vertical
Form	flat	0	0.5	NA
	round	0.5	1	2
	oval	1	1.5	2

4.3.1.2 Examples

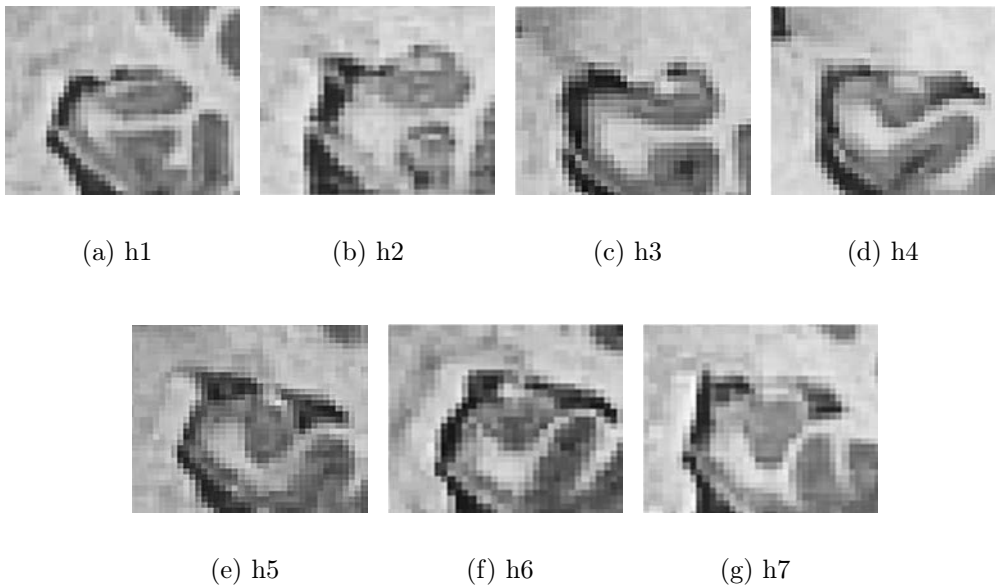


Figure 4.4: Examples for the evaluation of the $C1$ criterion. Which grades for these 7 hippocampi from (a) to (g)? Results are detailed in Table 4.3 and in Figure 4.5.

The learning phase consists in accustom the new observer to recognize when an hippocampus is flat and horizontal, round and oblique or round and vertical at first sight, and the duration of this learning phase varies if the reader is already used to

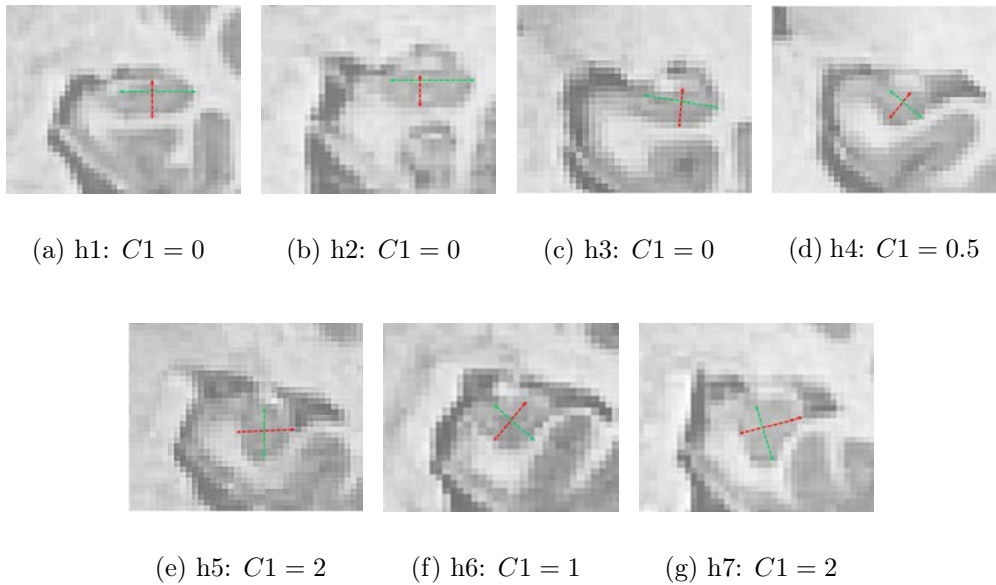


Figure 4.5: Results of the Figure 4.4 Segments are here only for helping the reader, they are not displayed on the MRI.

observe hippocampi on MRI.

Once the new observer is accustomed with this $C1$ criterion, he can easily say that the 3 first hippocampi on the Figure 4.4 , h1 to h3 have a null grade, likewise for the hippocampus h6 which is round and oblique it obtains a grade 1, and the hippocampi h5 and h7 which are vertical obtain a grade of 2. For the hippocampus h4, the large (compared to the hippocampus) gray area is in fact the fimbria, so we do not have to take it into account. The hippocampus h4 is oblique and flat, the grade is 0.5.

Table 4.3: Results of the C1 evaluation for hippocampus on Figure 4.4. "Hor" is for horizontal, "Obl" for oblique and "Ver" for vertical.

C1 evaluation	h1	h2	h3	h4	h5	h6	h7
roundness	$a > b$	$a > b$	$a > b$	$a > b$	$a = b$	$a = b$	$a = b$
verticality	Hor	Hor	Hor	Obl	Ver	Obl	Ver
grade	0	0	0	0.5	2	1	2

4.3.2 Criterion C2: collateral sulcus

4.3.2.1 Description

This criterion measures the verticality and depth of the collateral sulcus (CS) relatively to the size of the hippocampus. The CS is the sulcus which separates the fourth temporal (T4) from the fifth (T5) of the temporal lobe, and supports the collateral eminence (see Figure 4.1). Different definitions have been proposed for the start of the CS, some studies consider the rhinal sulcus binding laterally the uncus (Ono et al. (1990), Hanke (1997), Novak et al. (2002), Kim et al. (2008)) and others suppose that the rhinal sulcus is the most anterior part of the uncus (Insausti et al. (1995), Duvernoy (1999)). The problem of the collateral sulcus ending is even more complicated, but they all almost agree with the fact that the ending of the CS is at the level of the posterior part of the hippocampus tail. Some interesting studies which have been led by Novak et al. (2002) in mesial temporal lobe epilepsy (TLE) patients, by Kim et al. (2008) in controls and patients with TLE and by Huntgeburth & Petrides (2012) in healthy subjects, provide a quantification of the localization and variability for the collateral sulcus. In these studies, the collateral sulcus is mainly at the level of the hippocampus body, and sometimes at the levels of

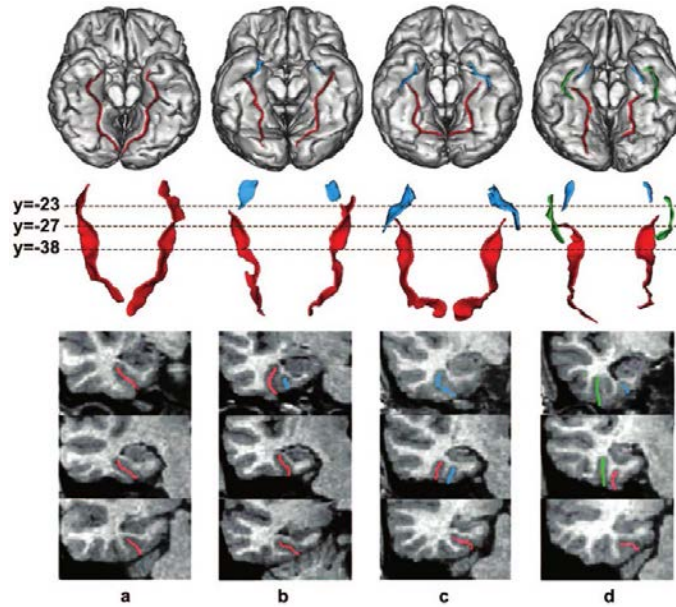


Figure 4.6: Figure from [Kim et al. \(2008\)](#). The red sulcus is the collateral sulcus (CS), the blue one is the rhinal sulcus (RS) and the green one, the occipitotemporal sulcus (OTC). Upper panel: basal view of the 3D MRI rendering. Middle panel: basal view of extracted sulci. Lower panel: three coronal slices of T1-weighted MRI at the level of hippocampal head, body and tail. The columns represent the four different patterns.

the hippocampus head and tail. The study of [Kim et al. \(2008\)](#) (Figure 4.6) shows the different patterns of the collateral sulcus, and we can observe that it is only at the level of the hippocampus body that we are sure to find the collateral sulcus. This criterion has to be observed at the hippocampus body level, in a coronal view, to avoid mistakes.

This criterion is evaluated at the level of the hippocampal body, in order to have an easy identification of the CS. In Figure 4.7, the vertical orange line $C2_b$ indicates the lateral limit of the hippocampus, and the blue segment $C2_a$ indicates the collateral sulcus. The evaluation of this criterion has been defined as follows:

4.3. SIMPLIFIED INDIVIDUAL CRITERIA AND GLOBAL CRITERION FOR IHI ASSESMENT 99

if the blue segment $C2_a$ does not cross the orange line $C2_b$, the grade for $C2$ will be from 0 to 1, i.e. 0, 0.5 or 1. If the line $C2_a$ crosses the segment $C2_b$ the grade will be from 1 to 2 (i.e. 1, 1.5 or 2). In an extreme case, when segment $C2_a$ starts laterally to the segment $C2_b$ (it can happen when the hippocampus has a very medial positioning), the grade is 2. Then the final grade is determined by the verticality, evaluated on 3 levels, of the blue segment $C2_a$, as presented in Table 4.4.

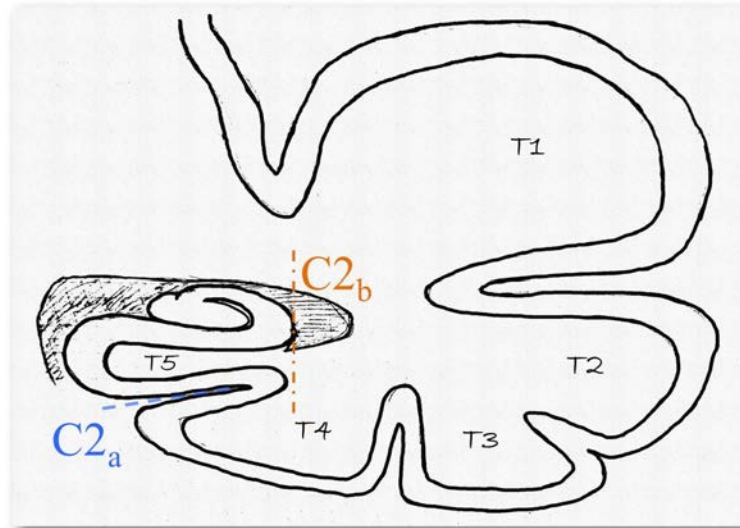


Figure 4.7: criterion $C2$: verticality and depth of the collateral sulcus. The segment a indicates the collateral sulcus, and b the lateral part of the hippocampus. If a do not cross b and stays medial to b , the grade will be between 0 and 1 otherwise between 1 and 2.

Table 4.4: Evaluation of the criterion $C2$. Segments $C2_a$ and $C2_b$ are defined on reference to the figure 4.7 page 99.

Verticality of a grade	$C2_a$ do not cross $C2_b$			$C2_a$ cross $C2_b$		
	Hor	Obl	Ver	Hor	Obl	Ver
	0	0.5	1	1	1.5	2

4.3.2.2 Examples

Some examples of the C_2 criterion are given in Figure 4.8, (a) has a grade of 0 since C_{2_a} is horizontal and does not cross C_{2_b} . (b) has a grade of 0.5 since C_{2_a} is oblique, even if the occipito-temporal sulcus seems closer to the temporal horn. (c) has a grade of 1, C_{2_a} crosses horizontally C_{2_b} . (d) has a grade of 1.5 since C_{2_a} is oblique and cross C_{2_b} . (e) and (f) have a grade of 2, they are vertical, and cross or exceed C_{2_b} .

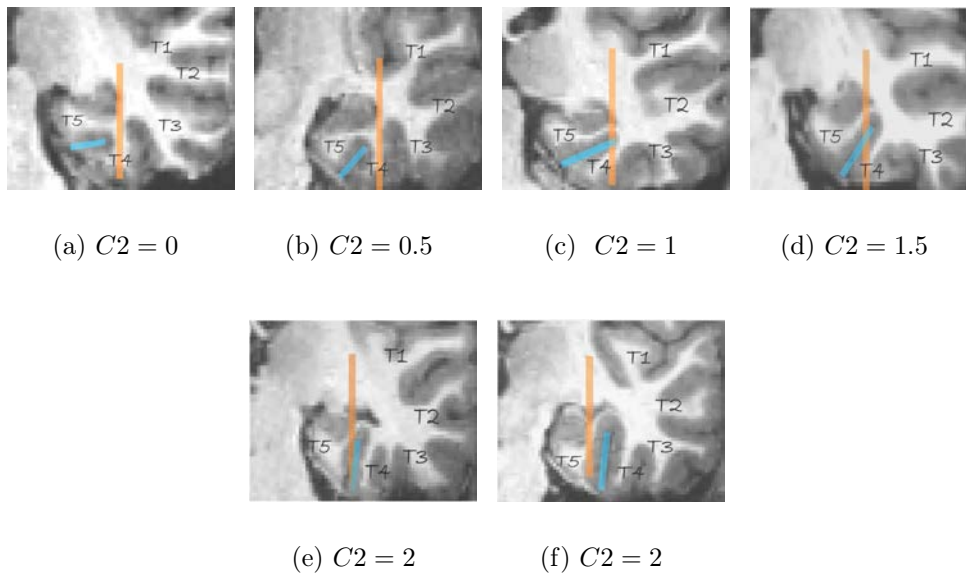


Figure 4.8: Examples for the criterion C_2 . The segments are displayed to help the reader, but during the evaluation no segments appear on the MRI. (a) has a grade of 0 since C_{2_a} is horizontal and does not cross C_{2_b} . (b) has a grade of 0.5 since C_{2_a} is oblique, even if the occipito-temporal sulcus seems closer to the temporal horn. (c) has a grade of 1, C_{2_a} crosses horizontally C_{2_b} . (d) has a grade of 1.5 since C_{2_a} is oblique and cross C_{2_b} . (e) and (f) have a grade of 2, they are vertical, and cross or exceed C_{2_b} .

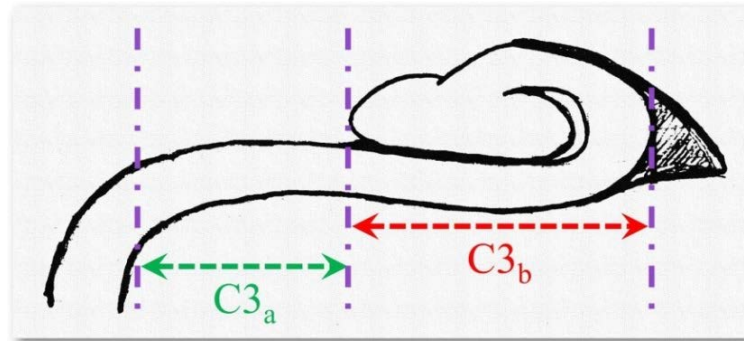


Figure 4.9: Criterion $C3$. Medial positioning of the hippocampus is estimated using the length of the part of the subiculum which is not covered by the gyrus dentatus (segment $C3_a$) relatively to the length of the ventral part of the hippocampus which is covered by the gyrus dentatus (segment $C3_b$).

4.3.3 Criterion $C3$: medial positioning

4.3.3.1 Description

This criterion assesses the medial positioning of the hippocampus. To evaluate this criterion, we consider the length of the part of the subiculum which is not covered by the gyrus dentatus, (segment $C3_a$ on Figure 4.9) relatively to the ventral part of CA1/subiculum which is covered by the gyrus dentatus (segment $C3_b$ on Figure 4.9). Even if the hippocampus is vertical or oblique, segments $C3_b$ and $C3_a$ are defined orthogonally to the brain midline. The junction between $C3_b$ and $C3_a$ is on the same plane as the fimbria. In addition, we considered whether the temporal horn (TH) of the lateral ventricle was empty or filled by the cerebrospinal fluid (CSF).

The evaluation is made on five levels: from 0 for a very lateral positioning to 2 for a very medial one. Evaluations are given in Table 4.5. The two extreme grades are only given using the segment $C3_a$; if the $C3_a$ part is not visible because the

Table 4.5: Evaluation of the Criterion 3. Segments $C3_a$ and $C3_b$ are defined on Figure 4.9.

	$C3_a$ is \emptyset	$C3_a < C3_b$	$C3_a = C3_b$	$C3_a > C3_b$	$C3_a \gg C3_b$
TH emptied	2	1	0.5	0	0
TH filled by CSF	2	1.5	1	0.5	0

hippocampus is too close to the ambient cistern, the grade is 2, regardless of the temporal horn. Similarly, if the subiculum is very long compared to the $C3_b$ part, the grade is 0, regardless of the temporal horn. In other situations, the grade is modulated by the configuration of the temporal horn, as presented in Table 4.5.

4.3.3.2 Examples

Examples are given in Figure 4.10. The image 4.10(b) corresponds to the case where $C3_a = C3_b$ and the temporal horn is filled by the CSF, (a) corresponds to the case where $C3_a > C3_b$ and (c) the case where $c3_a$ is not visible, the hippocampus is too close to the ambient cistern.

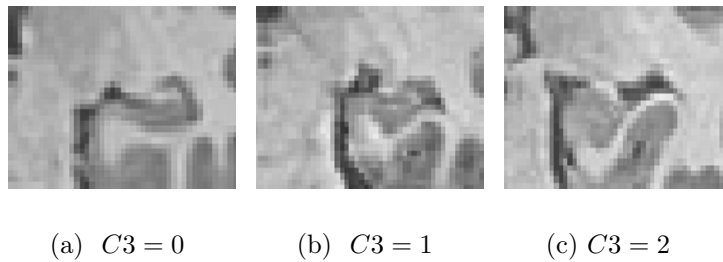
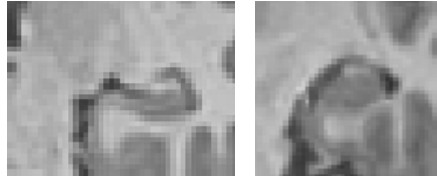


Figure 4.10: Examples for the criterion C_3 . (a) corresponds to the case where $C3_a > C3_b$, (b) corresponds to the case where $C3_a = C3_b$ and the temporal horn is filled by the CSF, (c) the case where $c3_a$ is not visible

4.3.4 Criterion C_4 : subiculum



(a) $C_4 = 0$

(b) $C_4 = 2$



1. HB subiculum thick

(c) Image from [Bernasconi et al. \(2005\)](#). The hippocampus pointed by the arrow have a grade 2, the other a grade 0.

Figure 4.11: Examples for the criterion C_4 .

4.3.4.1 Description

This criterion assesses the thickness of the subiculum, as in [Bernasconi et al. \(2005\)](#). The subiculum is considered as abnormal if it is bulging upward, therefore looking thickened, which corresponds to a grade equal to 2. Otherwise, the subiculum is considered normal and the grade is 0.

4.3.4.2 Examples

Here (Figure 4.11) are some examples of this criterion, two are from the database IMAGEN and the other one from the study of [Bernasconi et al. \(2005\)](#) which corresponds to a grade 2 for our evaluation.

4.3.5 Criterion C5: sulci of the fusiform gyrus (T4)

4.3.5.1 Description

This is a new criterion, which complements criterion C2. Indeed, we observed that IHI are not only associated with atypical patterns of the collateral sulcus but also of the occipito-temporal sulcus (OTS) which separates the fourth temporal (T4) and the third temporal (T3) convolution. In that case, the OTS is deep and comes laterally to the hippocampus. Criterion C5 takes into account both the CS and the OTS. We evaluate if one of these sulci is deep enough to cross the level of the subiculum. In Figure 4.12, we can see that none of the two sulci, which superior parts are indicated by dotted green lines, goes over the subiculum indicated by the red area.

The evaluation is made on three levels. If none of the sulci exceed the level of the subiculum, the grade is 0. If one of the sulci crosses sidewise the red area (with an oblique orientation), the grade is 1, and if a sulcus exceeds vertically, the grade is 2. If the two sulci cross the red area the grade is 2.

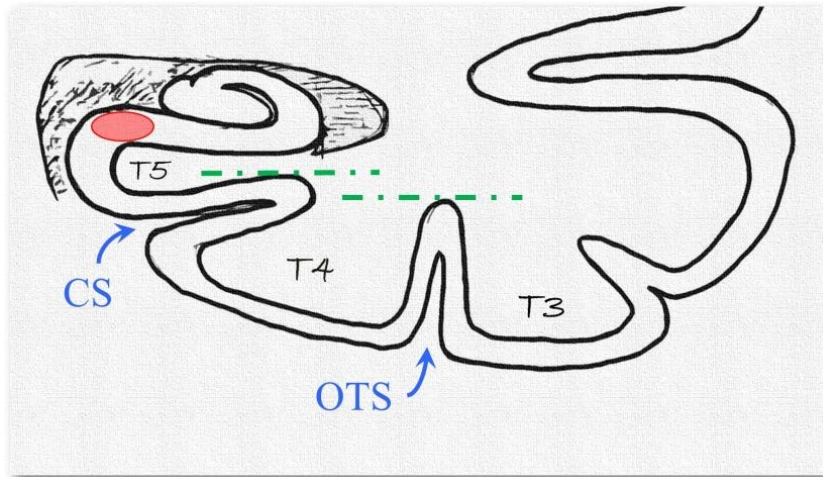


Figure 4.12: Criterion C5. If neither the CS nor the OTS superior parts (green dotted lines) exceed the level of the subiculum (red area), the grade is 0. Otherwise, the grade is either 1 (if the exceeding sulcus has an oblique orientation) or 2 (if the exceeding sulcus has a vertical orientation).

4.3.5.2 Examples

Examples are given in Figure 4.13. The green line represents the top of the deeper sulcus between CS and OTS, and the red area the subiculum as described above. In the subfigure 4.13(c), we can note that the deeper sulcus is the OTS one. For this hippocampus, the criterion C2 is graded 0, the deeper sulcus is not the collateral sulcus which is very small.

4.3.6 Global criterion C0

In addition to these five individual criteria, we also defined a global criterion indicating the presence of an IHI. This was done in order to provide a global assessment of the presence of an IHI. Criterion C0 is evaluated on three levels, a grade of 0 is given if the hippocampus has a common aspect, a grade of 2 is given if the

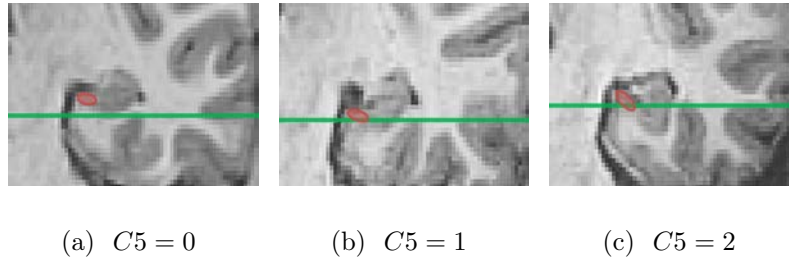


Figure 4.13: Examples for the criterion C_5 .

hippocampus has a pronounced incomplete inversion which corresponds to the total IHI in the literature (Baulac et al., 1998; Bajic et al., 2008), and a 1 is given if the hippocampus does not have a common aspect (flat and horizontal) neither a clear incomplete inversion, which corresponds to a partial IHI (Bajic et al. (2008)).

4.4 Hippocampus segmentation

We segmented the hippocampi using the SACHA software (Chupin et al., 2009). The method has the advantage to include realistic anatomical constraints. We performed quality control of the segmentation results for each hippocampus. Notations of the quality control were grades between 0 and 4, with the following scale:

- 0 when there is no segmentation;
- 1 when the method did not find the hippocampus (bounding box misplaced);
- 1.5 when the segmentation clearly failed;
- 2 when the segmentation is globally acceptable (would result in a reasonable volumetric estimation), but when the shape of the hippocampus is modified;
- 2.5 when the shape of the hippocampus is slightly deformed, mainly because

- a part of the head is missing;
- 3 when the segmentation is good, some small parts of the hippocampus are over segmented or under segmented but without modifying the hippocampal shape;
- 3.5 when some local voxels are missing;
- 4 for a perfect segmentation.

4.5 Experiments

4.5.1 Java application

For the evaluation of the database, we needed a software capable to quickly load MRI, in which we could grade each criterion for each subject, save these notations and reload them. Since we also segmented the hippocampus with the SACHA software [Chupin et al. \(2009\)](#) (see chapter 6), we also wanted to be able to control the quality of the segmentation at the same time.

For this we developed, based on a first version of an application developed by Roberto Toro, an application in Java able to change MRI by using the keyboard arrows and keeping the same view as the previous subject. The application loads 2000 MRI in nifti format at the beginning in about 3-4 minutes.

The window is separated in three panels, the left one contains a table with in columns the subjects IDs, comments, grades of criteria and segmentations QC grades. The middle panel and the right one are the same: these panels propose different small images to choose, by clicking on the small image, the point of view

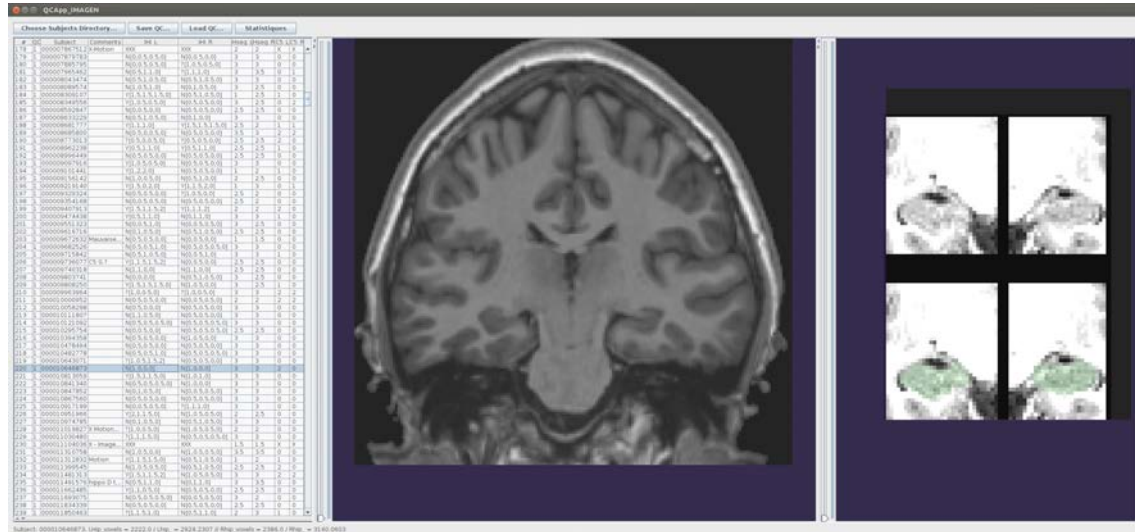


Figure 4.14: Java application for evaluation of IHI, quality control of MRI and quality control of MRI segmentations.

(coronal, sagittal, axial) to visualize the MRI, in its native space or in the MNI space, it is also possible to view bounding boxes of the hippocampus for the segmentation control, with or without the binary mask. There are two panels to display 2 different views at the same time, the Figure 4.14 displays for the same subject its coronal view and on the right panel the corresponding bounding box with the segmentation. It is possible to zoom in or out the image by using the scroll wheel. The user can change subjects by clicking in the table on the left panel on the desired subject, or by using the keyboard arrows. In any cases, the next subject will be directly (waiting time: 1 second) opened at the same slice of the same point of view, to facilitate the notation of the whole database.

At any moment grades can be saved in a text file, so it is easy to import them in a excel document for example. At the beginning of a session it is also possible to

load grades from a previous session.

4.5.2 IHI assesment

IHI were assessed by two observers (Claire Cury (CC) and Fanny Cohen (FC)). 42 subjects were randomly selected to evaluate the intra- and inter-observer reproducibility of the evaluations. Half of the remaining 1966 subjects were evaluated by CC, the other half was evaluated by FC. Additionally CC checked the evaluations given by FC, and FC checked the evaluations given by CC in order to homogenize evaluations.

4.5.3 Intra- and inter-observer reproducibility

To evaluate the reproducibility, each observer had to evaluate twice the same series of 42 subjects. This evaluation was done independently by the two observers and the grades were not subsequently homogenized. The first time is after the evaluation of at least 200 subjects, and the second time after assessing 900 MRI, with at least 3 weeks between reproducibility tests. The intra and inter reproducibility was computed using a kappa test for the criteria $C0$ and $C5$ (which are categorical variables) and a weighted kappa test for criteria $C1$, $C2$ and $C3$. Reproducibility of criterion $C4$ could not be evaluated because all 42 subjects used for reproducibility assessment had a $C4$ grade equal to zero

4.5.4 Statistical analysis

Based on the global criterion, we computed the proportions of IHI along with confidence intervals at 95%. We compared the proportion of IHI between left and right hemispheres using chi-square test. . We also compared the proportions of IHI between males and females and between left-handed and right-handed subjects using chi-square tests. For all individual criteria $C1$ to $C5$, we computed the frequencies of the different possible grades (from 0 to 2), as well as the average grades. Results between left and right hippocampi were compared using chi-square tests. Finally, we studied the relationship between the sum of individual criteria (SC) and the global criterion $C0$ and estimated an optimal threshold on SC to classify IHI, using $C0$ as a reference.

4.6 Results

4.6.1 Intra- and inter-observer reproducibility

Results of kappa test, for the intra- and inter- observer reproducibility are given in Table 4.6. A kappa value over 0.6 indicates a substantial agreement, and over 0.8 a very strong agreement (Cunningham, 2009). In all cases, intra- and inter-observer agreements were beyond substantial (0.6). Very strong agreements (over 0.8) were observed in the majority of cases.

Table 4.6: Results of Kappa test for the intra- and inter-observers reproducibility of the different criteria. The confident interval is at 95%

	<i>C0</i>	<i>C1</i>	<i>C2</i>	<i>C3</i>	<i>C5</i>
CC1 vs CC2	0.80 <i>CI</i> : [0.66; 0.95]	0.74 <i>CI</i> : [0.63; 0.86]	0.78 <i>CI</i> : [0.68; 0.89]	0.81 <i>CI</i> : [0.71; 0.90]	0.73 <i>CI</i> : [0.58; 0.88]
FC1 vs FC2	0.89 <i>CI</i> : [0.78; 0.99]	0.71 <i>CI</i> : [0.59; 0.83]	0.82 <i>CI</i> : [0.70; 0.93]	0.87 <i>CI</i> : [0.76; 0.92]	0.87 <i>CI</i> : [0.76; 0.98]
CC1 vs FC1	0.79 <i>CI</i> : [0.63; 0.94]	0.64 <i>CI</i> : [0.52; 0.76]	0.81 <i>CI</i> : [0.72; 0.91]	0.86 <i>CI</i> : [0.78; 0.94]	0.86 <i>CI</i> : [0.75; 0.97]
CC2 vs FC2	0.87 <i>CI</i> : [0.75; 0.99]	0.82 <i>CI</i> : [0.72; 0.92]	0.88 <i>CI</i> : [0.81; 0.96]	0.87 <i>CI</i> : [0.80; 0.95]	0.80 <i>CI</i> : [0.66; 0.94]

Table 4.7: Percentage of IHI for left and right hippocampi with a confidence interval of 95%

<i>C0</i>	No IHI	Partial IHI	IHI
Left	70.9% <i>CI</i> : [68.9%; 72.9%]	11.9% <i>CI</i> : [10.5%; 13.3%]	17.1% <i>CI</i> : [15.5%; 18.7%]
Right	84.6% <i>CI</i> : [83.0%; 86.2%]	9.0% <i>CI</i> : [7.7%; 10.3%]	6.5% <i>CI</i> : [5.4%; 7.6%]

4.6.2 Global criterion *C0*

Table 4.7 presents the prevalence of IHI according to the global criterion *C0*. Total IHI was found in 17% of healthy subjects for the left hippocampus and 6% for the right. IHI were significantly more frequent for the left hippocampus compared to the right ($\chi^2 = 129.2$ DF = 2 $p = 8.5e-29$).

Table 4.8 displays the co-occurrences of left and right IHI. One can note that the majority of right IHI are in fact bilateral IHI, unilateral right IHI having low frequency. On the other hand, unilateral left IHI are common. Further, left and right *C0* grades are not independent ($\chi^2 = 384.1$ DF = 4 $p = 7.5e-82$).

The frequencies of IHI in males and females are displayed on Table 4.9. The

Table 4.8: Co-occurrences of IHI for the left and right hippocampi, according to the global criterion $C0$. Confidence intervals (CI) are at 95%.

Left \ Right	No IHI	Partial IHI	IHI
No IHI	65.9% <i>CI</i> : [63.8%; 68.0%]	3.1% <i>CI</i> : [2.3%; 3.9%]	1.9% <i>CI</i> : [1.3%; 2.5%]
Partial IHI	7.9% <i>CI</i> : [6.7%; 9.1%]	3.5% <i>CI</i> : [2.7%; 4.3%]	0.5% <i>CI</i> : [0.2%; 0.8%]
IHI	10.8% <i>CI</i> : [9.4%; 12.2%]	2.3% <i>CI</i> : [1.6%; 3.0%]	4.0% <i>CI</i> : [3.1%; 4.9%]

frequencies did not differ between males and females ($\chi^2 = 4.41$ DF = 2 $p = 0.11$ for left hippocampi and $\chi^2 = 1.29$ DF = 2 $p = 0.52$ for right hippocampi). Therefore the differences between male and female seem to be due to the sample fluctuation.

Table 4.9: Frequency of IHI, according to the global criterion $C0$, for female and male populations, with a confidence interval at 95%

$C0$ Left	No IHI	Partial IHI	IHI
Female (n=1029)	70.1% <i>CI</i> : [67.3%; 72.9%]	13.4% <i>CI</i> : [11.3%; 15.5%]	16.5% <i>CI</i> : [14.2%; 18.8%]
Male (n=978)	71.8% <i>CI</i> : [69.0%; 74.6%]	10.4% <i>CI</i> : [8.5%; 12.3%]	17.8% <i>CI</i> : [15.4%; 20.2%]
$C0$ right	No IHI	Partial IHI	IHI
Female (n=1029)	84.4% <i>CI</i> : [82.2%; 86.6%]	9.5% <i>CI</i> : [7.7%; 11.3%]	6.1% <i>CI</i> : [4.6%; 7.6%]
Male (n=978)	84.9% <i>CI</i> : [82.7%; 87.1%]	8.3% <i>CI</i> : [6.6%; 10.0%]	6.9% <i>CI</i> : [5.3%; 8.5%]

The frequencies also did not differ depending on handedness ($\chi^2 = 2.29$ with $p = 0.89$ for left; $\chi^2 = 5.07$ with $p = 0.54$ for right). We cannot refute that the proportions between handedness right left and both-handed are identical according to the criterion $C0$.

Table 4.10: Repartition of grades for each individual criterion. We tested whether the repartition differs between left and right for each criterion (chi-square test).

	Left hippocampi					Right hippocampi				
	0	0.5	1	1.5	2	0	0.5	1	1.5	2
C1	23%	44%	23%	8%	1%	20%	58%	18%	3%	0%
C2	18%	42%	28%	11%	1%	9%	57%	29%	4%	0%
C3	27%	40%	21%	10%	2%	38%	39%	17%	5%	1%
C4	97%	NA	NA	NA	3%	98%	NA	NA	NA	2%
C5	59%	NA	20%	NA	20%	85%	NA	6%	NA	9%

Table 4.11: For each individual criterion, its mean value on left and right and its frequency when ≥ 1

	Left hippocampi		Right hippocampi	
	Mean value	Frequency of abnormal criterion (≥ 1)	Mean value	Frequency of abnormal criterion (≥ 1)
C1	0.61 <i>CI</i> : [0.59; 0.63]	33% <i>CI</i> : 31% – 35%	0.52 <i>CI</i> : [0.51; 0.54]	21% <i>CI</i> : 19% – 23%
C2	0.68 <i>CI</i> : [0.66; 0.70]	40% <i>CI</i> : 38% – 42%	0.64 <i>CI</i> : [0.62; 0.66]	33% <i>CI</i> : 31% – 35%
C3	0.60 <i>CI</i> : [0.58; 0.62]	33% <i>CI</i> : 31% – 35%	0.45 <i>CI</i> : [0.43; 0.47]	23% <i>CI</i> : 21% – 25%
C4	0.07 <i>CI</i> : [0.05; 0.09]	3% <i>CI</i> : 2% – 4%	0.03 <i>CI</i> : [0.02; 0.04]	2% <i>CI</i> : 1% – 3%
C5	0.61 <i>CI</i> : [0.57; 0.65]	41% <i>CI</i> : 39% – 43%	0.24 <i>CI</i> : [0.21; 0.26]	15% <i>CI</i> : 13% – 17%

4.6.3 Individual criteria

The repartition of grades of each individual criterion (*C1* to *C5*) is given in Table 4.10. For all criteria, the repartition was statistically different between left and right.

To complete in the Table 4.10, we present the average grade for each criterion as well as the proportion of subjects having a grade superior or equal to 1.

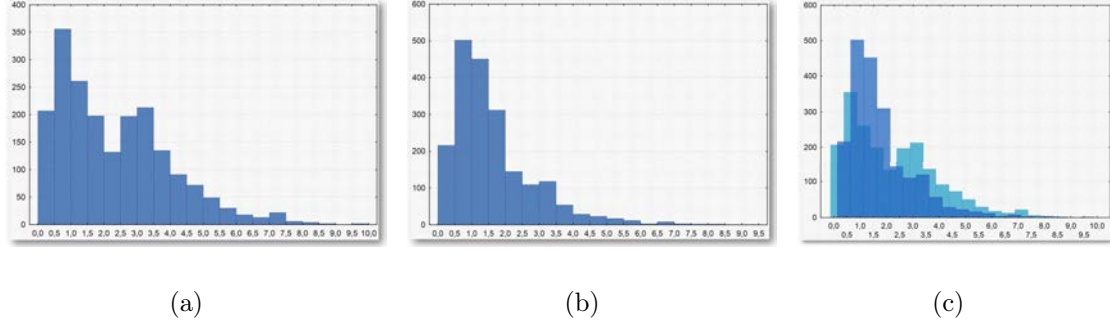


Figure 4.15: Histograms of the sums of individual criteria C_i for left hippocampi (a), right hippocampi (b) and the superposed histograms (c).

The sum of grades for all individual criteria ($C1$ to $C5$) may provide an overall degree of IHI. We denote this sum as IHI score. Figure 4.15 shows the histograms of the sum of grades for individual criteria for left and right hippocampi. Figure 4.16 shows the repartition of IHI score with respect to the grade of the global criterion $C0$. We can note that the populations with (IHI) and without IHI (NoIHI) are well separated. On the other hand, the intermediate class of “Partial IHI” overlaps with the two others. This highlights the consistency between the global criterion $C0$ and the individual criteria $C1$ to $C5$.

Furthermore, we computed the optimal threshold grade on IHI score to classify a given hippocampus into IHI or not, using the global criterion $C0$ as a reference. To compute this threshold, we used only hippocampi with a $C0$ grade of 0 (absence of IHI) or 2 (presence of IHI). We then computed the threshold on IHI score which maximizes the accuracy of the classification between cases with and without IHI. The optimal threshold is 3.75, i.e. hippocampi without IHI correspond to IHI score < 4 , and hippocampi with IHI correspond to IHI score ≥ 4 . Table 4.12 reports

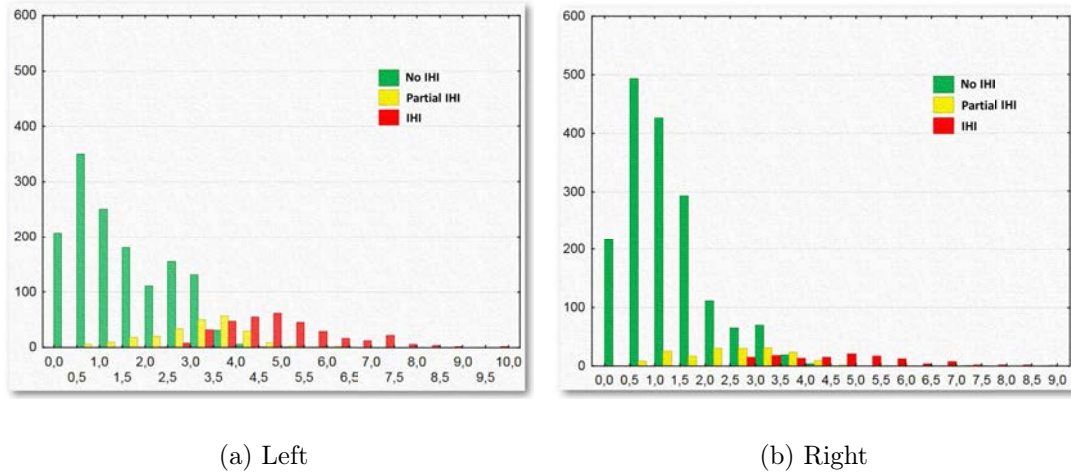


Figure 4.16: Histogram of the sum of grades of all individual criteria ($C1$ to $C5$) for left hippocampi (a), right hippocampi (b) and the superposed histograms (c).

Table 4.12: Frequency of IHI using the threshold IHI score < 4

	Left hippocampi		Right hippocampi	
	Classifying IHI and No IHI	Classifying all hippocampi	Classifying IHI and No IHI	Classifying all hippocampi
IHI	17%	22%	6%	8%
No IHI	71%	78%	85%	92%

the frequencies of IHI using this threshold. The Table indicates both frequencies obtained without taking into account the hippocampi with $C0 = 1$ (which are thus very close to those reported in Table 6) and frequencies obtained when classifying all hippocampi.

4.6.4 Impact of IHI on the automatic segmentation

We observed that results of segmentation were better for normal hippocampi than for IHI. On the left, the average quality control of segmentations was 2.06 for

hippocampi with IHI ($C_0 = 2$), 2.46 for hippocampi with $C_0 = 1$ and 2.74 for normal hippocampi ($C_0 = 0$). On the right, the average quality control of segmentations was 2.38 for hippocampi with IHI ($C_0 = 2$), 2.65 for hippocampi with $C_0 = 1$ and 2.69 for normal hippocampi ($C_0 = 0$). Thus, the segmentation quality decreased with the level of IHI. For the left side (which contains more IHI), we observed a correlation between the IHI score and the quality control of the segmentations ($r = -0.39$). These results clearly indicate that IHI have a bad influence on the segmentation method.

Since QC results were lower in subjects with IHI, it is not possible to use the whole population for subsequent volumetric or shape analysis. In the following, we consider as good segmentations the segmentations with a quality control ≥ 3 . This amount to 1114 segmentations for the left side, and 1085 segmentations for the right side. Using the C_0 criterion, left hippocampal volumes (of segmentations whose quality control were ≥ 3) for $C_0 = 0$ are on average 2.95 cm^3 for 891 subjects (and 2.99 cm^3 for the right side of 930 subjects). For hippocampus with IHI, so with $C_0 = 2$, left hippocampal volumes are on average 2.75 cm^3 for 113 subjects (and 2.78 cm^3 for the right side of 58 subjects). The difference in volume between hippocampi with IHI and hippocampi with a normal development was statistically significant (t -stat = 5.93, $df=1009$, $p = 4.11e-9$). The correlation between the criterion C_0 and the volume of segmentations with a quality control ≥ 3 are -0.24 for left hippocampi and -0.21 for right hippocampi. Thus, when considering only segmentation with good quality, the volume of the hippocampus is lower in subjects with IHI.

4.7 Discussion and conclusion

In this chapter, we characterized incomplete hippocampal inversions and studied their prevalence in a large population of young healthy subjects. We demonstrated that IHI are a common anatomical pattern in healthy subjects and that they are much more frequent in the left hemisphere. Our results clearly demonstrate that IHI are a common phenomenon in the healthy population, with a frequency of about 17% in the left hemisphere and about 6% in the right hemisphere. The existence of IHI in normal subjects was already known (Bajic et al., 2009; Gamss et al., 2009; Bernasconi et al., 2005) but their prevalence was a matter of debate, some authors arguing that IHI are a rare finding in patients without epilepsy (Gamss et al., 2009) and others reporting that IHI are a common anomaly (Bajic et al., 2009; Raininko & Bajic, 2010). The discrepancies between previous studies can be due to: 1) relatively small number of subjects resulting in imprecise estimates of the frequency; 2) populations that mixed normal controls and patients without epilepsy but with other conditions; 3) different sets of criteria for assessing IHI. Our study relied on a large population of normal subjects, providing reliable estimates with small confidence intervals. Furthermore, we included only young healthy subjects thus avoiding the occurrence of medical conditions that could bias the estimates or of age-related morphological changes that could make the visual evaluation difficult. Incomplete inversions were clearly more frequent in the left than in the right hemisphere. Furthermore, unilateral right IHI were rare while bilateral IHI were more common. This finding is consistent with previous studies (Bajic et al., 2009). The origin of this asymmetry is unknown. One can speculate that left and right hippocampi may not

develop exactly at the same pace and thus that when the inversion is stopped it may be incomplete only in the left hemisphere.

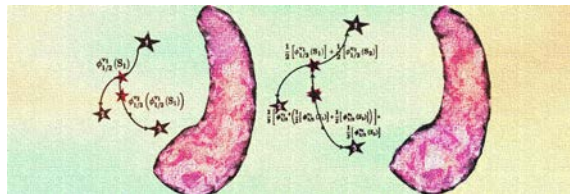
In our study, IHI were equally common in males and females. This is consistent with the findings of [Bajic et al. \(2008\)](#). Furthermore, IHI were not related to handedness of the subjects. For this study, we adapted criteria of IHI which are most commonly found in the literature to define a set of criteria which includes a reasonable number of criteria that can be applied on large datasets. As demonstrated by the reproducibility study, our criteria are highly reproducible across observers and rating sessions. We also defined a global criterion assessing the overall presence of an IHI. Although this criterion could theoretically be more subjective, we showed that its reproducibility is as good as for the other criteria. Furthermore, the global criterion was highly consistent with the individual scores. The distribution of the sum of individual criteria indicates there is a continuum between a normal hippocampus and IHI, with various intermediate degrees of hippocampal inversions. We nevertheless proposed a threshold on the sum of criteria that allows classifying an individual as presenting an IHI or not, that is consistent with the visual global assessment. Nevertheless, one should note that we do not claim that the global criterion is a gold standard, using the detailed criteria presented above could lead to more comparable results across studies. Compared to the other criteria, there were much less subjects with an abnormal score for criterion *C4* (about 3% of subjects), corresponding to a thicker subiculum. Interestingly, in [Bernasconi et al. \(2005\)](#), none of the 50 healthy subjects had an abnormally thick subiculum. This suggests that this criterion might be specific to malformations of cortical development or tempo-

ral lobe epilepsy. Nevertheless, this hypothesis would need to be tested in further work. Automatic segmentation performed less well in subjects with IHI than in subjects without, as demonstrated by the QC grades of segmentations which were significantly lower in subjects with IHI. This is consistent with the findings reported in [Kim et al. \(2012\)](#) which reported lower segmentation quality in subjects with IHI for various segmentation methods. This precludes the possibility to compare hippocampal segmentations (either with volumetry or shape analysis) between subjects with and without IHI on the whole population. Nevertheless, we still have over 1000 subjects (including over 100 subjects with IHI) with a QC score superior or equal to 3. Volumetry and shape analysis can thus be performed within this subpopulation. In this subpopulation, we found that subjects with IHI had a significantly smaller hippocampus than subjects with a normal hippocampus.

We studied the prevalence and characteristics of IHI in a large population of healthy subjects. We were able to conclude that IHI are a frequent phenomenon in healthy subjects and are more common in the left hemisphere than in the right. Using a large dataset, we were able to obtain narrow confidence intervals reflecting precise estimates of the prevalence. We also demonstrated that IHI do not depend on sex nor on handedness. We further showed there is a continuum of changes from a normal hippocampus to a complete IHI. For this study, we designed a new set of criteria for IHI, by adapting existing criteria proposed in the literature. Our criteria are applicable to large datasets and would allow further comparison between studies. We also showed that IHI have an impact on the quality of automatic hippocampal segmentation. This precludes a comparisons of hippocampal segmentations on the

whole population. However, a substantial portion of the population (over 1000 subjects) had very good segmentation quality; This subpopulation will be used subsequently for statistical shape analysis.

CHAPTER 5



DIFFEOMORPHIC ITERATIVE CENTROID METHOD FOR TEMPLATE ESTIMATION ON LARGE DATASETS

This part is directly taken from the chapter of the same name, published in 2014 in the book *Geometric Theory of Information* (Cury et al., 2014b). It introduces the Diffeomorphic Iterative Centroid method, which intended to be used primarily in our experiments as a fast and robust initialization algorithm for the template estimation method presented in section 3.5.

We will see in chapter 6 that this centroid algorithm can in fact be used itself as an alternative for template estimation for the statistical analysis of large datasets.

5.1 Introduction

Large imaging datasets are being increasingly used in neuroscience, thanks to the wider availability of neuroimaging facilities, the development of computing infrastructures and the emergence of large-scale multi-center studies. Such large-scale datasets offer increased statistical power which is crucial for addressing questions such as the relationship between anatomy and genetics or the discovery of new biomarkers using machine learning techniques for instance.

Computational anatomy aims at developing tools for the quantitative analysis of variability of anatomical structures, its variation in healthy and pathological cases and relations between functions and structures ([Grenander & Miller, 1998](#)). A common approach in computational anatomy is template-based analysis, where the idea is to compare anatomical objects by analyzing their variations relatively to a common template. These variations are analyzed using the ambient space deformations that match each individual structure to the template.

As exposed in the chapter 3, a common requirement is that transformations must be diffeomorphic in order to preserve the topology and to consistently transform coordinates. The Large Deformation Diffeomorphic Metric Mapping framework ([Christensen et al., 1996](#); [Beg et al., 2005](#)) has been widely used for the study of the geometric variation of human anatomy, of intra-population variability and inter-population differences. A presentation of the LDDMM are presented in section 3.3.2 page 67. It focuses the study on the spatial transformations which can match subject's anatomies one to another, or one to a template structure which needs to be estimated. These transformations not only provide a diffeomorphic correspondence

between shapes, but also define a metric distance in shape space.

In Chapter 3 we saw that several methods have been proposed to estimate templates in the LDDMM framework [Vaillant et al. \(2004\)](#); [Glaunès & Joshi \(2006\)](#); [Durrleman et al. \(2008a, 2012\)](#); [Ma et al. \(2008\)](#). [Vaillant et al. \(2004\)](#) proposed a method based on geodesic shooting which iteratively updates a shape by shooting towards the mean of directions of deformations from this shape to all shapes of the population. The method proposed by [Glaunès and Joshi \(2006\)](#) starts from the whole population and estimates a template by co-registering all subjects. The method uses a backward scheme: deformations are defined from the subjects to the template. The method optimizes at the same time the deformations between subjects and the template, and the template itself. The template is composed, in the space of currents (more details on section 3.3.1 page 62), by all surfaces of the population. A different approach was proposed by [Durrleman et al. \(2008a, 2012\)](#). The method initializes the template with a standard shape, in practice it is often an ellipsoid. The method uses a forward scheme: deformations are defined from the template to the subjects. Again, it optimizes at the same time the deformations and the template. The template is composed by one surface which presents the same configuration as the initial ellipsoid. The method presented by [Ma et al. \(2008\)](#) introduces an hyper template which is an extra fixed shape (which can be a subject of the population). The method aims at optimizing at the same time deformations from the hyper template to the template and deformations from the template to subjects of the population. The template is optimized via the deformation of the hyper template, not directly. A common point of all these methods

is that they need a surface matching algorithm, which is very expensive in terms of computation time in the LDDMM framework. When no specific optimization is used, computing only one matching between two surfaces, each composed of 3000 vertices, takes approximately 30 to 40 minutes. Then, computing a template composed of one hundred such surfaces until convergence can take a few days or some weeks. This is a limitation for the study of large databases. Different strategies can be used to reduce computation time. GPU implementation can substantially speed up the computation of convolutions that are heavily used in LDDMM deformations. Matching pursuit on current can also be used to reduce the computation time [Durrleman et al. \(2009\)](#). Sparse representations of deformations allow to reduce the number of optimized parameters of the deformations [Durrleman et al. \(2012\)](#).

Here, we propose a new approach to reduce the computation time, called diffeomorphic iterative centroid using currents. The method provides in $N-1$ steps (with N the number of shapes of the population) a centroid already correctly centered within the population of shapes. It increases the convergence speed of the template estimation by providing an initialization that is closer to the target.

Our method has some close connections with more general iterative methods to compute means on Riemannian manifolds (i.e. a differential manifold equipped in each tangent space with an inner product that varies smoothly from point to point). For example [Arnaudon et al. \(2012\)](#) defined a stochastic iterative method which converges to the Fréchet mean of the set of points. Ando, Li and Mathias [Ando et al. \(2004\)](#) gave a recursive definition of the mean of positive definite matrices which verifies important properties of geometric means. However these methods

require a large number of iterations (much larger than the number of points of the dataset), while in our case, due to the high computational cost of matchings, we aim at limiting as much as possible the number of iterations.

5.2 An Iterative Centroid method

As presented in the introduction, computing a template in the LDDMM framework can be highly time consuming, taking a few days or some weeks for large real-world databases. To increase the speed of the method, one of the key points may be to start with a good initial template, already correctly centred among shapes in the population. Of course the computation time of such an initialization method must be substantially lower than the template estimation itself. The Iterative Centroid method presented here performs such an initialization with $N - 1$ pairwise matchings only.

The LDDMM framework, in an ideal setting (exact matching between shapes), sets the template estimation problem as the computation of a centroid on a Riemannian manifold, which is of finite dimension in the discrete case (we limit our analysis to this finite dimensional setting in what follows). The Fréchet mean is the standard way for defining such a centroid and provides the basic inspiration of all LDDMM template estimation methods. Since our Iterated Centroid method is also inspired by considerations about computation of centroids in Euclidean space and their analogues on Riemannian manifolds, we will briefly discuss these ideas in the following.

5.2.1 Mathematical justification

If $x_i, 1 \leq i \leq N$ are points in \mathbb{R}^d , then their centroid is defined as

$$b_N = \frac{1}{N} \sum_{i=1}^N x_i. \quad (5.1)$$

It satisfies also the following:

$$b_N = \arg \min_{y \in \mathbb{R}^d} \sum_{1 \leq i \leq N} \|y - x_i\|^2. \quad (5.2)$$

Now, when considering points x_i living on a Riemannian manifold M (we assume M is path-connected and geodesically complete), the definition of b_N cannot be used because M is not a vector space. However the variational characterization of b_N has an analogue, which leads to the definition of the Fréchet mean, also called 2-mean, which is uniquely defined under some constraints (see [Arnaudon et al. \(2012\)](#)) on the relative locations of points x_i in the manifold:

$$b_N = \arg \min_{y \in M} \sum_{1 \leq i \leq N} d_M(y, x_i)^2. \quad (5.3)$$

Many mathematical studies (as for example [Kendall \(1990\)](#), [Karcher \(1977\)](#), [Le \(2004\)](#), [Afsari \(2011\)](#); [Afsari et al. \(2013\)](#)), have focused on proving the existence and uniqueness of the mean, as well as proposing algorithms to compute it. The more general notion of p -mean of a probability measure μ on a Riemannian manifold M is defined by:

$$b = \arg \min_{x \in M} F_p(x), \quad F_p(x) = \int_M d_M(x, y)^p \mu(dy). \quad (5.4)$$

[Arnaudon et al. \(2012\)](#) published in 2012 for $p \geq 1$ a stochastic algorithm which converges almost surely to the p -mean of the probability measure μ . This algorithm

does not require to compute the gradient of the functional F_p to minimize. The authors construct a time inhomogeneous Markov chain by choosing at each step a random point P with distribution μ and moving the current point X to a new position along the geodesic connecting X to P . As it will be obvious in the following, our method shares similarities with this method for the case $p = 2$, in that it also uses an iterative process which at each step moves the current position to a new position along a geodesic. However our method is not stochastic and does not compute the 2-mean of the points. Moreover, our approach stops after $N - 1$ iterations, while on the contrary the stochastic method does not ensure to have considered all subjects of the population after N iterations.

Other definitions of centroids in the Riemannian setting can be proposed. The following ideas are more directly connected to our method. Going back to the Euclidean case, one can observe that b_N satisfies the following iterative relation:

$$\begin{cases} b_1 = x_1 \\ b_{k+1} = \frac{k}{k+1}b_k + \frac{1}{k+1}x_{k+1}, \quad 1 \leq k \leq N - 1, \end{cases} \quad (5.5)$$

which has the side benefit that at each step b_k is the centroid of the $x_i, 1 \leq i \leq k$. This iterative process has an analogue in the Riemannian case, because one can interpret the convex combination $\frac{k}{k+1}b_k + \frac{1}{k+1}x_{k+1}$ as the point located along the geodesic linking b_k to x_{k+1} , at a distance equal to $\frac{1}{k+1}$ of the total length of the geodesic, which we can write $geod(b_k, x_{k+1}, \frac{1}{k+1})$. This leads to the following definition in the Riemannian case:

$$\begin{cases} \tilde{b}_1 = x_1 \\ \tilde{b}_{k+1} = geod(\tilde{b}_k, x_{k+1}, \frac{1}{k+1}), \quad 1 \leq k \leq N - 1, \end{cases} \quad (5.6)$$

Of course this new definition of centroid does not coincide with the Fréchet mean when the metric is not Euclidean, and furthermore it has the drawback to depend on the ordering of points x_i . Moreover one may consider other iterative procedures such as computing midpoints between arbitrary pairs of points x_i , and then midpoints of the midpoints, etc. In other words, all procedures that are based on decomposing the Euclidean equality $b_N = \frac{1}{N} \sum_{i=1}^N x_i$ as a sequence of pairwise convex combinations lead to possible alternative definitions of centroid in a Riemannian setting. Based on these remarks, Emery and Mokobodzki [Emery & Mokobodzki \(1991\)](#) proposed to define the centroid not as a unique point but as the set B_N of points $x \in M$ satisfying

$$f(x) \leq \frac{1}{N} \sum_{i=1}^N f(x_i), \quad (5.7)$$

for any convex function f on M (a convex function f on M being defined by the property that its restriction to all geodesics is convex). This set B_N takes into account all centroids obtained by bringing together points x_i by all possible means, i.e. recursively by pairs, or by iteratively adding a new point, as explained above (see Fig.5.2).

5.2.2 Diffeomorphic Centroid methods

Outline of the method The Iterated Centroid method consists roughly in applying the following procedure: given a collection of N shapes S_i , we successively update the centroid by matching it to the next shape and moving along the geodesic flow. Figure 5.1 illustrates the general idea. We propose two alternative ways for

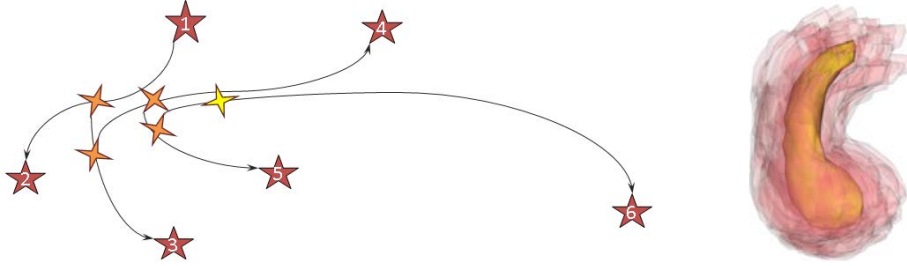


Figure 5.1: Illustration of the method. Left image: red stars are subjects of the population, the yellow star is the final Centroid, and orange stars are iterations of the Centroid. Right image: Final Centroid with the hippocampus population from Data1 (red). See section 5.3.1 for more details about datasets.

the update step (algorithms 1 and 2 below).

5.2.2.1 Direct iterative centroid

The first version of the method computes a centroid between two objects O_1 and O_2 by transporting a first object O_1 along the geodesic going from this object to O_2 . The transport is stopped depending of the weights of the objects. If the weight of O_1 is w_1 , and the weight of O_2 is w_2 with $w_1 + w_2 = 1$, we stop the deformation of O_1 at time $t = w_2$. Since the method is iterative, the first two objects are two subjects of the population, for the next step we have as a first object the previous centroid and as a second object a new subject of the population. The algorithm proceeds as presented in the Algorithm 1.

Data: N surfaces S_i
Result: 1 surface B_N representing the centroid of the population
 $B_1 = S_1$;
for i from 1 to $N - 1$ **do**
 B_i is matched using the equation (3.8) to S_{i+1} which results in a deformation map $\phi_{v_i}(x, t)$;
 Set $B_{i+1} = \phi_{v_i}(B_i, \frac{1}{i+1})$ which means we transport B_i along the geodesic and stop at time $t = \frac{1}{i+1}$;
end

Algorithm 1: Iterative Centroid 1 (IC1)

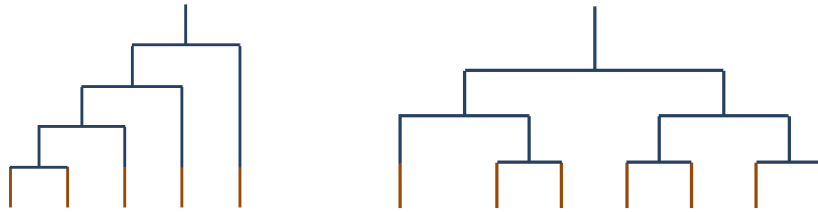


Figure 5.2: Diagrams of the iterative processes which lead to the centroid computation. The tops of the diagrams represent the final centroid. The diagram on the left corresponds to the Iterative Centroid algorithms (IC1 and IC2). The diagram on the right corresponds to the pairwise algorithm (PW).

5.2.2.2 Centroid with averaging in the space of current

Because matchings are inaccurate, the centroid computed with the method presented above accumulates small errors which can have an impact on the final centroid. Furthermore, the centroid computed with algorithm 1 is in fact a deformation of the first shape S_1 , which makes the procedure even more dependent on the ordering of subjects than it would be in an ideal exact matching setting. In this second algorithm, we modify the updating step by computing a mean in the space of currents between the deformation of the current centroid and the backward flow of the current shape being matched. Hence the computed centroid is not a true surface but

a current, i.e. combination of surfaces, as in the template estimation method. The weights chosen in the averaging reflects the relative importance of the new shape, so that at the end of the procedure, all shapes forming the centroid have equal weight $\frac{1}{N}$. The algorithm proceeds as presented in Algorithm 2.

Data: N surfaces S_i

Result: 1 current \mathcal{B}_N representing the centroid of the population

$\mathcal{B}_1 = [S_1]$;

for i from 1 to $N - 1$ **do**

\mathcal{B}_i is matched using the equation (3.8) to S_{i+1} which results in a deformation map $\phi_{v_i}(x, t)$;

Set $\mathcal{B}_{i+1} = \frac{i}{i+1} * \phi_{v_i}(\mathcal{B}_i, \frac{1}{i+1}) + \frac{1}{i+1}[\phi_{u_i}(S_{i+1}, \frac{i}{i+1})]$ which means we transport \mathcal{B}_i along the geodesic and stop at time $t = \frac{1}{i+1}$;

where $u_i(x, t) = -v_i(x, 1 - t)$, i.e. ϕ_{u_i} is the reverse flow map.

end

Algorithm 2: Iterative Centroid 2 (IC2)

Note that we have used the notation $\phi_{v_i}(\mathcal{B}_i, \frac{1}{i+1})$ to denote the transport (push-forward) of the current \mathcal{B}_i by the diffeomorphism. Here \mathcal{B}_i is a linear combination of currents associated to surfaces, and the transported current is the linear combination (keeping the weights unchanged) of the currents associated to the transported surfaces.

5.2.2.3 A pairwise centroid

Another possibility is to group objects by pairs, compute centroids (middle points) for each pair, and then recursively apply the same procedure to the set of centroids, until having only one centroid (see Fig. 5.2). This pairwise method also depends on the ordering of subjects, and also provides a centroid which satisfies

the definition of Emery and Mokobodzki (disregarding the inaccuracy of matchings). When the population is composed of more than 3 subjects, we split the population in two parts and recursively apply the same splitting until having two or three objects in each group. We then apply algorithm 1 to obtain the corresponding centroid before going back up along the dyadic tree, and keeping attention to the weight of each object. This recursive algorithm is described in algorithm 3.

Data: N surfaces S_i
Result: 1 surface B representing the centroid of the population
if $N \geq 2$ **then**
 $B_{left} = \text{Pairwise Centroid}(S_1, \dots, S_{\lfloor N/2 \rfloor});$
 $B_{right} = \text{Pairwise Centroid}(S_{\lfloor N/2 \rfloor + 1}, \dots, S_N);$
 B_{left} is matched to B_{right} which results in a deformation map $\phi_v(x, t);$
 Set $B = \phi_v(B_{left}, \frac{\lfloor N/2 \rfloor + 1}{N})$ which means we transport B_{left} along the geodesic and stop at time $t = \frac{\lfloor N/2 \rfloor + 1}{N};$
end
else
 $B = S_1$
end

Algorithm 3: Pairwise Centroid

5.2.3 Implementation

The methods presented just before need some parameters. Indeed, in each algorithm we have to compute the matching from one surface to another. For each matching we minimize the corresponding functional (see equation 3.9 at the end of section 3.3.1) which estimates the new momentum vectors α , which then are used to update the positions of points x_i of the surface. A gradient descent with adaptive step size is used for the minimization of the functional J . Evaluation of the func-

tional and its gradient require numerical integrations of high-dimensional ordinary differential equations, which is done using Euler trapezoidal rule.

The main parameters for computing J are *maxiter* which is the maximum number of iterations for the adaptive step size gradient descent algorithm, γ for the regularity of the matching, and σ_W and σ_V the sizes of the kernels which control the metric of the spaces W and V .

We selected parameters in order to have relatively good matchings in a short time. We chose γ close enough to zero to enforce the matching to bring the first object to the second one. Nevertheless, we must be prudent: choosing a γ too small could be hazardous because the regularity of the deformation could not be preserved. For each pairwise matching, we use the multi-scale approach described in section 3.3.1 page 62, performing four consecutive optimization processes with decreasing values by a constant factor of the σ_W parameter which is the size of the R.K.H.S. W , to increase the precision of the matching. At the beginning, we fix this σ_W parameter with a sufficient large value in order to capture the possible important variations or differences between shapes. This is for this reason that for the two first minimizations of the functional, we used a small *maxiter* parameter. For the results presented after, we used very small values for the parameter *maxiter* = [50, 50, 100, 300], to increase the velocity of the method. Results can be less accurate than in our previous study [Cury et al. \(2013\)](#) which used different values for *maxiter*: [40, 40, 100, 1000], but which took twice as much time to compute. For the kernel size σ_V of the deformation space, we fix this parameter at the beginning and have to adapt it to the size of the data.

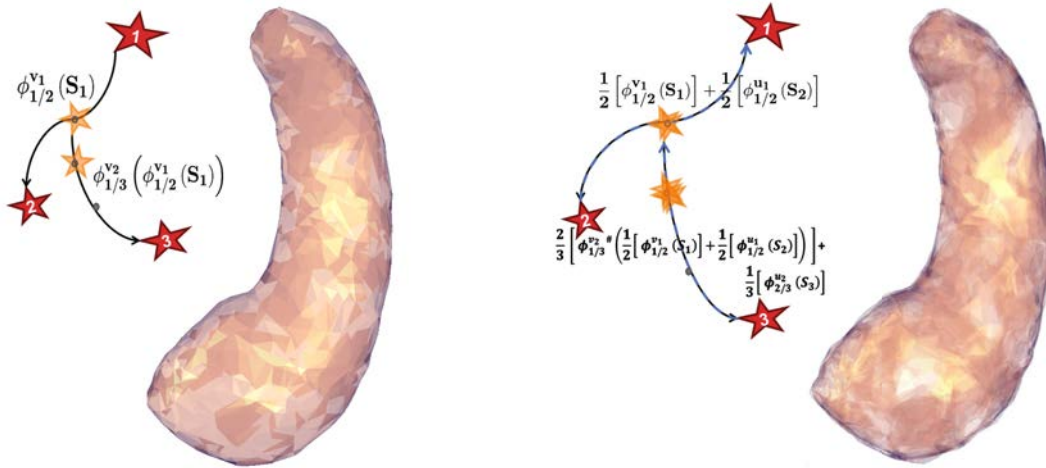


Figure 5.3: On the left, an Iterative Centroid of the dataset Data2 (see section 5.3.1 for more details about datasets) computed using the IC1 algorithm, and on the right the IC2 algorithm.

The first method starts from N surfaces, and gives a centroid composed by only one surface, which is a deformation of the surface used at the initialization step. An example is shown in Fig. 5.3. This method is rather fast, because at each step we have to match only one mesh composed by n_1 vertices to another, where n_1 is the number of vertices of the first mesh of the iterative procedure.

The second method starts from N surfaces and gives a centroid composed of deformations of all surfaces of the population. At each step it forms a combination in the space of currents between the current centroid and a backward flow of the new surface being matched. In practice this implies that the centroid grows in complexity; at step i its number of vertices is $\sum_{j=1}^i j * n_j$. Hence this algorithm is slower than the first one, but the mesh structure of the final centroid does not depend on the mesh of only one subject of the population, and the combination compensates the bias introduced by the inaccuracy of matchings.

The results of the Iterative Centroid algorithms depend on the ordering of subjects. We will study this dependence in the experimental part, and also study the effect of stopping the I.C. before it completes all iterations.

5.3 Results

We are using as comparison the variational template estimation method proposed by [Glaunès & Joshi \(2006\)](#) and presented in section 3.5. As the diffeomorphic iterative centroid method, this method does not need a priori on the template or external initialization.

5.3.1 Data

To evaluate our approach, we used hippocampi from 95 young (14-16 years old) subjects from the European database IMAGEN. Left hippocampi were segmented from T1-weighted Magnetic Resonance Images (MRI) of this database with the SACHA software [Chupin et al. \(2009\)](#), before computing meshes from the binary masks using BrainVISA software¹.

We denote as RealData the dataset composed of all 95 hippocampi meshes. We rigidly aligned all hippocampi to one subject of the population. For this rigid registration, we used a similarity term based on measures (as in [Glaunès et al. \(2004\)](#)) rather than currents since the orientation information given by the representation with currents can be an issue when surfaces are far and would need a large translation, or entirely included one into the other and would need a large scaling.

1. <http://www.brainvisa.info>

We also built two synthetic populations of hippocampi meshes, denoted as Data1 and Data2. Data1 is composed of a large number of subjects, in order to test our algorithms on a large dataset. In order to study separately the effect of the population size, meshes of this population are simple. Data2 is a synthetic population close to the real one, with the difference that all subjects have the same mesh structure. This allows to test our algorithms in a population with a single mesh structure, thus disregarding the effects of different mesh structures. These two datasets are defined as follows (examples of subjects from these datasets are shown on Fig. 5.4):

- Data1. We chose one subject S_0 that we decimated (down to 135 vertices) and deformed using geodesic shooting in 500 random directions with a sufficiently large kernel and a reasonable momentum vector norm in order to preserve the overall hippocampal shape, resulting in 500 deformed objects. Each deformed object was then further transformed by a translation and a rotation of small magnitude. This resulted in the 500 different shapes of Data1. All shapes in Data1 have the same mesh structure. Data1 thus provides a large dataset with simple meshes and mainly global deformations.
- Data2. We chose the same initial subject S_0 that we decimated to 1001 vertices. We matched this mesh to each subject of the dataset RealData ($n = 95$), using diffeomorphic deformation, resulting in 95 meshes with 1001 vertices. Data2 has more local variability than Data1, and is closer to the anatomical truth.

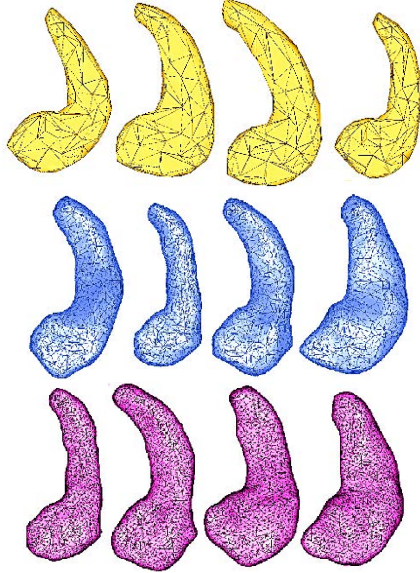


Figure 5.4: Top to bottom: meshes from Data1 (n=500), Data2 (n=95) and RealData (n=95)

5.3.2 Effect of subject ordering

Each of the 3 proposed algorithms theoretically depends on the ordering of subjects. Here, we aim to assess the influence of the ordering of subjects on the final centroid for each algorithm.

For that purpose, we compared several centroids computed with different orderings. For each dataset and each algorithm, we computed 10 different centroids. We computed the mean $m1$ and maximal distance between all pairs of centroids. The three datasets have different variabilities. In order to relate the previous mean distance to the variability, we also computed the mean distance $m2$ between each centroid and all subjects of a given dataset. We finally computed the ratio between these two mean distances $m1/m2$. Distances between surfaces were computed in

the space of currents, i.e. to compare two surfaces S and T , we computed the squared norm $\|[S] - [T]\|_{W^*}^2$. Results are presented in Table 5.1. Additionally, we computed the mean of distances between centroids computed using the different methods. Results are presented in Table 5.2.

Table 5.1: Distances between centroids computed with different subjects orderings, for each dataset and each of the 3 algorithms. The three first columns present the mean, standard deviation and the maximum of distances between all pairs of centroids computed with different orderings. The fourth column displays the mean of distances between each centroid algorithm and all subjects of the datasets. Distances are computed in the space of currents.

		From different order:			To the dataset:	$m1/m2$
		mean ($m1$)	max	std	mean ($m2$)	
Data1	IC1	0.8682	1.3241	0.0526	91.25	0.0095
	IC2	0.5989	0.9696	0.0527	82.66	0.0072
	PW	3.5861	7.1663	0.1480	82.89	0.0433
Data2	IC1	2.4951	3.9516	0.2205	16.29	0.1531
	IC2	0.2875	0.4529	0.0164	15.95	0.0181
	PW	3.8447	5.3172	0.1919	17.61	0.2184
RealData	IC1	4.7120	6.1181	0.0944	18.54	0.2540
	IC2	0.5583	0.7867	0.0159	17.11	0.0326
	PW	5.3443	6.1334	0.1253	19.73	0.2708

Table 5.2: In columns, average distances between centroids computed using the different algorithms.

	IC1 vs IC2	IC1 vs PW	IC2 vs PW
Data1	1.57	5.72	6.31
Data2	1.89	3.60	3.42
RealData	3.51	5.31	4.96

For each dataset and for each type of centroid, the mean of distances between

all 10 centroids is small compared to the mean of distances between the centroid and the subjects. However, the three algorithms IC1, IC2 and PW were not equally influenced by the ordering. IC2 seems to be the most stable: the different centroids are very close one to each other, this being true for all datasets. This was expected since we reduce the matching error by combining in the space of currents the actual centroid with the deformation of the new subject along the reverse flow. For IC1, the distance was larger for Data2 and RealData, which have anatomically more realistic deformations, than for Data1, which has rather simplistic shapes. This suggests that, for real datasets, IC1 is more dependent on the ordering than IC2. This is due to the fact that IC1 provides a less precise estimate of the centroid between two shapes since it does not incorporate the reverse flow. For all datasets, distances for PW were larger than those for IC1 and IC2, suggesting that the PW algorithm is the most dependent on the subjects ordering. Furthermore, centroids computed with PW are also farther from those computed using IC1 or IC2. Furthermore, we speculate that the increased sensitivity of PW over IC1 may be due to the fact that, in IC1, $n - 1$ levels of averaging are performed (and only $\log_2 n$ for PW) leading to a reduction of matching errors.

Finally, in order to provide a visualization of the differences, we present matchings between 3 centroids computed with the IC1 algorithm, in the case of RealData. Figure 5.5 shows that shape differences are local and residual. Visually, the 3 centroids are almost similar, and the amplitudes of momentum vectors, which bring one centroid to another, are small and local.

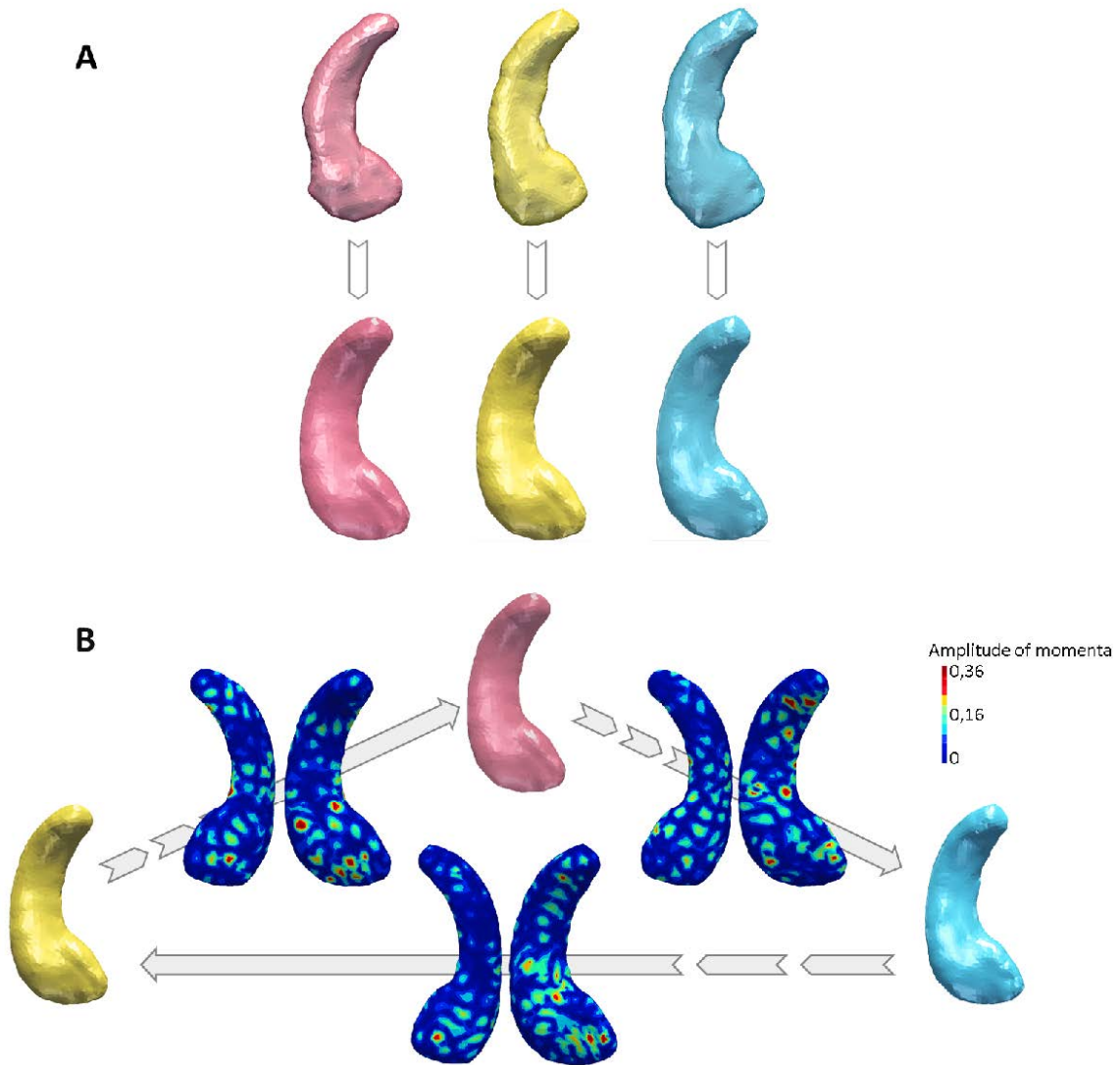


Figure 5.5: A. First row: 3 initial subjects used for 3 different centroid computations with IC1 (mean distance between such centroids, in the space of currents, is 4.71) on RealData. Second row: the 3 centroids computed using the 3 subjects from the first row as initialization. B: Maps of the amplitude of the momentum vectors that map each centroid to another. Top and bottom views of the maps are displayed. One can note that the differences are small and local.

5.3.3 Position of the centroids within the population

We also assessed whether the centroids are close to the center of the population. To that purpose, we calculated the ratio

$$R = \frac{\|\frac{1}{N} \sum_{i=1}^N v_0(S_i)\|_V}{\frac{1}{N} \sum_{i=1}^N \|v_0(S_i)\|_V}, \quad (5.8)$$

with $v_0(S_i)$ the vector field corresponding to the initial momentum vector of the deformation from the variational template or the centroid to the subject i . This ratio gives some indication about the centering of the centroid, because in a pure Riemannian setting (i.e. disregarding the inaccuracies of matchings), a zero ratio would mean that we are at a critical point of the Fréchet functional, and under some reasonable assumptions on the curvature of the shape space in the neighbourhood of the dataset (which we cannot check however), it would mean that we are at the Fréchet mean. To compute R , we need to match the centroid to all subjects of the population. We computed this ratio on the best (i.e. the centroid which is the closest to all other centroids) centroid for each algorithm and for each dataset.

Results are presented in Table 5.3. We can observe that the centroids obtained with the three different algorithms are reasonably centered for all datasets. Centroids for Data1 are particularly well centered, which was expected given the nature of this population. Centroids for Data2 and RealData are slightly less well centered but they are still close to the Fréchet mean. It is likely that using more accurate matchings (and thus increasing the computation time of the algorithms) we could reduce this ratio for RealData and Data2. Besides, one can note that ratios for Data2 and RealData are very similar; this indicates that the centering of the centroid is not altered by the variability of mesh structures in the population.

Table 5.3: Ratio values for assessing the position of the representative centroid within the population, computed using Equation 5.8 (for each algorithm and for each dataset).

R	IC1	IC2	PW
Data1	0.046	0.038	0.085
Data2	0.106	0.102	0.107
RealData	0.106	0.107	0.108

5.3.4 Effects of initialization on estimated variational template

The initial idea was to have a method which provides a good initialization for variational template estimation methods for large databases. We just saw that IC1 and IC2 centroids are both reasonably centred and do not depend on the subjects ordering. Despite the fact that IC2 has the smallest sensitivity to the subjects ordering, the method is slower and provides a centroid composed of N meshes. Because we want to decrease the computation time for the variational template of a large database, it is natural to choose as initialization a centroid composed by only one mesh (time saved in kernel convolution) in a short time. We advocate to choose IC1 over PW because we can stop the IC1 algorithm at any step to get a centroid of the sub-population used so far. Furthermore, PW seems to be more sensitive to subjects ordering.

Now, we study the impact of the use of a centroid, computed with the IC1 algorithm, as initialization for the variational template estimation method presented in section 3.5 page 75. To that purpose, we compared the variational template obtained using a standard initialization, denoted as $T(StdInit)$, to the variational

Table 5.4: Distances between variational templates initialized via different IC1 ($T(IC1)$) for each dataset, and the distance between the variational template initialized via the standard initialization ($T(StdInit)$) and variational templates initialized via IC1.

	$T(IC1)$ vs $T(IC1)$	$T(IC1)$ vs $T(StdInit)$
Data1	0.9833	40.9333
Data2	0.6800	20.4666
RealData	4.0433	26.8667

Table 5.5: Ratios R for variational templates ($T(IC1)$) and for the variational template with its usual initialization $T(StdInit)$, for each dataset.

R	$T(IC1)$	$T(StdInit)$
Data1	0.0057	0.0062
Data2	0.0073	0.0077
RealData	0.0073	0.0074

template initialized with IC1 centroid, denoted as $T(IC1)$. We chose to stop the variational template estimation method after 7 iterations of the optimization process. We arbitrarily chose this number of iterations, it is large enough to have a good convergence for $T(IC1)$ and to have an acceptable convergence for $T(StdInit)$. We did not use a stopping criterion based on the W^* metric because it is highly dependent on the data and is difficult to establish when using a multiscale approach. In addition to comparing $T(IC1)$ to $T(StdInit)$, we also compared the variational templates corresponding to two different IC1 initializations based on two different orderings. We compared the different variational templates in the space of currents. Results are presented in Table 5.4. We also computed the same ratios R as in equation 5.8. Results are presented in Table 5.5.

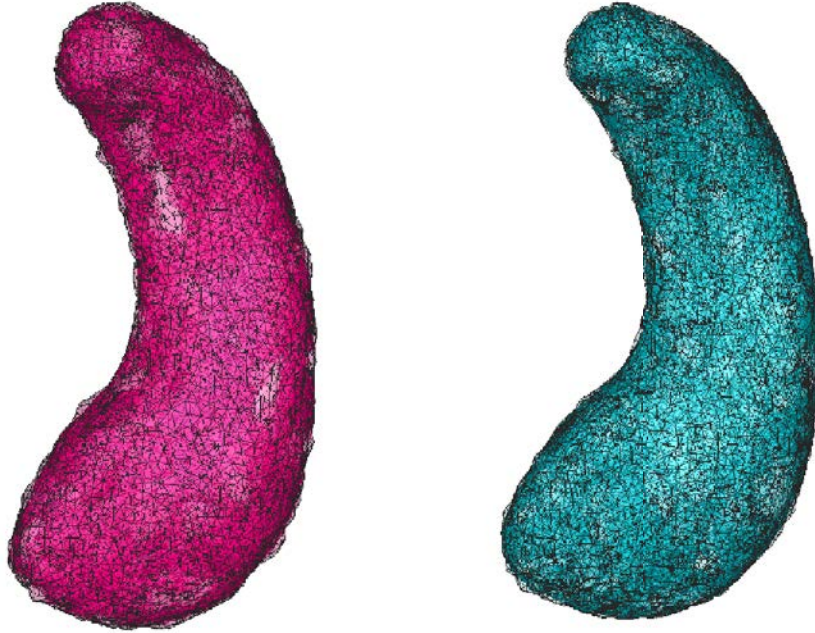


Figure 5.6: Estimated variational template from RealData. On the left, initialized via the standard initialization which is the whole population. On the right, estimated variational template initialized via a IC1 centroid

One can note that the differences between $T(IC1)$ for different orderings are small for Data1 and Data2 and larger for RealData, suggesting that these are due to the mesh used for the initialization step. We can also observe that variational templates initialized via IC1 are far, in terms of distances in the space of currents, from the variational template initialized by the standard initialization. These results could be alarming, but the results of ratios (see Table 5.5) prove that variational templates are all very close to the Fréchet mean, and that the differences are not due to a bad variational template estimation. Moreover, both variational templates are visually similar as seen in Figure 5.6.

5.3.5 Effect of the number of iterations for Iterative Centroids

Since it is possible to stop the Iterative Centroid methods IC1 and IC2 at any step, we wanted to assess the influence of computing only a fraction of the N iterations on the estimated variational template. Indeed one may wonder if computing an I.C. at e.g. 40% (then saving 60% of computation time for the IC method) could be enough to initialize a variational template estimation. Moreover, for large datasets, the last subject will have a very small influence: for a database composed of 1000 subjects, the weight of the last subject is $1/1000$. We performed this experiment in the case of IC1. In the following, we call "IC1 at $x\%$ " an IC1 computed using $x \times N/100$ subjects of the population.

We computed the distance in the space of currents between "IC1 at $x\%$ " and IC1. Results are presented in Figure 5.7. These distances are averaged over the 10 centroids computed for each datasets. We can note that after processing 40% of the population, the IC1 covers more than 75% of the distance to the final centroid for all datasets.

We also compared $T(\text{IC1 at } 40\%)$ to $T(\text{IC1})$ and to $T(\text{StdInit})$, using distances in the space of currents, as well as the R ratio defined in Equation 5.8. Results are shown in Table 5.6). They show that using 40% of subjects lowers substantially the quality of the resulting variational template. Indeed the estimated variational template seems trapped in the local minimum found by the IC1 at 40%. We certainly have to take into account the size of the dataset. Nevertheless, we believe that if the dataset is very large and sufficiently homogeneous we could stop the Iterative

Table 5.6: Results of initialization of variational template estimation method by a IC1 at 40%

	Data1	Data2	RealData
$T(\text{IC1 at } 40\%) \text{ vs } T(\text{StdInit})$	41.41	24.41	24.82
$T(\text{IC1 at } 40\%) \text{ vs } T(\text{IC1 at } 100\%)$	9.36	9.56	6.18
R value for $T(\text{IC1 at } 40\%)$	0.040	0.106	0.105

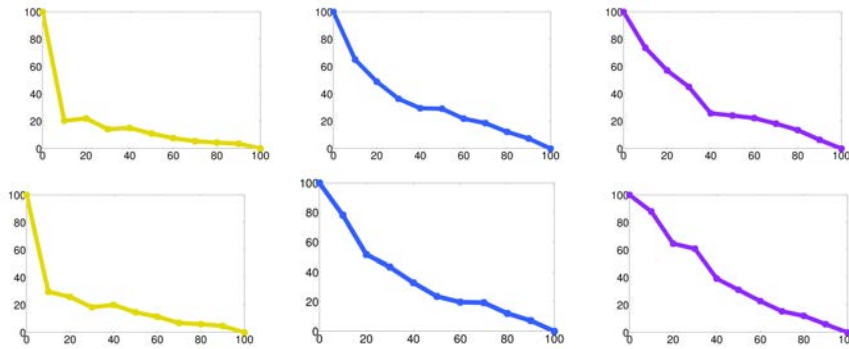


Figure 5.7: first row: Graphs of average W^* -distances between the IC1 at $x\%$ and the final one. The second row present the same results with IC2.

Centroid method before the end.

5.3.6 Computation time

To speed up the matchings, we use a GPU implementation for the computation of kernel convolutions, which constitutes the most time-consuming part of LDDMM methods. Computations were performed on a Nvidia Tesla C1060 card. Computation times are displayed in Table 5.7.

We can note that the computation time of IC1 is equal to the one of PW and that these algorithms are faster than the IC2 algorithm, as expected. The computation time for any IC method (even for IC2) is much lower (by a factor from 10 to 80) than

Table 5.7: Computation time (in hours) for Iterative Centroids and for variational template estimation initialised by IC1 ($T(IC1)$), the standard initialization ($T(StdInit)$) and by IC1 at 40% (T(IC1 at 40%)). For $T(IC1)$, we give the complete time for the whole process i.e. the time for the IC1 computation plus the time for $T(IC1)$ computation itself.

Computation time (hrs)	Data1	Data2	RealData
IC1	1.7	0.7	1.2
IC2	5.2	2.4	7.5
PW	1.4	0.7	1.2
$T(IC1)$	21.1(= 1.7 + 19.4)	13.3(= 0.7 + 12.6)	27.9(= 1.2 + 26.7)
$T(StdInit)$	96.1	20.6	99
T(IC1 at 40%)	24.4(= 0.7 + 23.7)	10.4(= 0.3 + 10.1)	40.7(= 0.5 + 40.2)

the computation time of the variational template estimation method. Moreover, initializing the variational template estimation with IC1 can save up to 70% of computation time over the standard initialization. On the other hand, using T(IC1 at 40%) does not reduce computation time compared to using T(IC1).

It could be interesting to evaluate the parameters which would lead to a more precise centroid estimate in a time that would still be inferior to that needed for the variational template estimation. We should also mention that one could speed up computations by adding a Matching Pursuit on currents as described in [Durrleman et al. \(2009\)](#).

5.4 Discussion

We have proposed a new approach for the initialization of the variational template estimation method presented by [Glaunès & Joshi \(2006\)](#). The aim was to

reduce computation time by providing a rough initial estimation, making more feasible the application of variational template estimation on large databases.

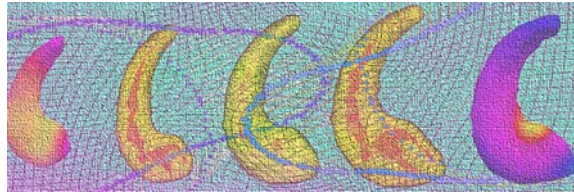
To that purpose, we proposed to iteratively compute a centroid which is correctly centered within the population. We proposed three different algorithms to compute this centroid: the first two algorithms are iterative (IC1 and IC2) and the third one is recursive (PW). We evaluated the different approaches on one real and two synthetic datasets of brain anatomical structures. Overall, the centroids computed with all three approaches are close to the Fréchet mean of the population, thus providing a reasonable centroid or initialization for variational template estimation method. Furthermore, for all methods, centroids computed using different orderings are similar. It can be noted that IC2 seems to be more robust to the ordering than IC1 which in turns seems more robust than PW. Nevertheless, in general, all methods appear relatively robust with respect to the ordering.

The advantage of iterative methods, like IC1 and IC2, is that we can stop the deformation at any step, resulting in a centroid built with part of the population. Thus, for large databases (composed for instance of 1000 subjects), it may not be necessary to include all subjects in the computation since the weight of these subjects will be very small. The iterative nature of IC1 and IC2 provides another interesting advantage which is the possible online refinement of the centroid estimation as new subjects are entered in the dataset. This leads to an increased possibility of interaction with the image analysis process. On the other hand, the recursive PW method has the advantage that it can be parallelized (still using GPU implementation), although we did not implement this specific feature in the present work.

Using the centroid as initialization of the variational template estimation can substantially speed up the convergence. For instance, using IC1 (which is the fastest one) as initialization saved up 70% of computation time. Moreover, this method could certainly be used to initialize other template estimation methods, such as the method proposed by [Durrleman et al. \(2008a\)](#).

As we observed, the centroids, obtained with rough parameters, are close to the Fréchet mean of the population, thus we believe that by computing IC with more precise parameters (but still reasonable in terms of computation time), we could obtain centroids closer to the center. This accurate centroid could be seen as a cheap alternative to true template estimation methods, particularly if computing a precise mean of the population of shapes is not required. Indeed, in the LDDMM framework, template-based shape analysis gives only a first-order, linearized approximation of the geometry in shape space. In a future work, we will study the impact of using IC as a cheap template on results of population analysis based for instance on kernel principal component analysis. Finally, the present work deals with surfaces for which the metric based on currents seems to be well-adapted. Nevertheless, the proposed algorithms for centroid computation are general and could be applied to images, provided that an adapted metric is used.

CHAPTER 6



STATISTICAL SHAPE ANALYSIS USING DIFFEOMORPHIC ITERATIVE CENTROIDS

In this chapter, we apply the diffeomorphic iterative centroid method to template-based statistical shape analysis. Here, the Centroid is directly used as a template, instead of being used as an initialization for a more refined template estimation. The main part of this chapter has been submitted to the IEEE Journal of Biomedical and Health Informatics.

6.1 Introduction

Statistical shape analysis methods are increasingly used in neuroscience and clinical research. Their applications include the study of correlations between anatomical structures and genetic or cognitive parameters, as well as the detection of alterations associated with neurological disorders. A current challenge for methodological research is to perform statistical analysis on large databases, which are needed to improve the statistical power of neuroscience studies.

In this chapter, we propose a fast approach for template-based statistical analysis of large datasets in the LDDMM setting presented in Chapter 3. The template estimation is based on the diffeomorphic centroid algorithm, which we introduced in Chapter 5. The main idea of this method is to iteratively update a centroid shape by successive matchings to the different subjects. This procedure involves a limited number of matchings and thus quickly provides a template of the population. We previously showed that these centroids can be used to initialize a variational template estimation procedure (Chapter 5). Here, we propose to use them directly for template-based statistical shape analysis. The analysis is done on the tangent space of the template shape, either directly through Principal Component Analysis or by approximating distances between subjects. We perform a thorough evaluation of the approach using three datasets (one synthetic dataset and two real datasets composed of 50 and 1000 subjects respectively). In particular, we study extensively the impact of different centroids on statistical analysis, and compare the results to those obtained using a standard variational template method. Finally we use this template-based approach and a large database composed of 1000 subjects to try to

predict incomplete hippocampal inversions (IHI) scores presented in Chapter 4.

6.2 Evaluation of iterative centroids

6.2.1 Statistical Analysis

The proposed iterative centroid approaches can be used for subsequent statistical shape analysis of the population, using various strategies. As presented in chapter 3, section 3.4.1, a first strategy consists in analysing the initial momentum vectors which encode the optimal diffeomorphisms computed from the matching between a centroid and the subjects S_i . A second strategy consists in computing the set of pairwise distances between subjects and use methods such as Isomap [Tenenbaum et al. \(2000\)](#), Locally Linear Embedding [Roweis & Saul \(2000\)](#), [Yang et al. \(2011a\)](#) or spectral clustering algorithms [Von Luxburg \(2007\)](#). Here, we tested two approaches: i) the analysis of initial momentum vectors using PCA for the first strategy; ii) the approximation of pairwise distance matrices for the second strategy. These tests allow us both to validate the different iterative centroid methods and to show the feasibility of such analysis on large databases.

6.2.1.1 Principal Component Analysis on initial momentum vectors

The PCA in the tangent space of the template shape, i.e. on the initial momentum vectors from the template to the subjects, corresponds to the usual Principal Component Analysis using the LDDMM metric on momentum vectors, as previously exposed in section 3.4.2 page 74. For this metric scalar products between observa-

tions are expressed using the kernel K_V associated to the space V of velocity fields. We refer to section 3.4.2 for details of this method.

Remark To analyse the population, we need to know the initial momentum vectors α^i which correspond to the matchings from the centroid to the subjects. For the IC1 and PW centroids, these initial momentum vectors were obtained by matching the centroid to each subject. For the IC2 centroid, since the mesh structure is composed of all vertices of the population, it is too expensive to match the centroid toward each subject. Instead, we matched each subject toward the centroid and we used the opposite vector of final momentum vectors for the analysis. Indeed, if we have two surfaces S and T and need to compute the initial momentum vectors from T to S , we can estimate the initial momentum vectors $\alpha^{TS}(0)$ from T to S by computing the deformation from S to T and using the initial momentum vectors $\tilde{\alpha}^{TS}(0) = -\alpha^{ST}(1)$, which are located at vertices $\phi_{ST}(\mathbf{x}^S)$.

6.2.1.2 Distance matrix approximation

As explained in section 3.4.1 computing all pairwise deformation distances $\rho(S_i, S_j) = D(id, \varphi_{ij})$ is computationally very expensive for large datasets as it involves $O(N^2)$ matchings, which led us to use a first order approximation evaluated from the N matchings from the centroid shape (see equation 3.18).

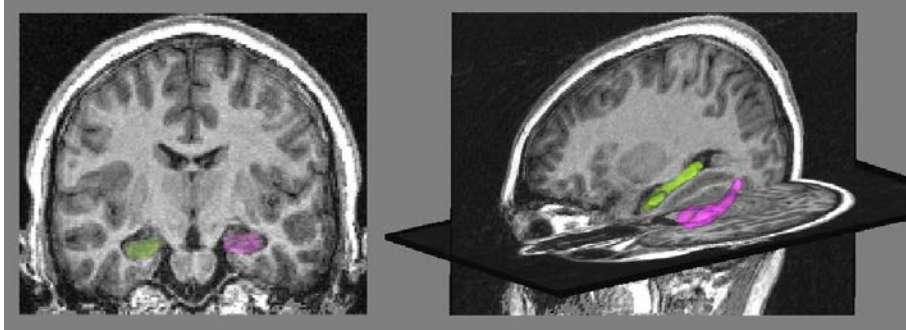


Figure 6.1: Left panel: coronal view of the MRI with the binary masks of hippocampi segmented by the SACHA software [Chupin et al. \(2009\)](#), the right hippocampus is in green and the left one in pink. Right panel: 3D view of the hippocampus meshes.

6.2.2 Data

The two real datasets are from the European database IMAGEN [Schumann et al. \(2010\)](#)¹ composed of young healthy subjects. We segmented the hippocampi from T1-weighted Magnetic Resonance Images (MRI) of subjects using the SACHA software [Chupin et al. \(2009\)](#) (see Fig. 6.1). The synthetic dataset was built using deformations of a single hippocampal shape of the IMAGEN database.

The synthetic dataset SD it is composed of synthetic deformations of a single shape S_0 and was designed in order that this single shape is the exact center of the population. We will thus be able to compare the computed centroids to this exact center. We generated 50 subjects for this synthetic dataset by shootings, from this single shape S_0 , along geodesics in different directions. We randomly chose two orthogonal momentum vectors β_1 and β_2 in $\mathbb{R}^{3 \times n}$. We then computed momentum vectors α^i , $i \in \{1, \dots, 25\}$ of the form $k_1^i \beta_1 + k_2^i \beta_2 + k_3^i \beta_3$ with $(k_1^i, k_2^i, k_3^i) \in$

1. <http://www.imagen-europe.com/>

$\mathbb{R}^3, \forall i \in \{1, \dots, 25\}, k_j^i \sim \mathcal{N}(0, \sigma_j)$ with $\sigma_1 > \sigma_2 \gg \sigma_3$ and β_3 a randomly selected momentum vector. We then computed momentum vectors $\alpha^j, j \in \{26, \dots, 50\}$ such as $\alpha^j = -\alpha^{j-25}$. We then generated the 50 subjects of the population by shootings of S_0 using the initial momentum vectors $\alpha^i, i \in \{1, \dots, 50\}$. The population is symmetrical since $\sum_i^{50} \alpha^i = 0$. It should be noted that all shapes of the dataset have the same mesh structure composed of $n = 549$ vertices.

The real dataset RD50 is composed by 50 left hippocampi well segmented from the IMAGEN database. We applied the following preprocessing steps to each individual MRI. First, the MRI was linearly registered toward the MNI152 atlas, using the FLIRT procedure [Jenkinson et al. \(2002\)](#) of the FSL software². The computed linear transformation was then applied to the binary masks of the hippocampal segmentations. Meshes of these segmentations were computed from the binary masks using the BrainVISA software³. All meshes were then aligned using rigid transformations to one subject of the population. For this rigid registration, we used a similarity term based on measures (as in [Glaunès et al. \(2004\)](#)) as in Chapter 5. All meshes were decimated in order to keep a reasonable number of vertices and to avoid falling below the resolution of the MRI used for the segmentation: meshes have on average 500 vertices.

The real database RD1000 is composed by 1000 left hippocampi well segmented from the IMAGEN database. We applied the same preprocessing steps to the MRI data as for the dataset RD50.

2. <http://fsl.fmrib.ox.ac.uk/fsl/fslwiki/FslOverview>

3. <http://www.brainvisa.info>

6.2.3 Experiments

For the datasets SD and RD50 (which both contain 50 subjects), we compared the results of the three different iterative centroid algorithms (IC1, IC2 and PW). We also investigated the possibility of computing variational templates, initialized by the centroids, based on the approach proposed by [Glaunès & Joshi \(2006\)](#) and summarized in section 3.5 page 75. We could thus compare the results obtained when using the centroid directly to those obtained when using the more expensive variational template estimation method. We thus computed 6 different templates: IC1, IC2, PW and the corresponding variational templates T(IC1), T(IC2), T(PW). For the synthetic dataset SD, we could also compare those 6 templates to the exact center of the population. For the real dataset RD1000 (with 1000 subjects), we only computed the iterative centroid IC1.

For all computed templates and all datasets, we investigated: 1) the computation time; 2) whether the templates are well-centred within the population; 3) the impact of the center on the results of PCA on tangent space; 4) the impact on approximated distance matrices.

To assess the centring of the different centroids and variational templates, we performed two experiments, one using the momentum vectors from templates to subjects, and one projecting templates into a 2D space to visualize the position of templates with respect to the population. These two experiments are detailed below, along with the results obtained for dataset SD.

We then compared the results of PCA in the tangent spaces computed from these different templates by comparing the principal modes, the position of subjects

Table 6.1: **Synthetic dataset SD.** Computation times in minutes for the different templates of the synthetic dataset.

	<i>Centroid</i>	$T(\textit{Centroid})$	Total
IC1	31	81	112
IC2	85	87	172
PW	32	81	113

within the space spanned by the first modes, and the cumulative explained variance for different number of dimensions.

Finally, we compared the approximated distance matrices to the direct distance matrix.

6.2.4 Synthetic dataset SD

6.2.4.1 Computation time

The three centroids have been computed with the next arbitrary parameters (see section 5.2.3 page 132) chosen to be adapted to the data: $\sigma_V = 15$, $\sigma_W = [10, 6.6, 5, 4, 3.3, 2.8]$, $\gamma = 1\text{e-}7$ and $\textit{maxiter} = [100, 300, 300, 600, 800, 800]$. For the variational template we used $\sigma_V = 15$, $\sigma_{W_i} = 20 \times 0.7^{i-1}$ with $i \in \{1; \dots; 6\}$ the i -th optimization process, $\gamma = 1\text{e-}4$ and $\textit{maxiter} = 5000$. Computation times for the different centroids and variational templates are presented in Table 6.1. As a reference, we also computed a variational template with the standard initialisation (see section 3.5) whose computation took **194** min. Computing a centroid saved between 56% and 84% of computation time over the template with standard initialization and between 50% and 72% over the template initialized by the centroid.

Table 6.2: **Synthetic dataset SD.** Ratio R (equation 6.1) computed for the 3 centroids, and the 3 variational templates initialized via these centroids.

Ratio	Centroid	$T(\text{Centroid})$
IC1	0.04	0.04
IC2	0.03	0.04
PW	0.06	0.05

6.2.4.2 Centring of the centres

We first calculated the following ratio R which takes values between 0 and 1:

$$R = \frac{\|\frac{1}{N} \sum_{i=1}^N v^i(\cdot, 0)\|_V}{\frac{1}{N} \sum_{i=1}^N \|v^i(\cdot, 0)\|_V}, \quad (6.1)$$

with $v^i(\cdot, 0)$ the vector field of the deformation from the template to the subject S_i , corresponding to the vector of initial momentum vectors $\alpha^i(0)$.

Table 6.2 presents the values of the ratio R for each centroid and variational template.

In a pure Riemannian setting (i.e. disregarding the fact that matchings are not exact), a zero ratio would mean that we are at a critical point of the Fréchet functional, and under some reasonable assumptions on the curvature of the shape space in the neighbourhood of the dataset (which we cannot check however), it would mean that we are at the Fréchet mean. By construction, the ratio computed from the exact center using the initial momentum vectors α^i used for the construction of subjects S_i (as presented in section 6.2.2) is zero.

Ratios R are close to zero for all centroids and variational templates, indicating that they are close to the exact center. Furthermore, the residual value of R may be partly due to the non-exactitude of the matchings between the templates and

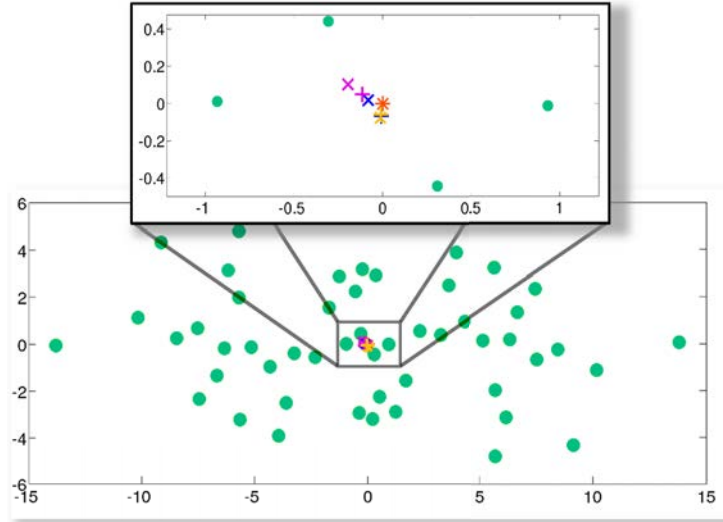


Figure 6.2: **Synthetic dataset SD.** Projection of the 6 templates (3 centroids and 3 variational templates) on the 2D space of the synthetic data. “ X ” represent centroids, “ + ” represent templates. IC1 is in blue, IC2 in yellow and PW in magenta. The exact centre is represented by the red asterisk.

the subjects. To become aware of this non-exactitude, we matched the exact center toward all subjects of the dataset. The resulting ratio is $R = 0.0466$. This is of the same order of magnitude as the ratios obtained in Table 6.2, indicating that the computed templates are indeed very close to the exact center.

To further assess the centring of the different templates, we visualized their position by projecting them on the 2D space of the population, with the exact center at position $(0,0)$. Indeed, since the exact center and the two first axes β_1 and β_2 (see section 6.2.2) were used to build the population are known, we can project any shape on the 2D space of the population spanned by (β_1, β_2) . This is done by matching the exact center to the shape and projecting the momentum vectors of this matching on β_1 and β_2 . The result is presented in Figure 6.2.

Overall, on the synthetic dataset, all computed centroids and variational templates are very well centred within the population and close to the exact center.

6.2.4.3 PCA

We performed PCA using initial momentum vectors (see section 3.4.2 for details) from our different templates (3 centroids, 3 variational templates and the exact centre). For this synthetic dataset, we can project principal components on the 2D space spanned by β_1 and β_2 as described in the previous paragraph. This projection allows displaying in the same 2D space subjects in their native space, and principal axes computed from the different PCAs. To visualize the first component (respectively the second one), we shot from the associated template in the direction $k\mathbf{m}^1$ (resp. \mathbf{m}^2) with $k \in [-2\sqrt{\lambda_1}; +2\sqrt{\lambda_1}]$ (resp. $\sqrt{\lambda_2}$). Results are presented in Figure 6.3. The principal axes are extremely similar for all templates.

We then computed the cumulative explained variance for different number of dimensions of the PCA. Results are presented in Table 6.3. The cumulative explained variances are very similar for the different templates for any number of dimensions.

Overall, for this synthetic dataset, the choice of a given template (i.e. a centroid, a variational template or an exact centre) has almost no impact on the results of the PCA computed on the tangent space of the template shape.

6.2.4.4 Distance matrices

We then studied the impact of different templates on the approximated distance matrices. We computed the seven approximated distance matrices corresponding to

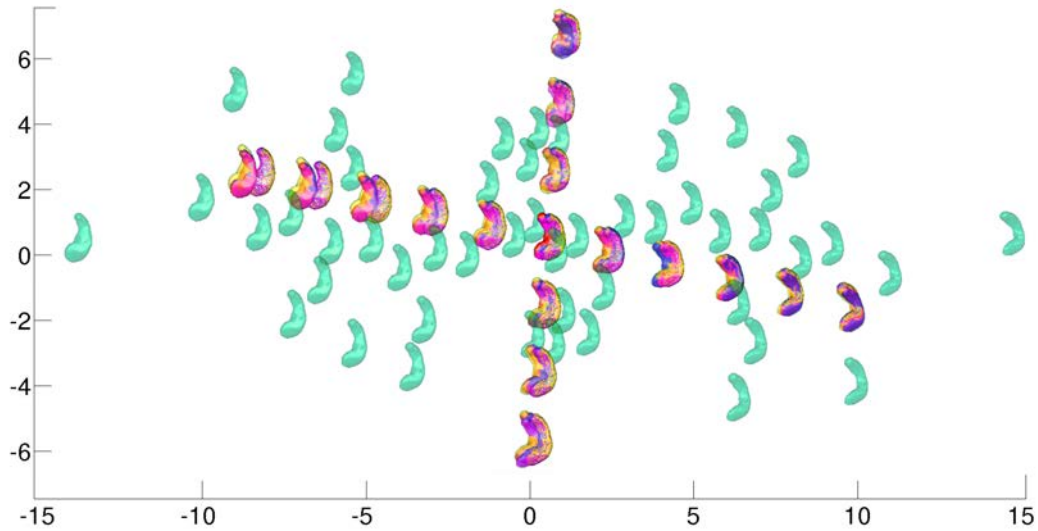


Figure 6.3: **Synthetic dataset SD.** Synthetic population in green, the exact center is in red. The two first components are marked in orange for the exact center, in blue for IC1, in yellow for IC2 and in magenta for PW.

Table 6.3: **Synthetic dataset SD.** Proportion of cumulative explained variance of PCA computed from different templates.

	1st mode	2nd mode	3rd mode
Centre	0.829	0.989	0.994
IC1	0.829	0.990	0.995
IC2	0.833	0.994	0.996
PW	0.829	0.990	0.995
T(IC1)	0.829	0.995	0.999
T(IC2)	0.829	0.995	0.999
T(PW)	0.829	0.995	0.999

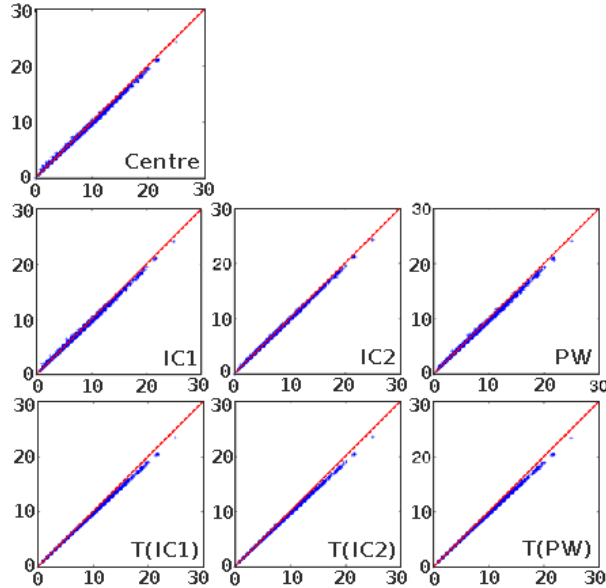


Figure 6.4: **Synthetic dataset SD.** Scatter plots between the direct distance matrix and the 7 approximated distance matrices, computed from the exact center, IC1, IC2, PW and the corresponding variational templates of the synthetic dataset. The red line corresponds to the identity

the seven templates, and the direct pairwise distance matrix computed by matching all subjects to each other. Computation of the direct distance matrix took 1000 minutes (17 hours) for this synthetic dataset of 50 subjects. In the following, we denote as $aM(C)$ the approximated distance matrix computed from the template C , and dM the direct distance matrix. Figure 6.4 shows that the approximated distance matrices for the different templates are very similar to the direct matrix. A very similar result was obtained when comparing the matrices approximated from the centroids and variational templates to the matrix approximated from the exact center (see Supplementary material). We can observe a subtle curvature of the scatter-plot, which is due to the curvature of the shape space.

Table 6.4: **Synthetic dataset SD.** Error e (equation 6.2) between the six different approximated distance matrices and the approximated distance matrix from the exact center (left column), and the direct distance matrix (right column).

	$e(\cdot, aM(\text{realCentre}))$		$e(\cdot, dM)$	
	C	$T(C)$	C	$T(C)$
IC1	0.01	0.02	0.03	0.03
IC2	0.02	0.02	0.02	0.03
PW	0.02	0.02	0.03	0.03

To quantify the difference between these matrices, we introduced the following error e :

$$e(M_1, M_2) = \frac{1}{N^2} \sum_{i,j=1}^N \frac{|M_1(i, j) - M_2(i, j)|}{\max(M_1(i, j), M_2(i, j))} \quad (6.2)$$

with M_1 and M_2 two distance matrices. Results are reported in Table 6.4. We also computed the error between the direct distance matrix and the $aM(\text{realCentre})$ and the value is **0.03**, which value is of the same order of magnitude than for others matrices.

In conclusion on this synthetic dataset, the different computed templates have very little impact on the approximation of the distance matrices.

6.2.5 The real dataset RD50

We now present experiments on the real dataset RD50. For this dataset, the exact center of the population is not known, neither is the distribution of the population, and meshes have different numbers of vertices and different connectivity structures.

6.2.5.1 Computation time

The three centroids have been computed with the next arbitrary parameters chosen to be adapted to the dataset: $\sigma_V = 15$, $\sigma_W = [15, 8, 5, 2]$, $\gamma = 1e-7$ and $maxiter = [200, 300, 800, 1000]$. For the variational template we used $\sigma_V = 15$, $\sigma_{W_i} = 16 \times 0.7^{i-1}$ with $i \in \{1; \dots; 8\}$ the i -th optimization process, $\gamma = 0.01$ and $maxiter = 5000$. Parameters are determined after matching tests between some surfaces of the dataset. We computed our 3 centroids IC1 IC2 and PW, and the corresponding variational templates. Computation times are reported in Table 6.5.

Table 6.5: **Real dataset RD50.** Computation times, in minutes.

	<i>Centroid</i>	$T(\textit{Centroid})$	Total
IC1	75	188	263
IC2	174	252	426
PW	88	183	271

For comparison of computation time, we also computed a variational template using the standard initialization (by using the whole population as initialisation) which took 1220 minutes (20.3 hours). Computing a centroid saved between 85% and 93% of computation time over the variational template with standard initialization and between 59% and 71% over the variational template initialized by the centroid.

6.2.5.2 Centring of the centres

As for the synthetic dataset, we assessed the centring of these six different templates. To that purpose, we first computed the ratio R of equation 6.1 in sec-

tion 6.2.4. Results are presented in Table 6.6.

Table 6.6: **Real dataset RD50.** Ratio R (equation 6.1) computed for 3 centroids and 3 variational templates initialized via these centroids.

Ratio	<i>Centroid</i>	$T(\textit{Centroid})$
IC1	0.25	0.21
IC2	0.33	0.31
PW	0.32	0.26

The ratios are higher than ratios computed from the synthetic dataset, indicating that templates are less centred. This was predictable since the population is not built from one surface via geodesic shootings as the synthetic dataset. In order to better understand these values, we computed the ratio for each subject of the population (after matching each subject toward the population), as if each subject was considered as a potential template of the population. For the whole population, the average ratio was 0.6745, with a minimum of 0.5543, and a maximum of 0.7626. These ratios are clearly larger than those of Table 6.6, thus the 6 templates are much better centred than any subject of the population.

The real dataset is not intrinsically two-dimensional, unlike the synthetic dataset, thus we can not project templates onto the corresponding 2D space. However, we illustrated the position of the templates by projecting them onto the space spanned by the two first modes of variation resulting from the PCA of a given template (here the centroid IC1 which is in coordinates $(0,0)$). The results are presented in Figure 6.5.

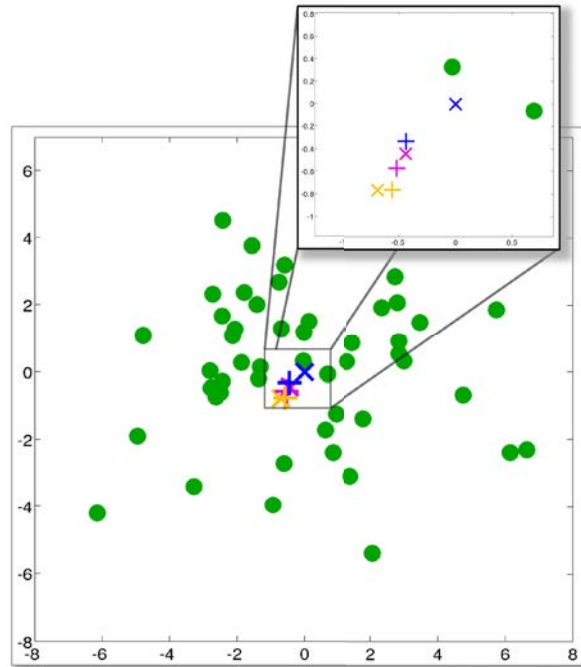


Figure 6.5: **Real dataset RD50.** Projection of the 5 other templates (2 centroids and 3 variational templates) in the 2D space spanned by the two first modes of the PCA computed from the centroid IC1. “ x ” represent centroids, “ + ” represent templates. IC1 is in blue, IC2 in yellow and PW in magenta.

6.2.5.3 PCA

As for the synthetic dataset, we performed six PCAs from these templates. For the first two components of the PCAs, we displayed the coordinates of the subjects for the 6 different templates in Figure 6.6, templates are at coordinates $(0, 0)$. Overall, the coordinates of the subjects are highly similar for the different templates. Besides, we can observe that PCAs from variational templates are more similar to each other than PCAs from centroids (as seen also for the positions of the templates themselves in Figure 6.5). This was expected since the variational template estimation converges from the centroid given as initialization.

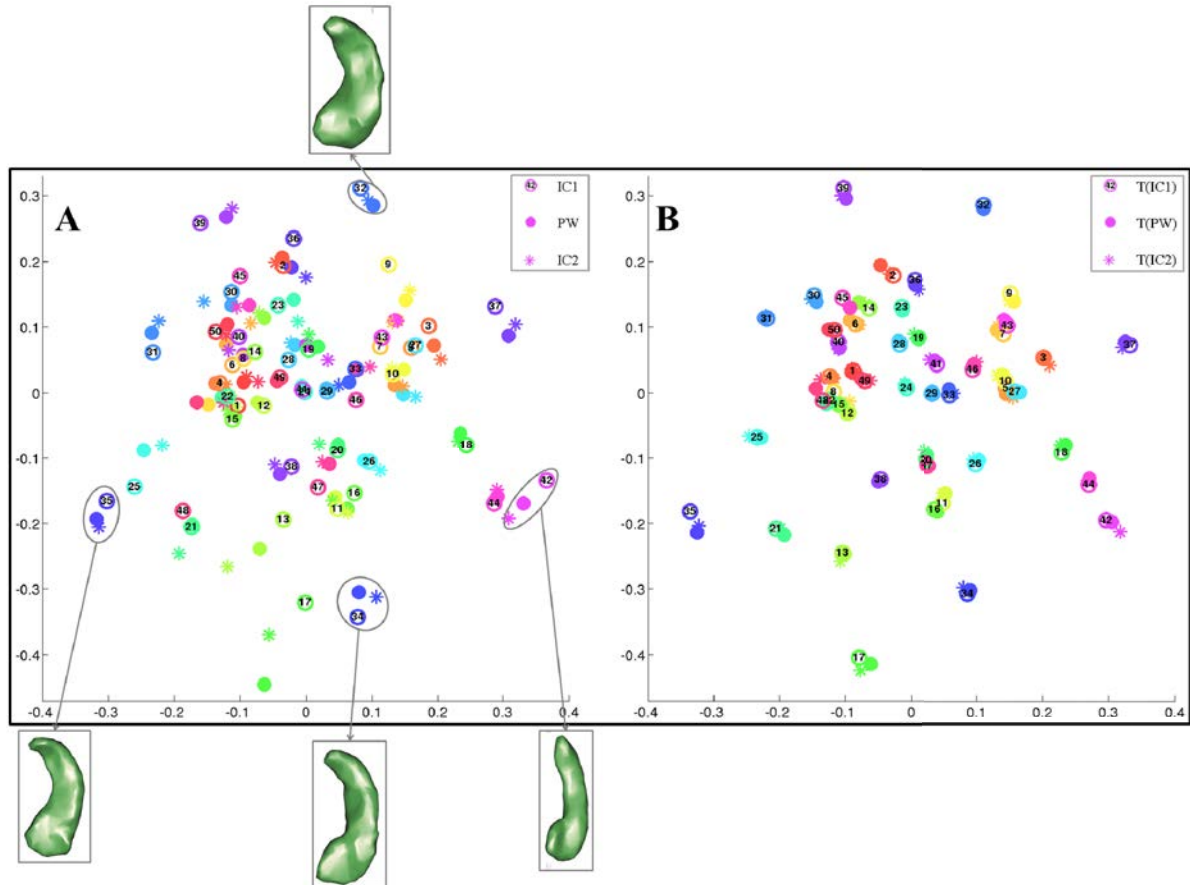


Figure 6.6: **Real dataset RD50.** Coordinates of the subjects in the 2D space spanned by the first two components of the PCAs computed from different templates. Panels A and B are superimpositions of the PCA from the 3 centroids (A) and from the 3 variational templates (B). There is one color per subject.

Table 6.7: **Real dataset RD50.** Proportion of cumulative explained variance for PCAs computed from the 6 different centres, for different number of dimensions

	1st mode	2nd mode	15th mode	20th mode
IC1	0.118	0.214	0.793	0.879
IC2	0.121	0.209	0.780	0.865
PW	0.117	0.209	0.788	0.875
T(IC1)	0.117	0.222	0.815	0.899
T(IC2)	0.115	0.220	0.814	0.898
T(PW)	0.116	0.221	0.814	0.898

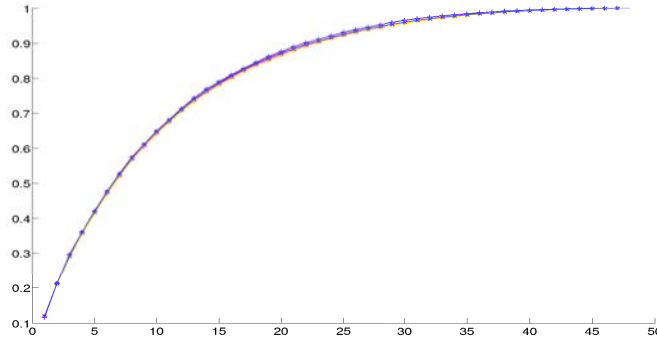


Figure 6.7: **Real dataset RD50.** Proportion of cumulative explained variance for PCAs computed from the 6 different templates, with respect to the number of dimensions. Curves are almost identical.

Figure 6.7 and Table 6.7 show the proportion of cumulative explained variance for different number of modes. We can note that for any given number of modes, all PCAs result in the same proportion of explained variance.

Additionally, we illustrated the 2D space generated by the two first modes of variation of a PCA corresponding to a given template (here the centroid IC1). To that purpose, we performed geodesic shootings from the template using the momentum vectors $k_1\mathbf{m}^1 + k_2\mathbf{m}^2$ with k_i from $-2\sqrt{\lambda_i}$ to $+2\sqrt{\lambda_i}$. Results are presented in Figure 6.8. We can observe that the first mode of variation of this dataset is

Table 6.8: **Real dataset RD50.** Errors e (equation 6.2) between the approximated distance matrices of each center and: i) the approximated matrix computed with IC1 (left columns); ii) the direct distance matrix (right columns).

	$e(., aM(IC1))$		$e(., dM)$	
	C	$T(C)$	C	$T(C)$
IC1	0	0.04	0.10	0.08
IC2	0.06	0.04	0.06	0.08
PW	0.03	0.04	0.08	0.07

influenced by the curvature of the tail and the width of the hippocampus, while the second mode seems to be linked with the length of the hippocampus, and on the shape of the head.

6.2.5.4 Distance matrices

As for the synthetic dataset, we then studied the impact of these different templates on the approximated distance matrices. A direct distance matrix was also computed and took around 90 hours of computation time, against 7 hours (426 min, see Table 6.5) for the approximated distance matrix computed from the slowest of the 6 templates, the variational template $T(IC2)$. We compared the approximated distance matrices of the different templates to: i) the approximated matrix computed with IC1; ii) the direct distance matrix.

We computed the errors $e(M_1, M_2)$ defined in equation 6.2. Results are presented in Table 6.8. Errors are small and with the same order of magnitude.

Figure 6.9 shows scatter plots between the direct distance matrix and the six approximated distance matrices. Interestingly, we can note that the results are similar to those obtained by Yang et al. ([Yang et al. \(2011b\)](#), Figure 2). Figure 6.10

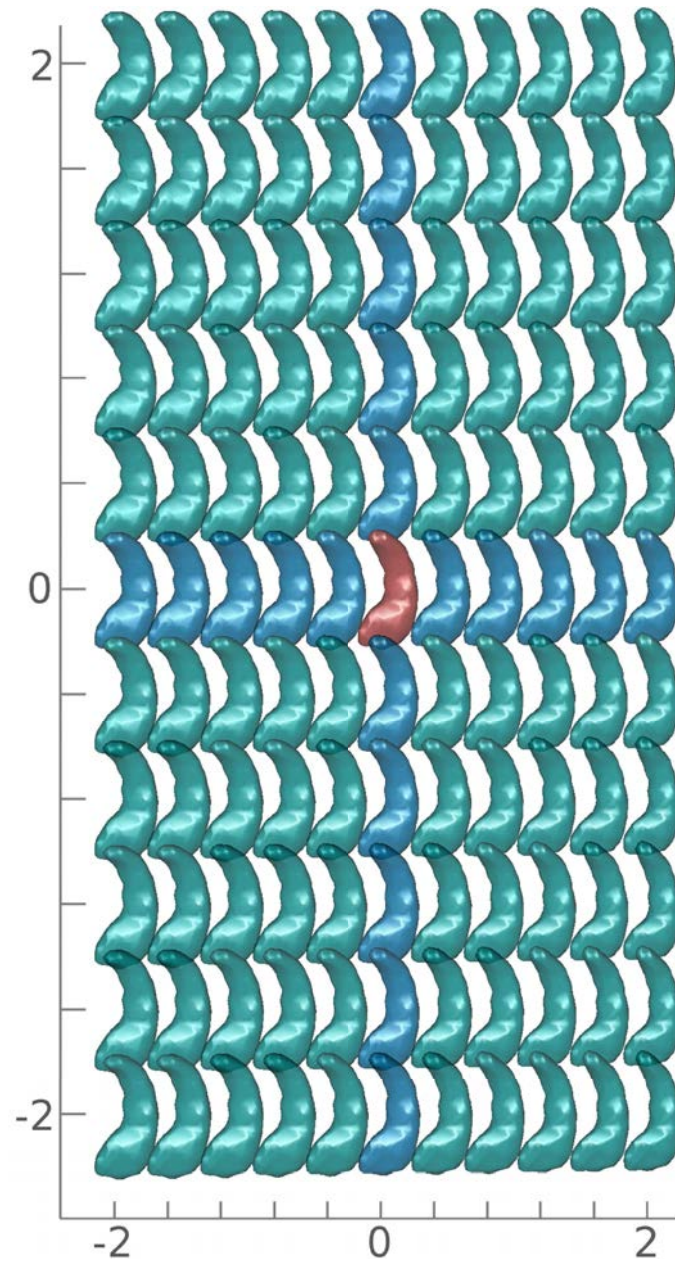


Figure 6.8: **Real dataset RD50.** Grid generated by the two first modes of variation of the PCA computed on the tangent space of IC1.

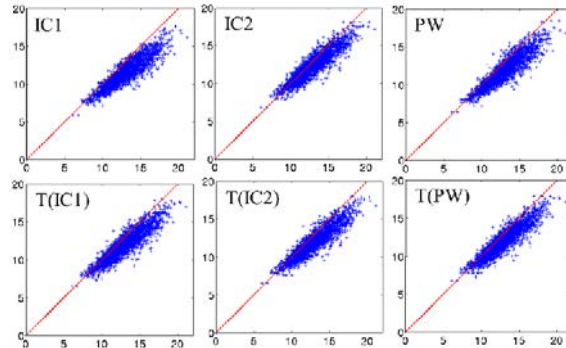


Figure 6.9: **Real dataset RD50.** Scatter plots between direct distance matrix and approximated distance matrices from the six templates. The red line corresponds to the identity.

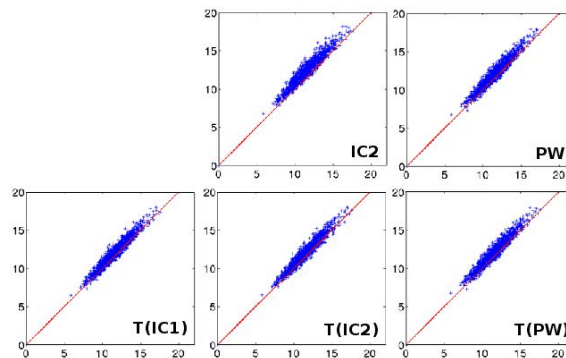


Figure 6.10: **Real dataset RD50.** Scatter plot between the $aM(IC1)$ matrix and the 5 others approximated distance matrices. The red line corresponds to the identity.

shows scatter plots between the approximated distance matrix from IC1 and the five others approximated distance matrices. The approximated matrices thus seem to be independent of the chosen template.

6.3 Variability analysis and prediction of IHI

6.3.1 Centroid estimation

Results on the real dataset RD50 and the synthetic SD showed that results were highly similar for the 6 different templates. In light of these results and because of the large size of the real dataset RD1000, we only computed the template IC1 for this last dataset. Parameters for the IC1 computation were the same as for the RD50 dataset. The computation time was about 832 min (13.8 hours) for the computation of the centroid using the algorithm IC1, and 12.6 hours for matching the centroid to the population.

The ratio R of equation 6.1 computed from the IC1 centroid was 0.1011, indicating that the centroid is well centred within the population.

We then performed PCA. Table 6.9 shows the proportion of cumulative explained variance for some selected number of dimensions. In addition, we explored the evolution of the cumulative explained variance when considering varying numbers of subjects in the analysis. Results are displayed in Figure 6.11. We can first note that about 50 dimensions are sufficient to describe the variability of our population of hippocampal shapes from healthy young subjects. When considering increasing number of subjects in the analysis, the dimension increases and converges around 50. Moreover, for large number of subjects, this dimensionality seems to be stable.

As for RD50, we computed a grid of the 2D space spanned by the two first modes of variation of the PCA. We then performed geodesic shootings using momentum vectors $k_1\mathbf{m}^1 + k_2\mathbf{m}^2$ with k_i from $-2\sqrt{\lambda_i}$ to $+2\sqrt{\lambda_i}$, and \mathbf{m}^1 and \mathbf{m}^2 the two first

Table 6.9: **Real dataset RD1000.** Proportion of cumulative explained variance, for PCA, computed from IC1 for the whole dataset.

	1st m	2nd m	10th m	20th m	30th m	40th m	50th m	100th m
IC1	0.07	0.15	0.48	0.71	0.85	0.93	0.97	1.00

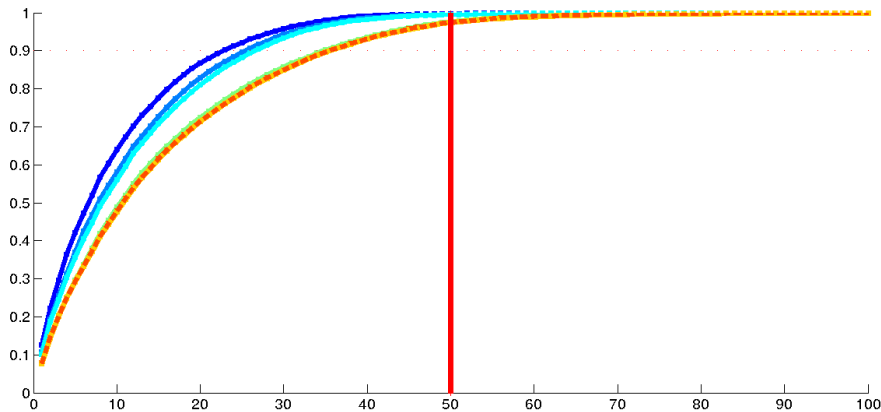


Figure 6.11: **Real dataset RD1000.** Proportion of cumulative explained variance of K-PCA as a function of the number of dimensions (in abscissa) and considering varying number of subjects. The dark blue curve was made using 100 subjects, the blue 200, the light blue 300, the green curve 500 subjects, the yellow one 800, very close to the dotted orange one which was made using 1000 subjects.

modes of variation. The result is shown in Figure 6.12. Compared to the smaller dataset RD50 (Figure 6.8), we can observe that the centroid (in the middle) is smoother as well as the shootings. For the first mode, we observe an enlargement of the hippocampus and a curvature of the tail. The second mode seems to correspond to an increase of the length and a slight modification of the shape of the hippocampal head.

Finally, we computed the approximated distance matrix. Its histogram is shown in Figure 6.13. Interestingly, as for RD50, all subjects have a relatively large mini-

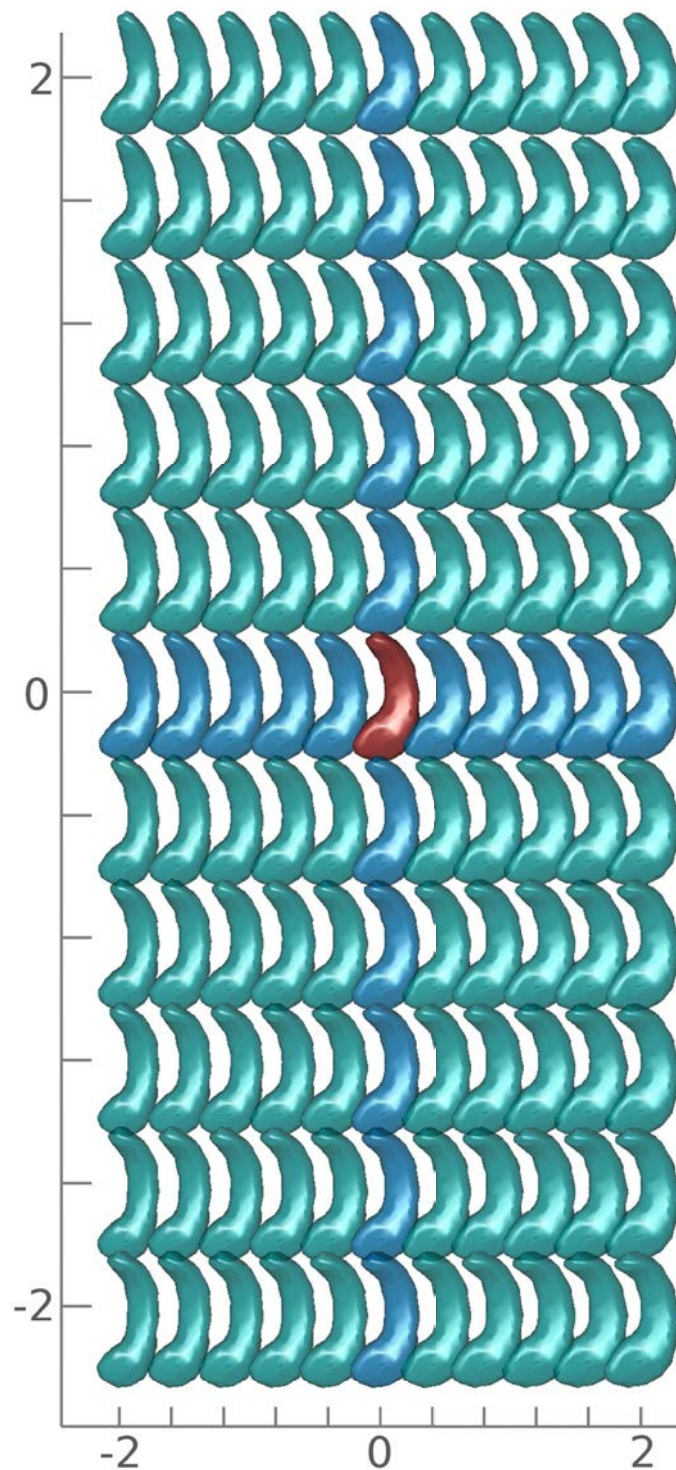


Figure 6.12: **Real dataset RD1000.** Grid of the 2D space generated by the 2 first components of the PCA computed from IC1 for the 1000 subjects of the database.

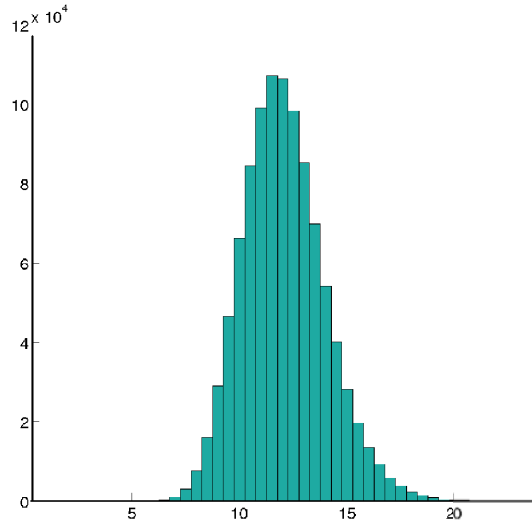


Figure 6.13: **Real dataset RD1000.** Histogram of the approximated distances of the large database from the computed centroid.

imum pairwise distance (about 6 for a maximum value around 20). This corresponds to the intuition that, in a space of high dimension, all subjects are relatively far from each other.

6.3.2 Prediction of IHI using shape analysis

We now apply our approach to predict incomplete hippocampal inversions (IHI) from hippocampal shape parameters. Specifically, we predict the visual IHI score, which corresponds to the sum of the individual criteria as defined in section 4.3 page 93. We studied whether it is possible to predict the IHI score using statistical shape analysis on the RD1000 dataset composed of 1000 healthy subjects (left hippocampus). We chose only 1000 subjects in order to include only subjects with good segmentation quality (i.e. a quality control ≥ 3) as previously explained in

section 4.4 page 106. For this study, we did not use the segmentations with a quality control = 2.5 because the main difference between quality control 2.5 and 3 is that the 2.5 group has a missing part on the hippocampus head which could bias the shape analysis.

The eigenvectors, computed in section 6.3.1, from the centroid IC1, are the independent variables we will use to predict the IHI scores. As we saw in the previous section (section 6.3.1 Table 6.9), 40 eigenvectors are enough to explain 93% of the total anatomical variability of the population. We use the centred and normalized principal eigenvectors $X_{1,i}, \dots, X_{40,i}$ computed from the RD1000 database with $i \in \{1, \dots, 1000\}$ to predict the IHI score Y . We simply used a multiple linear regression model (Hastie et al., 2009) which is written as $f(X) = \beta_0 + \sum_{i=1}^{40} X_i \beta_i$ where $\beta_0, \beta_1, \dots, \beta_{40}$ are the regression coefficients to estimate. The standard method to estimate the regression coefficients is the least squares estimation method in which the coefficients β_i minimize the residual sum of squares $RSS(\beta) = \sum_{j=1}^N (y_j - \beta_0 - \sum_{i=1}^p x_{ji} \beta_i)^2$, which leads to the estimated $\hat{\beta}$ (with matrix notations) $\hat{\beta} = (X^T X)^{-1} X^T Y$. For each number of dimensions $p \in \{1, \dots, 40\}$ we validated the quality of the computed model with the adjusted coefficient of determination R_{adj}^2 , which expresses the part of explained variance of the model with respect to the total variance:

$$R_{adj}^2 = 1 - \frac{SSE/(N-p)}{SST/(N-1)} \quad (6.3)$$

with $SSE = \sum_i^N (y_i - (X_{1\dots p,i}^T \hat{\beta}))^2$ the residual variance due to the model and $SST = \sum_{i=1}^N (y_i - \bar{Y})^2$ the total variance of the model. The R_{adj}^2 coefficient, unlike R^2 , takes into account the number of variables and therefore does not increase with the number

of variables. One can note that R is the coefficient of correlation of Pearson. We then tested the significance of each model by computing the F statistic

$$F = \frac{R^2/p}{(1 - R^2)/(N - p - 1)} \quad (6.4)$$

which follows a F-distribution with $(p, n - p - 1)$ degrees of freedom. So for each number of variables (i.e. dimensions of the PCA space) we computed the adjusted coefficient of determination to evaluate the model and the p -value to evaluate the significance of the model.

Then we used the k -fold cross validation method which consists in using $1000 - k$ subjects to predict the k remaining ones. To quantify the prediction of the model, we used the traditional mean square error $MSE = SSE/N$ which corresponds to the unexplained residual variance. For each model, we computed 10,000 k -fold cross validation and displayed the mean and the standard deviation of MSE corresponding to the model.

Results are given at Figure 6.14, and display the coefficient of determination of each model. The cross validation is only computed on models with a coefficient of correlation higher than 0.5, so models using at least 20 dimensions. For the k -fold cross validation, we chose $k = 100$ which represents 10% of the total population. Figure 6.14D presents results of cross validation; for each model computed from 20 to 40 dimensions we computed the mean of the 10,000 MSE of the 100-fold and its standard deviation. To have a point of comparison, we also computed the MSE between the IHI scores and random values which follow a normal distribution with the same mean and standard deviation as the IHI scores (red cross on the Figure). The MSE of the cross validation are similar to the MSE of the training set. This

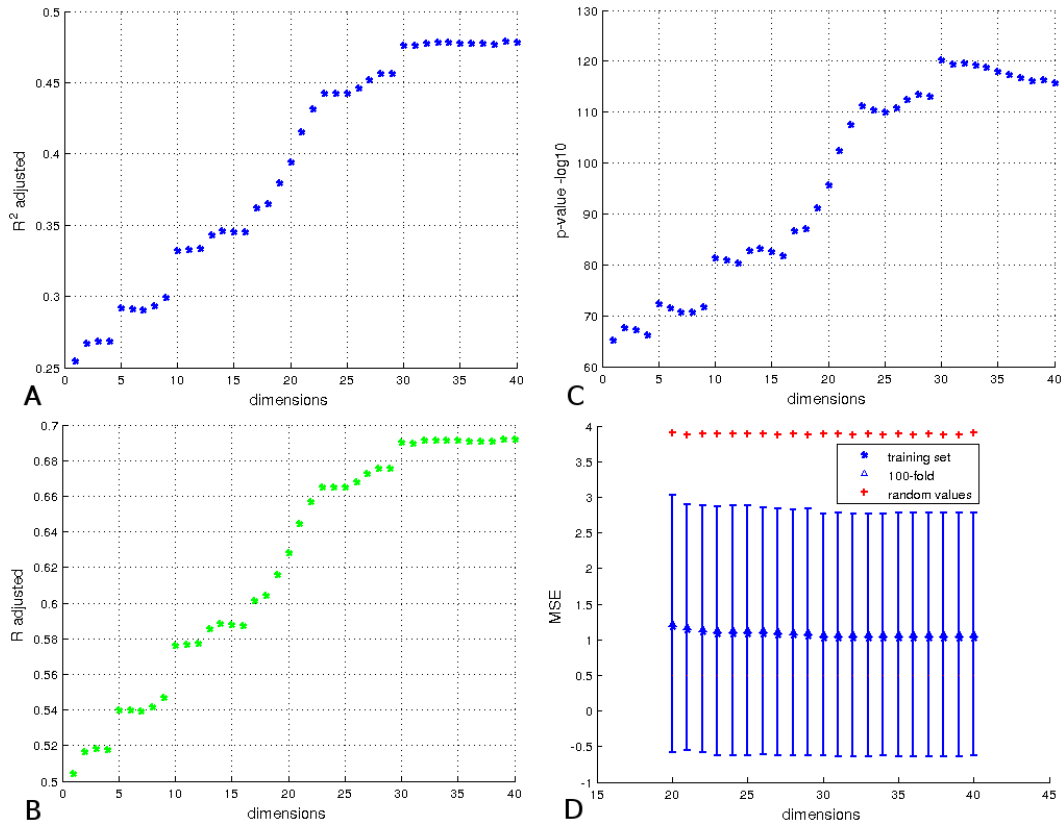


Figure 6.14: Results for prediction of IHI scores. A: Values of the adjusted coefficient of determination using from 1 to 40 eigenvectors resulting from the PCA. B: The coefficient correlation corresponding to the coefficient of determination of A. C: The p -values in $-\log_{10}$ of the corresponding coefficient of determination. D: Cross validation of the models using 20 to 40 dimensions by 100-fold. The red cross indicates the MSE of the model predicted using random values, and the errorbar corresponds to the standard deviation of MSE computed from 10,000 cross validations for each model, the triangle corresponds to the average MSE .

results show that using the first 30 to 40 principal components of initial momentum vectors computed from a centroid of the population, it is possible to predict the IHI score with a correlation of 69%.

6.4 Discussion and conclusion

In this chapter, we proposed a method for template-based shape analysis using diffeomorphic centroids. This approach leads to a reasonable computation time making it applicable to large datasets. It was thoroughly evaluated on different datasets including a large population of 1000 subjects.

The results demonstrate that the method adequately captures the variability of the population of hippocampal shapes with a reasonable number of dimensions. In particular, PCA showed that the large population of left hippocampi of young healthy subjects can be explained, for the metric we used, by a relatively small number of variables (around 50-60). Moreover, when a large enough number of subjects was considered, the number of dimensions was independent of the number of subjects.

The comparisons performed on the two small datasets show that the different centroids or variational templates lead to very similar results. This can be explained by the fact that in all cases the analysis was performed on the tangent space of the template, which correctly approximates the population in the shape space. Moreover, we showed that the different centres are equally well centred in the population.

While all templates (centroids or variational templates) yield comparable results, they have different computation times. IC1 and PW centroids are the fastest approaches and can save between 70 and 90% of computation time over the variational template. Thus, for the study of hippocampal shape, IC1 or PW algorithms seem to be more adapted than IC2 or the variational template estimation. However, it is not clear whether the same conclusion would hold for more complex sets of anatomical

structures, such as an exhaustive description of cortical sulci (Auzias et al., 2011). Besides, one should note that, unlike with the variational template estimation, centroid computations do not directly provide transformations between the centroid and the population which must be computed afterwards to obtain momentum vectors. This requires N more matchings, which doubles the computation time. Even with this additional step, centroid-based shape analysis stills leads to a competitive computation time (about 26 hours for the complete procedure on the large dataset of 1000 subjects).

In this study, we also applied this centroid computation to a template based shape analysis, and used the resulting shape parameters (best eigenvectors) for the prediction of IHI scores. We showed that using the first 30 to 40 eigenvectors of the PCA is enough to predict with a correlation coefficient of 69% of the variation of the IHI score. This is an interesting result which means that the template-based shape analysis we used provides consistent results: by using hippocampal shapes we are able to predict a part of a particular anatomical variation of the hippocampus.

In future work, this approach could be compared to other template estimation methods such as for example Durrleman et al. (2008a) Ma et al. (2008) Vaillant et al. (2004). We could also study the impact of the choice of parameters on the number of dimensions needed to describe the variability population (in this study the parameters were selected to optimize the matchings). Finally we can note that this template-based shape analysis could be easily extended to other data types such as images or curves.

CHAPTER 7



SHAPE ANALYSIS APPLIED TO THE ALZHEIMER'S DISEASE

This chapter is an excerpt from an article which has been submitted to *Computer Methods in Biomechanics and Biomedical Engineering: Imaging and Visualization* journal, and a first version of this study has been presented at the *Medical Image Understanding and Analysis 2014* conference in London and published as a short conference paper ([Cury et al., 2014a](#)). It follows chapters 5 and 6 as it makes use of the methodology for centroid computation and shape analysis presented in these chapters. Here this set of techniques is applied to the analysis of a dataset from the

Alzheimer's Disease Neuroimaging Initiative (ADNI) database, which is composed of two groups (control group and Alzheimer's disease group) and provides clinical information together with the anatomy. Consequently, the statistical analysis part is focused here on group variability comparison and prediction of clinical variables, unlike what was done in chapter 6 with the IMAGEN database.

7.1 Dataset and experiments

The method was applied to the analysis of hippocampal shapes of 134 patients with Alzheimer's Disease (AD, with age = 75.8 ± 7.3 years, 50% male, Mini Mental State Examination (MMSE) = 23 in average) and 160 controls (CN, with age = 76.0 ± 5.4 years, 47% male, MMSE=29 in average) ($N = 294$ in total) from the Alzheimer's Disease Neuroimaging Initiative (ADNI) database¹. Left hippocampi were segmented with the SACHA software (Chupin et al., 2009) from 3D T1 weighted MRI. Then the meshes were computed using the BrainVisa² software. They are composed of 800 vertices on average.

For this dataset, we first analysed the variability of both patients and control groups using Principal Component Analysis. Then, for the AD group, we assessed the aptitude of our approach to predict clinical parameters. Specifically, we studied

1. (adni.loni.usc.edu). The Principal Investigator of this initiative is Michael W. Weiner, MD, VA Medical Center and University of California - San Francisco. The investigators within the ADNI contributed to the design and implementation of ADNI and/or provided data but did not participate in analysis or writing of this report. A complete listing of ADNI investigators can be found at: adni.loni.usc.edu/wp-content/uploads/how_to_apply/ADNI_Acknowledgement_List.pdf. Data collection and sharing for this project was funded by the Alzheimer's Disease Neuroimaging Initiative (ADNI) (National Institutes of Health Grant U01 AG024904) and DOD ADNI (Department of Defense award number W81XWH-12-2-0012).

2. <http://www.brainvisa.info>

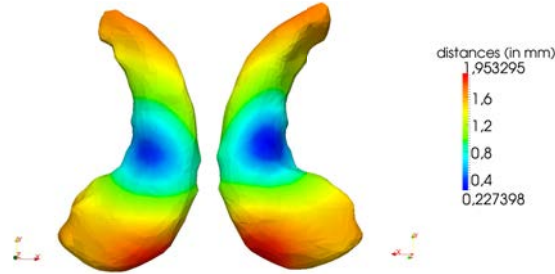


Figure 7.1: Distances between $IC(CN)$ and the deformation of $IC(CN)$ onto $IC(AD)$. On the left, the hippocampus is viewed from below.

the Mini Mental State Examination (MMSE) which is a global indicator of the severity of cognitive impairment, and the ADNI-MEM score (Crane et al., 2012) which is a composite score reflecting the performance of the subjects on memory tasks.

We hypothesise that hippocampal shape predicts the ADNI-MEM score, reflecting the central role of the hippocampus in memory performance. On the other hand, we hypothesise that it will not predict the MMSE which is a global indicator.

7.2 Results: analysis of variability

We computed a centroid for each of the two populations (AD and CN) using Algorithm 1 page 130. The two centroids are denoted $IC(AD)$ and $IC(CN)$. Computation times were 2.4 hours for $IC(AD)$ and 3.6 hours for $IC(CN)$. To assess whether the centroids are close to the center of the respective populations, we computed the ratio $R = \frac{\|\frac{1}{N} \sum_{i=1}^N v_0(S_i)\|_V}{\frac{1}{N} \sum_{i=1}^N \|v_0(S_i)\|_V}$ between the mean of the norms of initial vector fields from the centroid to the population and the norm of the mean of initial vector fields. Both ratios are 0.25, which means that both centroids are correctly centred

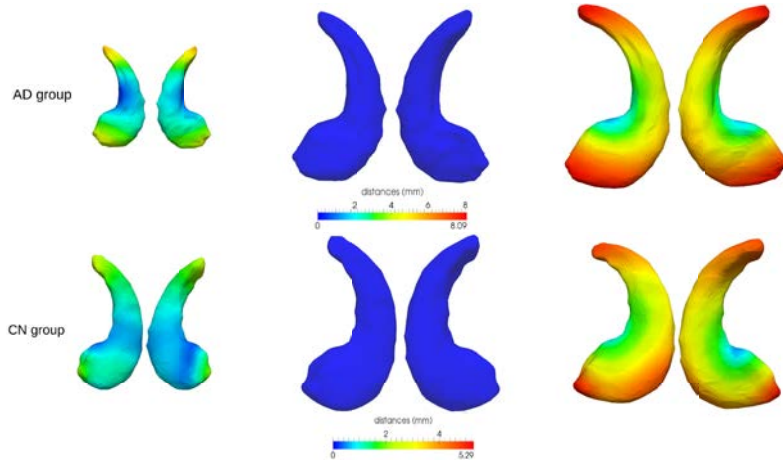


Figure 7.2: First mode of deformation of the AD group (top) and of the CN group (bottom). For each row, the centroid is in the center (in blue), on the right its deformation at $+2\sigma_1\mathbf{m}^1$, and at $-2\sigma_1\mathbf{m}^1$ on the left. The colormap indicates the displacement of each vertex between the corresponding centroid and its deformation.

even though they are not exactly at the Fréchet mean (which would correspond to $R = 0$). To visualise differences between $IC(CN)$ and $IC(AD)$, we computed distances between vertices of $IC(CN)$ and the deformation of $IC(CN)$ onto $IC(AD)$ (figure 7.1).

We then analysed the variability of the AD and the CN populations using PCA. Figure 7.2 shows, for each group, the principal mode of variation. This figure is obtained by geodesic shooting from each centroid in the first principal direction with a magnitude of $\pm 2\sigma_1$, with σ_1 the standard deviation of the first mode of variation. One can note that, while the templates of the two groups are different, the variabilities of both groups share similarities. Nevertheless, there seems to be less variability in the medial part of the body for the CN group.

In order to visualize the localization of $IC(CN)$ and $IC(AD)$ and the corre-

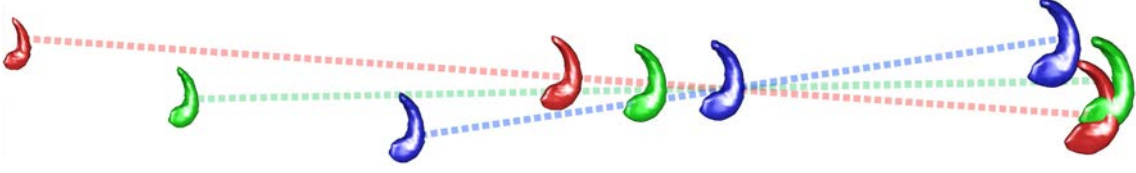


Figure 7.3: Two principal axes of the whole population (in green), the length of each axis is proportional to its standard deviation. In blue, the projections of $IC(CN)$ and projections of its deformations at $\pm 2\sigma$ in the direction of its first mode of variation. In red, for the AD group.

sponding first modes within the whole population, we computed a centroid of the whole population and performed a PCA. We then projected $IC(CN)$ and $IC(AD)$ and their corresponding $\pm 2\sigma_1 \mathbf{m}^1$ onto the 2D space spanned by the first two principal components of the whole dataset. We can observe (figure 7.3) that $IC(CN)$ is on the right of the global centroid, and $IC(AD)$ is on the other side, and the 3 principal modes of variation have different directions. One can observe that for the AD and the CN group, the two shapes corresponding to the $+2\sigma_1 \mathbf{m}^1$ deformation (on the right of the figure 7.3) are close i.e. similar to each others. This observation can also be note on the figure 7.2, which shows that the deformation in the direction $-2\sigma_1$ for the AD group is very different than the one of the CN group and the deformation in the direction $+2\sigma_1$ for the AD group is similar to the one of the CN group.

We then studied the variance associated to the different dimensions. In total, the AD group have more variance than the CN group: $\sum_{i=1}^{N_{AD}} \lambda_i^{AD} = 233$ and $\sum_{i=1}^{N_{CN}} \lambda_i^{CN} = 171$. The first two components of the AD group have a variance of respectively 51.4 and 21.2, while the two first components of the CN group have a

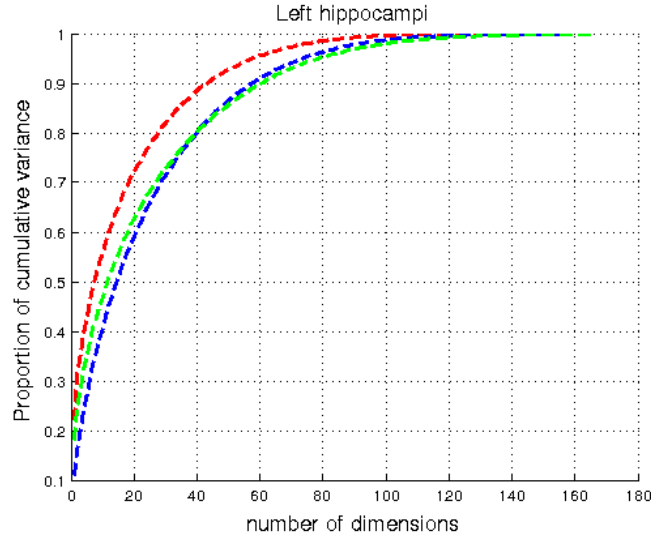


Figure 7.4: In red, the proportion of cumulative variance of the AD group, in blue of the CN group and in green, of the whole population.

smaller variance of respectively 19.0 and 8.3. We also studied the proportion of cumulative variance CEV_k explained for each number of dimensions k . In Figure 7.4, we can see that the AD group needs less dimensions (or principal components), around 40 dimensions, to explain 90% of its total variance than the CN group (requiring around 60 dimensions). To make sure that this difference is not due to the larger number of subjects in the CN group, we also performed the same experiment with the same number of subjects (134) in each group, and obtained similar results.

Figure 7.5 shows these two first modes of variations in blue for the CN group and in red for the AD group computed by geodesic shooting in the directions $(k_1 \times \mathbf{m}^1; k_2 \times \mathbf{m}^2)$ with $k_1 \in [-2\sigma_1; +2\sigma_1]$ and $k_2 \in [-2\sigma_2; +2\sigma_2]$, with \mathbf{m}^1 and \mathbf{m}^2 the two first modes of variations of the population, and σ_i the standard deviation of the corresponding mode \mathbf{m}^i . We can see that for the two groups, the first mode

mainly captures the volume effectn which effect is clearly (and expected to be) more important for the AD group, and also captures the curvature of the hippocampus tail. The second axis of the AD group captures the atrophy of the hippocampus body and head.

7.3 Results: prediction of clinical variables

For the AD group we tested the ability of different models computed using different number of variables to predict clinical variables (MMSE and ADNI-MEM).

Multiple linear regression From the space computed via the PCA, by using the z-scored p principal eigenvectors $X_{1,i}, \dots, X_{p,i}$ with $i \in \{1, \dots, N\}$ of the N subjects, we can use multiple linear regression to predict a biological or clinical factor Y . The multiple linear regression model is written as $f(X) = \beta_0 + \sum_{i=1}^p X_i \beta_i$ where $\beta_0, \beta_1, \dots, \beta_p$ are the regression coefficients. The standard method to estimate the regression coefficients is the least squares estimation method in which the coefficients β_i minimize the residual sum of squares $RSS(\beta) = \sum_{j=1}^N (y_j - \beta_0 - \sum_{i=1}^p x_{ji} \beta_i)^2$, which leads to the estimated $\hat{\beta}$ (with matrix notations) $\hat{\beta} = (X^T X)^{-1} X^T Y$ (Hastie et al., 2009). For each dimension p we validated the quality of the computed model with the adjusted coefficient of determination R_{adj}^2 , which expresses the part of explained variance of the model with respect to the total variance:

$$R_{adj}^2 = 1 - \frac{SSE/(N-p)}{SST/(N-1)} \quad (7.1)$$

with $SSE = \sum_i^N (y_i - (X_{1\dots p,i}^T \hat{\beta}))^2$ and $SST = \sum_{i=1}^N (y_i - \bar{Y})^2$. The R_{adj}^2 coefficient, unlike the R^2 , takes into account the number of variables and therefore does not



Figure 7.5: Geodesic shootings in the directions of $(k_1 \times \mathbf{m}^1; k_2 \times \mathbf{m}^2)$ with $k_1 \in [-2\sigma_1; +2\sigma_1]$ and $k_2 \in [-2\sigma_2; +2\sigma_2]$ with \mathbf{m}^1 and \mathbf{m}^2 the two first modes of variations for the AD group (in red) and the CN group (in blues). Principal axis $(k_1 \times \mathbf{m}^1; 0)$ and $(0; k_2 \times \mathbf{m}^2)$ are in yellow for the AD group and in light blue for the CN group.

increase with the number of variables. We then tested the significance of each model by computing the F statistic

$$F = \frac{R^2/p}{(1 - R^2)/(N - p - 1)} \quad (7.2)$$

which follows a F-distribution with $(p, n - p - 1)$ degrees of freedom. So for each number of variables (i.e. dimensions) we computed the coefficient of determination to evaluate the model and the p -value to evaluate the significance of the model. Then we used a leave-one-out cross validation which consists in computing N models with $N - 1$ observations to predict the remaining one. To quantify the prediction of the model, we computed the mean square error $MSE = SSE/N$ which corresponds to the unexplained residual variance.

The variables of the models are the principal modes of variation i.e. principal components of the PCA computed from the PCA. The response Y is the response to the ADNI-MEM test or to the MMSE test. We saw in the previous section that the AD group can express 90% of its total variability by using only 40 dimensions, thus we studied models with maximum 50 principal modes of variation.

Figure 7.6 shows, for the hippocampi of the AD group, the values of R_{adj}^2 coefficient computed from the models computed with the k first modes of variations, then the corresponding p -values are displayed. We cross validated the models with the best R_{adj}^2 coefficients and the best p -values with the lower number of dimensions. Thus, for the cross validation step we assessed models from 29 dimensions to 40 dimensions which seems to be the more interesting. For these model, $R_{adj}^2 = 0.25$ on average, and the p -values are $1.2e-3$ on average. Results of cross validation using leave-one-out (LOOCV) are assessed using the MSE score (right panel of

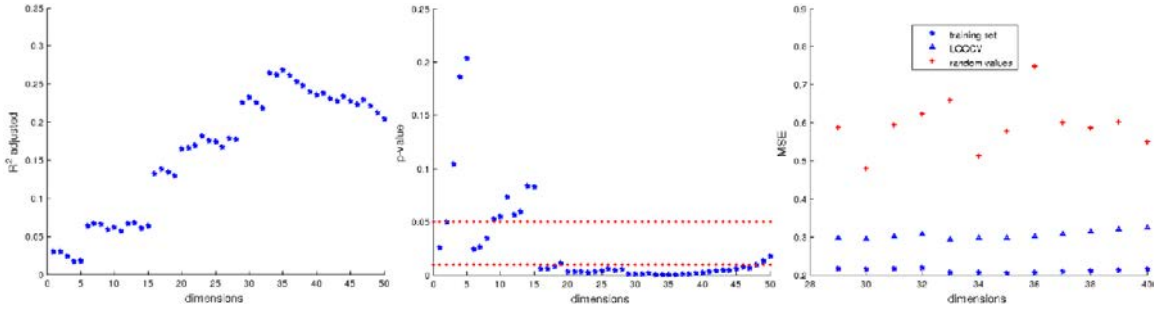


Figure 7.6: Multiple linear regression on principal components for the Y response ADNI MEM, and variables are the principal modes of variations. On left panels, R_{adj}^2 coefficients regarding to the number of dimensions (i.e. variables) of the model. On middle panels, the corresponding p -values of the models with dotted red lines representing the thresholds 0.05 and 0.01. On right panels, the different MSE computed from some model previously selected using the two previous panels in which the corresponding models are highlighted in green.

the Figure 7.6). MSE scores of the predicted values from the cross validation step are compared to the MSE of the model, and to a random prediction distributed normally with mean \bar{Y} and variance σ_Y^2 .

None of the models (even those computed using more than 50 variables) was able to predict the response to the MMSE test, the maximum value for the R_{adj}^2 coefficient was 0.11, and the p -values were all higher than 0.1.

7.4 Conclusion

In this chapter, we proposed a template-based shape analysis approach for group comparison and the prediction of clinical variables, in the LDDMM framework, and applied it to the study of a database of Alzheimer and controls from the ADNI database. We computed a centroid of the whole population using the diffeomorphic

iterative centroid method, as well as centroids for the AD and CN groups. Analysis of variability was then based on a PCA on the initial momentum vectors from the centroid to the subjects. The comparison of the resulting geodesic shooting surfaces in the direction of the principal modes of variation of the AD group and of the CN group shows that for each group the volume is mainly captured in this principal mode, and these two groups produce really different shapes. Furthermore, the projection of the templates of the CN group and the AD group onto the two principal modes of variation of the whole population show that they are located on the main axis of variability. The analysis of the number of dimensions given by the PCA shows that, even if the AD group is more variable than the CN group, the AD group is explained by fewer dimensions than the CN group. Our experiments also showed that the approach can be used to predict clinical variables from hippocampal shape. Specifically, we were able to predict memory performances in AD patients, which is consistent with the central role played by the hippocampus in memory processes.

CHAPTER 8

CONCLUSION AND DISCUSSION

The topic of this thesis was the analysis of the anatomical variability of the hippocampus on large databases. The objectives were two-fold. First, we aimed to design methods for statistical shape analysis of the hippocampus, applicable to large number of subjects. Moreover, we aimed to study a remarkable anatomical variant of the hippocampus. This anatomical variant is the Incomplete Hippocampal Inversion (IHI) and could be of developmental origin. Until now, this variant has been mostly studied in patients with epilepsy. It was also known to be present in

healthy subjects but its prevalence and characteristics were unclear.

We designed robust visual criteria to characterize and study IHI, that are applicable to large series of subjects. On the other hand, we developed fast approaches for template-based shape analysis based on the mathematical frameworks of currents and of Large Diffeomorphic Deformations Metric Mapping. In particular, we introduced diffeomorphic iterative centroid methods to compute a template of the population. This approach were then introduced in statistical analyses. In particular, we combined it with principal component analysis on the initial momentum vectors of the deformations from the template to the subjects. We showed that it allowed to summarize the variability of the population with a reasonable number of dimensions. Further, we used multiple linear regression to predict IHI scores in normal subjects. We also showed that this approach can be used to predict clinical variables, such as memory scores, in patients with Alzheimer's disease.

* *
*

For evaluation of IHI, we proposed and applied 5 criteria which are reproducible. We demonstrated that IHI are not a rare anatomical variant and they are much more frequent in the left hemisphere. Specifically, they are present in around 17% of left-side hippocampus and in around 6.5% of right-side hippocampus in the healthy and young population. We also introduced an IHI score ranging from 0 to 10 to give a degree of IHI for each hippocampus. Indeed, we showed that there is an anatomical continuum between hippocampi with incomplete inversion and normal hippocampi. Using this IHI score and the hippocampi with and without obvious IHI,

we determined a threshold to be able to classify the hippocampi into two groups (IHI and non-IHI). Therefore an IHI score < 4 indicates that the hippocampus is normal otherwise it very probably present an IHI.

We proposed a pipeline for template-based shape analysis of large databases. The diffeomorphic iterative centroid method we proposed allows computing a centroid of the population. We showed that this centroid is always close to the centre of the population, even though it depends on the subject ordering. We also saw that using an iterative centroid rather than a more complex template estimation has no impact on the subsequent template-based analysis, in the case of hippocampi. We firstly computed the template of the population by using the diffeomorphic iterative centroid method proposed in Chapter 5, then we computed the initial momentum vectors from the template to the population and then we used a PCA in the tangent space at the level of the template. This template-based shape analysis was applied to the study of 1000 left hippocampi (with good segmentation quality) from the IMAGEN database. We showed that the anatomical variability of these 1000 hippocampi can be captured by a space of reasonable dimension (around 50 dimensions). We showed that using the first 30-40 dimensions we were able to predict the IHI score, with a correlation coefficient of 0.69. We also used this template-based shape analysis on 298 subjects of the ADNI database. Results showed that the method is able to predict a memory score with the first 30-40 dimensions of the anatomical variability of the AD population.

To conclude, we developed criteria to evaluate IHI and applied them to study their prevalence in healthy subjects. The statistical template-based shape analysis

we proposed using the diffeomorphic iterative centroid method is able capture the anatomical variability of hippocampi with few variables and predict some biological or clinical parameters.

* *
*

Various questions regarding IHI remain to be answered. First, it is not clear whether this atypical anatomical pattern is confined to the hippocampus. It is already clear that IHI are associated with other atypical features in the temporal lobe: characteristics of the collateral sulcus and the occipito temporal sulcus are part the criterion and co-occur with hippocampus-specific features. Nevertheless, the extent of these atypical patterns in other parts of and outside of the temporal lobe remain to be studied. An interesting possibility is to analyse the IHI score together with sulcal measurements. Such a study is currently undergoing.

Also, the factors (genetic, environmental) that influence the development of IHI are currently unknown. It would be also particularly interesting to analyse the relationship of IHI with genetics variables. Indeed, some genes are known to be linked with hippocampal volume as the gene APOE4 (O'Dwyer et al., 2012) and variants at positions 12q14 and 12q24 (Bis et al., 2012). Besides, various genes are involved in diseases affecting the hippocampus, including CLU, BIN1, APOE4 (Braae et al., 2014; Michaelson, 2014). More specifically, a study showed frequent IHI in subjects with micro-deletions at 22q11.2 (Bassett et al., 2014). Since we characterized IHI on all subjects of the IMAGEN database, the study of correlations

between IHI and Single Nucleotide Polymorphisms appears as a natural perspective of our work.

There are also several methodological perspectives. First, it could be interesting to compare the diffeomorphic iterative centroid method to other template estimation methods such as those of [Vaillant et al. \(2004\)](#); [Glaunès & Joshi \(2006\)](#); [Durrleman et al. \(2008a, 2012\)](#); [Ma et al. \(2008\)](#). Furthermore, while the use of centroids in place of variational template estimation had no impact in our case that dealt with hippocampal shape, it would be interesting to study if this is also true with more complex structures or set of structures such as cortical sulci ([Auzias et al., 2011](#); [Durrleman et al., 2008b](#)) or white matter tracks ([Gori et al., 2013](#)). Finally, the diffeomorphic iterative centroid could also be used to initialize other template estimation methods.

LIST OF FIGURES

2.1	Dissection of the inferomedial part of the right hemisphere (a), and coronal section of a brain (b). From Duvernoy (2005)	25
2.2	The limbic system	26
2.3	Anatomy of the hippocampus. Left: general shape of the gyrus dentatus in an axial point of view. Right: the two cortical U-shaped lamina of the gyrus dentatus (GD on the figure) and the cornu Ammonis (CA). A: head, B: body, C: tail, and right: the general shape of the hippocampus. Drawings are from Duvernoy (2005)	27
2.4	Anatomy of the hippocampus. Schema of the internal organisation of the hippocampus	29
2.5	Schematic diagram of the temporal lobe in the coronal plane during the development of the hippocampus. D: gyrus dentatus, C: cornu Ammonis, S: subiculum, P: parahippocampal gyrus. Drawing from Baker & Barkovich (1992)	30
2.6	13 GW. (a) Photography from Kier et al. (1995) in sagittal plane of the medial brain surface of a 13 GW foetus. The frontal lobe is on the left side of the photography and the temporal lobe on the bottom part and the hippocampus is highlighted in green. The corpus callosum is not yet formed. Large arrowheads, hippocampal sulcus; small arrowheads, the inner limbic arch of the hippocampal formation; OT, olfactory tract. The distance between two graduations is 1 mm. (b) Coronal T1-weighted spoiled gradient-echo MR image (45/8/2; 45° flip angle) of an intact 13 GW foetus from Kier et al. (1997) . The neocortical parahippocampal gyrus region (P) is small, (T) is the temporal horn. The white vertical line measures 10 mm.	32

2.7 16 GW. (a) Photography from [Kier et al. \(1995\)](#) in sagittal plane of the medial brain surface of a 16 GW foetus. Large arrowheads, hippocampal sulcus; small arrowheads, the inner limbic arch of the hippocampal formation; CC, corpus callosum; F, fornix; OT, olfactory tract. The distance between two graduations is 1 mm. (b) Coronal T1-weighted spoiled gradient-echo MR image (45/8/2; 45° flip angle) of intact 13 GW old foetus from [Kier et al. \(1997\)](#). The neocortical parahippocampal gyrus region (P) is small. The white vertical line measures 10 mm. (c) coronal histological section (Nissl, original magnification $\times 24$ from [Kier et al. \(1997\)](#)), the CA1 (1), CA2 (2), and CA3 (3) fields of the cornu Ammonis are arranged linearly. The dentate gyrus (small arrowheads) has a tight U-shaped configuration around the CA4 (4) field of the cornu Ammonis. The very thin molecular stratum (M) of the dentate gyrus is separated from the larger molecular stratum of the cornu Ammonis by the very wide hippocampal sulcus (large arrowheads). 33

2.8 (A) acetylcholinesterase histochemistry of a 25 GW. (B) a T1-weighted MRI from a 25 GW, and (C), T1-weighted MRI from a full term newborn. TH: Thalamus. Images are from [Radoš et al. \(2006\)](#). 34

2.9 Coronal point of view of hippocampi, the 3 images are from the same subject, the top image shows the heads of the hippocampi, the middle image shows the bodies of hippocampi and the bottom one, the tails. The left hippocampus framed in red presents a rounded shape, a medial positioning and a deep colateral sulcus which are typical criteria for an IHI. 36

2.10 Two visualizations of hippocampus of a same subject from the IRMA7 database. (a) Magnetic Resonance Images with a T1-weighted acquisition and (b) T2-weighted acquisition. Views are (from left to right) axial, coronal and sagittal. 39

2.11 Visualization of the hippocampi of a same subject of the IRMA7 database in Figure 2.10. The volumetric image have been computed by Marrakchi et al. (submitted paper) from different T2-weighted sequence in 7T MRI, by registering the different acquisition using the 3T MRI. 41

2.12 Hippocrates 46

3.1 Three similar shapes. 55

- 4.1 Figure from the third edition of The Human Hippocampus book of Duvernoy [Duvernoy \(2005\)](#). Figure A: Development of the gyrus dentatus (dotted area) and the Cornus Ammonis (hatched area). Figure B: Their definitive disposition. Arrows indicate the hippocampal sulcus (superficial part). 1, Cornus Ammonis; 2, gyrus dentatis; 3, hippocampal sulcus (deep or vestigial part); 4, fimbria; 5, prosubiculum; 6, subiculum proper; 7, presubiculum; 8, parasubiculum; 9, entorhinal oarea; 10, parahippocampal gyrus; 11, collateral sulcus; 12, collateral eminence; 13, temporal (inferior) horn of the lateral ventricle; 14, tail of caudate nucleus; 15, stria terminalis; 16, choroid fissure and choroid plexuses; 17, lateral geniculate body; 18, lateral part of the transverse fissure; 19, ambient cistern; 20, mesencephalon; 21, pons; 22, tentorium cerebelli. . . . 86
- 4.2 coronal view of a T1-weighted MRI in the MNI space from a subject of the database IMAGEN. On the right (left hippocampus) an IHI, and on the left a standard hippocampus 89
- 4.3 Criterion $C1$: roundness and verticality of the hippocampus. For roundness, the hippocampus is considered flat when $C1_a \gg C1_b$, round when $C1_a \simeq C1_b$, and ovoid when $C1_a \ll C1_b$. The verticality of the hippocampus is determined by the verticality of the segment $C1_a$ 94
- 4.4 Examples for the evaluation of the $C1$ criterion. Which grades for these 7 hippocampi from (a) to (g)? Results are detailed in Table 4.3 and in Figure 4.5. 95
- 4.5 Results of the Figure 4.4 Segments are here only for helping the reader, they are not displayed on the MRI. 96
- 4.6 Figure from [Kim et al. \(2008\)](#). The red sulcus is the collateral sulcus (CS), the blue one is the rihnal sulcus (RS) and the green one, the occipitotemporal sulcus (OTC). Upper panel: basal view of the 3D MRI rendering. Middle panel: basal view of extracted sulci. Lower panel: three coronal slices of T1-weighted MRI at the level of hippocampal head, body and tail. The columns represent the four different patterns. 98
- 4.7 criterion $C2$: verticality and depth of the collateral sulcus. The segment a indicates the collateral sulcus, and b the lateral part of the hippocampus. If a do not cross b and stays medial to b , the grade will be between 0 and 1 otherwise between 1 and 2. 99

4.8	Examples for the criterion C_2 . The segments are displayed to help the reader, but during the evaluation no segments appear on the MRI. (a) has a grade of 0 since $C2_a$ is horizontal and does not cross $C2_b$. (b) has a grade of 0.5 since $C2_a$ is oblique, even if the occipito-temporal sulcus seems closer to the temporal horn. (c) has a grade of 1, $C2_a$ crosses horizontally $C2_b$. (d) has a grade of 1.5 since $C2_a$ is oblique and cross $C2_b$. (e) and (f) have a grade of 2, they are vertical, and cross or exceed $C2_b$	100
4.9	Criterion $C3$. Medial positioning of the hippocampus is estimated using the length of the part of the subiculum which is not covered by the gyrus dentatus (segment $C3_a$) relatively to the length of the ventral part of the hippocampus which is covered by the gyrus dentatus (segment $C3_b$).	101
4.10	Examples for the criterion C_3 . (a) corresponds to the case where $C3_a > C3_b$, (b) corresponds to the case where $C3_a = C3_b$ and the temporal horn is filled by the CSF, (c) the case where $C3_a$ is not visible	102
4.11	Examples for the criterion C_4	103
4.12	Criterion $C5$. If neither the CS nor the OTS superior parts (green dotted lines) exceed the level of the subiculum (red area), the grade is 0. Otherwise, the grade is either 1 (if the exceeding sulcus has an oblique orientation) or 2 (if the exceeding sulcus has a vertical orientation).	105
4.13	Examples for the criterion C_5	106
4.14	Java application for evaluation of IHI, quality control of MRI and quality control of MRI segmentations.	108
4.15	Histograms of the sums of individual criteria C_i for left hippocampi (a), right hippocampi (b) and the superposed histograms (c).	114
4.16	Histogram of the sum of grades of all individual criteria ($C1$ to $C5$) for left hippocampi (a), right hippocampi (b) and the superposed histograms (c).	115
5.1	Illustration of the method. Left image: red stars are subjects of the population, the yellow star is the final Centroid, and orange stars are iterations of the Centroid. Right image: Final Centroid with the hippocampus population from Data1 (red). See section 5.3.1 for more details about datasets.	129
5.2	Diagrams of the iterative processes which lead to the centroid computation. The tops of the diagrams represent the final centroid. The diagram on the left corresponds to the Iterative Centroid algorithms (IC1 and IC2). The diagram on the right corresponds to the pairwise algorithm (PW).	130

5.3	On the left, an Iterative Centroid of the dataset Data2 (see section 5.3.1 for more details about datasets) computed using the IC1 algorithm, and on the right the IC2 algorithm.	134
5.4	Top to bottom: meshes from Data1 (n=500), Data2 (n=95) and Real-Data (n=95)	137
5.5	A. First row: 3 initial subjects used for 3 different centroid computations with IC1 (mean distance between such centroids, in the space of currents, is 4.71) on RealData. Second row: the 3 centroids computed using the 3 subjects from the first row as initialization. B: Maps of the amplitude of the momentum vectors that map each centroid to another. Top and bottom views of the maps are displayed. One can note that the differences are small and local.	140
5.6	Estimated variational template from RealData. On the left, initialized via the standard initialization which is the whole population. On the right, estimated variational template initialized via a IC1 centroid	144
5.7	first row: Graphs of average W^* -distances between the IC1 at $x\%$ and the final one. The second row present the same results with IC2.	146
6.1	Left panel: coronal view of the MRI with the binary masks of hippocampi segmented by the SACHA software Chupin et al. (2009) , the right hippocampus is in green and the left one in pink. Right panel: 3D view of the hippocampus meshes.	155
6.2	Synthetic dataset SD. Projection of the 6 templates (3 centroids and 3 variational templates) on the 2D space of the synthetic data. “ X ” represent centroids, “ + ” represent templates. IC1 is in blue, IC2 in yellow and PW in magenta. The exact centre is represented by the red asterisk.	160
6.3	Synthetic dataset SD. Synthetic population in green, the exact center is in red. The two first components are marked in orange for the exact center, in blue for IC1, in yellow for IC2 and in magenta for PW.	162
6.4	Synthetic dataset SD. Scatter plots between the direct distance matrix and the 7 approximated distance matrices, computed from the exact center, IC1, IC2, PW and the corresponding variational templates of the synthetic dataset. The red line corresponds to the identity	163
6.5	Real dataset RD50. Projection of the 5 other templates (2 centroids and 3 variational templates) in the 2D space spanned by the two first modes of the PCA computed from the centroid IC1. “ x ” represent centroids, “ + ” represent templates. IC1 is in blue, IC2 in yellow and PW in magenta.	167

6.6	Real dataset RD50. Coordinates of the subjects in the 2D space spanned by the first two components of the PCAs computed from different templates. Panels A and B are superimpositions of the PCA from the 3 centroids (A) and from the 3 variational templates (B). There is one color per subject.	168
6.7	Real dataset RD50. Proportion of cumulative explained variance for PCAs computed from the 6 different templates, with respect to the number of dimensions. Curves are almost identical.	169
6.8	Real dataset RD50. Grid generated by the two first modes of variation of the PCA computed on the tangent space of IC1.	171
6.9	Real dataset RD50. Scatter plots between direct distance matrix and approximated distance matrices from the six templates. The red line corresponds to the identity.	172
6.10	Real dataset RD50. Scatter plot between the $aM(IC1)$ matrix and the 5 others approximated distance matrices. The red line corresponds to the identity.	172
6.11	Real dataset RD1000. Proportion of cumulative explained variance of K-PCA as a function of the number of dimensions (in abscissa) and considering varying number of subjects. The dark blue curve was made using 100 subjects, the blue 200, the light blue 300, the green curve 500 subjects, the yellow one 800, very close to the dotted orange one which was made using 1000 subjects.	174
6.12	Real dataset RD1000. Grid of the 2D space generated by the 2 first components of the PCA computed from IC1 for the 1000 subjects of the database.	175
6.13	Real dataset RD1000. Histogram of the approximated distances of the large database from the computed centroid.	176
6.14	Results for prediction of IHI scores. A: Values of the adjusted coefficient of determination using from 1 to 40 eigenvectors resulting from the PCA. B: the coefficient correlation corresponding to the coefficient of determination of A. C: The p -values in $-\log_{10}$ of the corresponding coefficient of determination. D: Cross validation of the models using 20 to 40 dimensions by 100-fold. The red cross indicates the MSE of the model predicted using random values, and the errorbar corresponds to the standard deviation of MSE computed from 10,000 cross validations for each model, the triangle corresponds to the average MSE	179
7.1	Distances between $IC(CN)$ and the deformation of $IC(CN)$ onto $IC(AD)$. On the left, the hippocampus is viewed from below.	185

7.2	First mode of deformation of the AD group (top) and of the CN group (bottom). For each row, the centroid is in the center (in blue), on the right its deformation at $+2\sigma_1\mathbf{m}^1$, and at $-2\sigma_1\mathbf{m}^1$ on the left. The colormap indicates the displacement of each vertex between the corresponding centroid and its deformation.	186
7.3	Two principal axes of the whole population (in green), the length of each axis is proportional to its standard deviation. In blue, the projections of $IC(CN)$ and projections of its deformations at $\pm 2\sigma$ in the direction of its first mode of variation. In red, for the AD group.	187
7.4	In red, the proportion of cumulative variance of the AD group, in blue of the CN group and in green, of the whole population.	188
7.5	Geodesic shootings in the directions of $(k_1 \times \mathbf{m}^1; k_2 \times \mathbf{m}^2)$ with $k_1 \in [-2\sigma_1; +2\sigma_1]$ and $k_2 \in [-2\sigma_2; +2\sigma_2]$ with \mathbf{m}^1 and \mathbf{m}^2 the two first modes of variations for the AD group (in red) and the CN group (in blues). Principal axis $(k_1 \times \mathbf{m}^1; 0)$ and $(0; k_2 \times \mathbf{m}^2)$ are in yellow for the AD group and in light blue for the CN group.	190
7.6	Multiple linear regression on principal components for the Y response ADNI MEM, and variables are the principal modes of variations. On left panels, R_{adj}^2 coefficients regarding to the number of dimensions (i.e. variables) of the model. On middle panels, the corresponding p -values of the models with dotted red lines representing the thresholds 0.05 and 0.01. On right panels, the different MSE computed from some model previously selected using the two previous panels in which the corresponding models are highlighted in green.	192

LIST OF TABLES

4.1	Characteristics of the studied population	92
4.2	Evaluation of the criterion $C1$, based on the verticality and roundness of the hippocampus.	95
4.3	Results of the $C1$ evaluation for hippocampus on Figure 4.4. "Hor" is for horizontal, "Obl" for oblique and "Ver" for vertical.	97
4.4	Evaluation of the criterion $C2$. Segments $C2_a$ and $C2_b$ are defined on reference to the figure 4.7 page 99.	99
4.5	Evaluation of the Criterion 3. Segments $C3_a$ and $C3_b$ are defined on Figure 4.9.	102
4.6	Results of Kappa test for the intra- and inter-observers reproducibility of the different criteria. The confident interval is at 95%	111
4.7	Percentage of IHI for left and right hippocampi with a confidence interval of 95%	111
4.8	Co-occurences of IHI for the left and right hippocampi, according to the global criterion $C0$. Confidence intervals (CI) are at 95%.	112
4.9	Frequency of IHI, according to the global criterion $C0$, for female and male populations, with a confidence interval at 95%	112
4.10	Repartition of grades for each individual criterion. We tested whether the repartition differs between left and right for each criterion (chi-square test).	113
4.11	For each individual criterion, its mean value on left and right and its frequency when ≥ 1	113
4.12	Frequency of IHI using the threshold IHI score <4	115

5.1	Distances between centroids computed with different subjects orderings, for each dataset and each of the 3 algorithms. The three first columns present the mean, standard deviation and the maximum of distances between all pairs of centroids computed with different orderings. The fourth column displays the mean of distances between each centroid algorithm and all subjects of the datasets. Distances are computed in the space of currents.	138
5.2	In columns, average distances between centroids computed using the different algorithms.	138
5.3	Ratio values for assessing the position of the representative centroid within the population, computed using Equation 5.8 (for each algorithm and for each dataset).	142
5.4	Distances between variational templates initialized via different IC1 ($T(IC1)$) for each datasets, and the distance between the variational template initialized via the standard initialization ($T(StdInit)$) and variational templates initialized via IC1.	143
5.5	Ratios R for variational templates ($T(IC1)$) and for the variational template with its usual initialization $T(StdInit)$, for each datasets.	143
5.6	Results of initialization of variational template estimation method by a IC1 at 40%	146
5.7	Computation time (in hours) for Iterative Centroids and for variational template estimation initialised by IC1 ($T(IC1)$), the standard initialization ($T(StdInit)$) and by IC1 at 40% ($T(IC1 \text{ at } 40\%)$). For $T(IC1)$, we give the complete time for the whole process i.e. the time for the IC1 computation plus the time for $T(IC1)$ computation itself.	147
6.1	Synthetic dataset SD. Computation times in minutes for the different templates of the synthetic dataset.	158
6.2	Synthetic dataset SD. Ratio R (equation 6.1) computed for the 3 centroids, and the 3 variational templates initialized via these centroids.	159
6.3	Synthetic dataset SD. Proportion of cumulative explained variance of PCA computed from different templates.	162
6.4	Synthetic dataset SD. Error e (equation 6.2) between the six different approximated distance matrices and the approximated distance matrix from the exact center (left column), and the direct distance matrix (right column).	164
6.5	Real dataset RD50. Computation times, in minutes.	165
6.6	Real dataset RD50. Ratio R (equation 6.1) computed for 3 centroids and 3 variational templates initialized via these centroids.	166

6.7	Real dataset RD50. Proportion of cumulative explained variance for PCAs computed from the 6 different centres, for different number of dimensions	169
6.8	Real dataset RD50. Errors e (equation 6.2) between the approximated distance matrices of each center and: i) the approximated matrix computed with IC1 (left columns); ii) the direct distance matrix (right columns).	170
6.9	Real dataset RD1000. Proportion of cumulative explained variance, for PCA, computed from IC1 for the whole dataset.	174

BIBLIOGRAPHY

- Afsari, B. (2011). Riemannian L^p center of mass: Existence, uniqueness, and convexity. *Proceedings of the American Mathematical Society*, 139(2), 655–673.
- Afsari, B., Tron, R., & Vidal, R. (2013). On the convergence of gradient descent for finding the Riemannian center of mass. *SIAM Journal on Control and Optimization*, 51(3), 2230–2260.
- Akhondi-Asl, A., Jafari-Khouzani, K., Elisevich, K., & Soltanian-Zadeh, H. (2011). Hippocampal volumetry for lateralization of temporal lobe epilepsy: automated versus manual methods. *Neuroimage*, 54, S218–S226.
- Alvarez, P. & Squire, L. R. (1994). Memory consolidation and the medial temporal lobe: a simple network model. *Proceedings of the National Academy of Sciences*, 91(15), 7041–7045.
- Ando, T., Li, C.-K., & Mathias, R. (2004). Geometric means. *Linear algebra and its applications*, 385, 305–334.
- Arnaudon, M., Dombry, C., Phan, A., & Yang, L. (2012). Stochastic algorithms for computing means of probability measures. *Stochastic Processes and their Applications*, 122(4), 1437–1455.
- Ashburner, J. & Friston, K. J. (2000). Voxel-based morphometry—the methods. *Neuroimage*, 11(6), 805–821.
- Auzias, G., Colliot, O., Glaunès, J. A., Perrot, M., Mangin, J., Trounev, A., & Baillet, S. (2011). Diffeomorphic Brain Registration Under Exhaustive Sulcal Constraints. *IEEE Transactions on Medical Imaging*.

- Auzias, G., Glaunès, J. A., Colliot, O., Perrot, M., Mangin, J.-F., Trouvé, A., & Baillet, S. (2009). DISCO: A Coherent Diffeomorphic Framework for Brain Registration under Exhaustive Sulcal Constraints. *Medical Image Computing and Computer-Assisted Intervention—MICCAI 2009*, (pp. 730–738).
- Bajic, D., Ewald, U., & Raininko, R. (2010). Hippocampal development at gestation weeks 23 to 36. An ultrasound study on preterm neonates. *Neuroradiology*, 52(6), 489–494. PMID: 20352419.
- Bajic, D., Kumlien, E., Mattsson, P., Lundberg, S., Wang, C., & Raininko, R. (2009). Incomplete hippocampal inversion—is there a relation to epilepsy? *European radiology*, 19(10), 2544–2550.
- Bajic, D., Wang, C., Kumlien, E., Mattsson, P., Lundberg, S., Eeg-Olofsson, O., & Raininko, R. (2008). Incomplete inversion of the hippocampus—a common developmental anomaly. *European radiology*, 18(1), 138–142. PMID: 17828540.
- Baker, L. & Barkovich, A. (1992). The large temporal horn: MR analysis in developmental brain anomalies versus hydrocephalus. *American journal of neuroradiology*, 13(1), 115–122.
- Barsi, P., Kenéz, J., Solymosi, D., Kulin, A., Halász, P., Rásonyi, G., Janszky, J., Kalóczkai, A., Barcs, G., Neuwirth, M., Paraicz, E., Siegler, Z., Morvai, M., Jerney, J., Kassay, M., & Altmann, A. (2000). Hippocampal malrotation with normal corpus callosum: a new entity? *Neuroradiology*, 42(5), 339–345.
- Bassett, A., Krings, T., Chow, E., Kiehl, T.-R., & Andrade, D. (2014). Hippocampal Malrotation Is Associated With Chromosome 22q11. 2 Microdeletion (S29. 006). *Neurology*, 82(10 Supplement), S29–006.
- Baulac, M., Grissac, N. D., Hasboun, D., Oppenheim, C., Adam, C., Arzimanoglou, A., Semah, F., Leheéricy, S., Clémenceau, S., & Berger, B. (1998). Hippocampal developmental changes in patients with partial epilepsy: Magnetic resonance imaging and clinical aspects. *Annals of Neurology*, 44(2), 223–233.
- Becker, B. G., Cosío, F. A., Huerta, M. E. G., & Benavides-Serralde, J. (2010). Automatic segmentation of the cerebellum of fetuses on 3D ultrasound images, using a 3D Point Distribution Model. In *Engineering in Medicine and Biology Society (EMBC), 2010 Annual International Conference of the IEEE* (pp. 4731–4734).: IEEE.

- Beg, M. F., Miller, M. I., Trouvé, A., & Younes, L. (2005). Computing large deformation metric mappings via geodesic flows of diffeomorphisms. *International Journal of Computer Vision*, 61(2), 139–157.
- Berchtold, N. C. & Cotman, C. W. (1998). Evolution in the conceptualization of dementia and Alzheimer's disease: Greco-Roman period to the 1960s. *Neurobiology of aging*, 19(3), 173–189.
- Bernasconi, N., Kinay, D., Andermann, F., Antel, S., & Bernasconi, A. (2005). Analysis of shape and positioning of the hippocampal formation: an MRI study in patients with partial epilepsy and healthy controls. *Brain*, 128(10), 2442–2452.
- Bis, J. C., DeCarli, C., Smith, A. V., van der Lijn, F., Crivello, F., Fornage, M., Dobbins, S., Shulman, J. M., Schmidt, H., Srikanth, V., et al. (2012). Common variants at 12q14 and 12q24 are associated with hippocampal volume. *Nature genetics*, 44(5), 545.
- Braae, A., Turton, J., Lord, J., Medway, C., Brown, K., Barber, I., & Morgan, K. (2014). Deep sequencing Alzheimer's disease associated genes, CLU, PICALM, CR1, ABCA7, BIN1, MS4A, CD2AP, EPHA1, and CD33 identifies potential functional SNPs. *Alzheimer's & Dementia: The Journal of the Alzheimer's Association*, 10(4), P322.
- Braak, H. & Braak, E. (1991). Neuropathological staging of Alzheimer-related changes. *Acta neuropathologica*, 82(4), 239–259.
- Bremner, J. D., Narayan, M., Anderson, E. R., Staib, L. H., Miller, H. L., & Charney, D. S. (2000). Hippocampal volume reduction in major depression. *American Journal of Psychiatry*, 157(1), 115–118.
- Bronen, R. A. & Cheung, G. (1991). MRI of the normal hippocampus. *Magnetic resonance imaging*, 9(4), 497–500.
- Burgess, N., Maguire, E. A., & O'Keefe, J. (2002). The Human Hippocampus and Spatial and Episodic Memory. *Neuron*, 35(4), 625–641.
- Charon, N. & Trouvé, A. (2013). The varifold representation of non-oriented shapes for diffeomorphic registration. *SIAM Journal on Imaging Sciences*.
- Christensen, G. E., Rabbitt, R. D., & Miller, M. I. (1996). Deformable templates using large deformation kinematics. *Image Processing, IEEE Transactions on*, 5(10), 1435–1447.

- Chupin, M., Hammers, A., Liu, R. S., Colliot, O., Burdett, J., Bardinet, E., Duncan, J. S., Garnero, L., & Lemieux, L. (2009). Automatic segmentation of the hippocampus and the amygdala driven by hybrid constraints: method and validation. *Neuroimage*, 46(3), 749–761.
- Collins, D. L. & Pruessner, J. C. (2010). Towards accurate, automatic segmentation of the hippocampus and amygdala from MRI by augmenting ANIMAL with a template library and label fusion. *Neuroimage*, 52(4), 1355–1366.
- Convit, A., De Leon, M., Tarshish, C., De Santi, S., Tsui, W., Rusinek, H., & George, A. (1997). Specific hippocampal volume reductions in individuals at risk for Alzheimer’s disease. *Neurobiology of aging*, 18(2), 131–138.
- Cootes, T. F., Taylor, C. J., Cooper, D. H., & Graham, J. (1995). Active shape models-their training and application. *Computer vision and image understanding*, 61(1), 38–59.
- Corkin, S. (2002). What’s new with the amnesic patient HM? *Nature Reviews Neuroscience*, 3(2), 153–160.
- Cox, T. F. & Cox, M. A. (2010). *Multidimensional scaling*. CRC Press.
- Crane, P. K., Carle, A., Gibbons, L. E., Insel, P., Mackin, R. S., Gross, A., Jones, R. N., Mukherjee, S., Curtis, S. M., Harvey, D., et al. (2012). Development and assessment of a composite score for memory in the Alzheimer’s Disease Neuroimaging Initiative (ADNI). *Brain imaging and behavior*, 6(4), 502–516.
- Csernansky, J., Wang, L., Swank, J., Miller, J., Gado, M., McKeel, D., Miller, M., & Morris, J. (2005). Preclinical detection of Alzheimer’s disease: hippocampal shape and volume predict dementia onset in the elderly. *Neuroimage*, 25(3), 783–792.
- Csernansky, J. G., Joshi, S., Wang, L., Haller, J. W., Gado, M., Miller, J. P., Grenander, U., & Miller, M. I. (1998). Hippocampal morphometry in schizophrenia by high dimensional brain mapping. *Proceedings of the National Academy of Sciences*, 95(19), 11406–11411.
- Cunningham, M. (2009). More than just the kappa coefficient: a program to fully characterize inter-rater reliability between two raters. In *SAS global forum* (pp. 242–2009).
- Cury, C., Glaunès, J. A., Chupin, M., Colliot, O., et al. (2014a). Fast Template-based Shape Analysis using Diffeomorphic Iterative Centroid. In *MIUA 2014-Medical Image Understanding and Analysis 2014* (pp. 39–44).

- Cury, C., Glaunès, J. A., & Colliot, O. (2013). Template Estimation for Large Database: A Diffeomorphic Iterative Centroid Method Using Currents. In F. Nielsen & F. Barbaresco (Eds.), *GSI2013 - Geometric Science of Information*, volume 8085 of *Lecture Notes in Computer Science* (pp. 103–111).: Springer.
- Cury, C., Glaunès, J. A., & Colliot, O. (2014b). Diffeomorphic Iterative Centroid Methods for Template Estimation on Large Datasets. In F. Nielsen (Ed.), *Geometric Theory of Information, Signals and Communication Technology* (pp. 273–299). Springer International Publishing.
- De Rham, G. (1955). Variétés différentiables. Formes, courants, formes harmoniques. *Actualités Sci. Ind.*, no. 1222, Publ. *Inst. Math. Univ. Nancago III., Hermann, Paris*.
- Dericioglu, N., Oguz, K. K., Soylemezoglu, F., Akalan, N., & Saygi, S. (2009). Resective surgery is possible in patients with temporal lobe epilepsy due to bilateral isolated hippocampal malformation. *Clinical neurology and neurosurgery*, 111(6), 554–557.
- Devanand, D., Pradhaban, G., Liu, X., Khandji, A., De Santi, S., Segal, S., Rusinek, H., Pelton, G., Honig, L., Mayeux, R., et al. (2007). Hippocampal and entorhinal atrophy in mild cognitive impairment Prediction of Alzheimer disease. *Neurology*, 68(11), 828–836.
- Donmez, F. Y., Yildirim, M., Erkek, N., Karacan, C. D., & Coskun, M. (2009). Hippocampal abnormalities associated with various congenital malformations. *Child's Nervous System*, 25(8), 933–939.
- Donoho, D. L. & Grimes, C. (2003). Hessian eigenmaps: Locally linear embedding techniques for high-dimensional data. *Proceedings of the National Academy of Sciences*, 100(10), 5591–5596.
- D’Arcy Thompson, W. (1917). *On growth and form*. Cambridge Univ Press.
- Dryden, I. L. & Mardia, K. V. (1998). *Statistical shape analysis*, volume 4. John Wiley & Sons New York.
- Duman, R. S., Heninger, G. R., & Nestler, E. J. (1997). A molecular and cellular theory of depression. *Archives of general psychiatry*, 54(7), 597–606.
- Durrleman, S. (2010). *Statistical models of currents for measuring the variability of anatomical curves, surfaces and their evolution*. PhD thesis, University of Nice-Sophia Antipolis.

- Durrleman, S., Pennec, X., Trouvé, A., & Ayache, N. (2009). Statistical models of sets of curves and surfaces based on currents. *Medical Image Analysis*, 13(5), 793–808.
- Durrleman, S., Pennec, X., Trouvé, A., Ayache, N., et al. (2008a). A forward model to build unbiased atlases from curves and surfaces. In *2nd Medical Image Computing and Computer Assisted Intervention. Workshop on Mathematical Foundations of Computational Anatomy* (pp. 68–79).
- Durrleman, S., Pennec, X., Trouvé, A., Thompson, P., & Ayache, N. (2008b). Inferring brain variability from diffeomorphic deformations of currents: an integrative approach. *Medical image analysis*, 12(5), 626–637.
- Durrleman, S., Prastawa, M., Korenberg, J. R., Joshi, S., Trouvé, A., & Gerig, G. (2012). Topology Preserving Atlas Construction from Shape Data without Correspondence Using Sparse Parameters. In N. Ayache, H. Delingette, P. Golland, & K. Mori (Eds.), *Medical Image Computing and Computer-Assisted Intervention – MICCAI 2012*, volume 7512 of *Lecture Notes in Computer Science* (pp. 223–230). Springer Berlin Heidelberg.
- Duvernoy, H. (1999). *The Human Brain: Surface, Three-Dimensional Sectional Anatomy and MRI*. Springer Verlag, Wien.
- Duvernoy, H. (2005). *The Human Hippocampus: Functional Anatomy, Vascularization and Serial Sections with MRI*. Springer Verlag, Berlin.
- Ekstrom, A. D., Kahana, M. J., Caplan, J. B., Fields, T. A., Isham, E. A., Newman, E. L., & Fried, I. (2003). Cellular networks underlying human spatial navigation. *Nature*, 425(6954), 184–188.
- Emery, M. & Mokobodzki, G. (1991). Sur le barycentre d’une probabilité dans une variété. In *Séminaire de probabilités*, volume 25 (pp. 220–233): Springer Berlin Heidelberg.
- Engel Jr, J. (1996). Introduction to temporal lobe epilepsy. *Epilepsy research*, 26(1), 141–150.
- Eriksson, P. S., Perfilieva, E., Björk-Eriksson, T., Alborn, A.-M., Nordborg, C., Peterson, D. A., & Gage, F. H. (1998). Neurogenesis in the adult human hippocampus. *Nature medicine*, 4(11), 1313–1317.

- Eriksson, S. H., Thom, M., Bartlett, P. A., Symms, M. R., McEvoy, A. W., Sisodiya, S. M., & Duncan, J. S. (2008). PROPELLER MRI visualizes detailed pathology of hippocampal sclerosis. *Epilepsia*, 49(1), 33–39.
- Fischl, B., Salat, D. H., Busa, E., Albert, M., Dieterich, M., Haselgrove, C., van der Kouwe, A., Killiany, R., Kennedy, D., Klaveness, S., et al. (2002). Whole brain segmentation: automated labeling of neuroanatomical structures in the human brain. *Neuron*, 33(3), 341–355.
- Friedman, E. R. & Tandon, N. (2013). Beyond Mesial Temporal Sclerosis: Optimizing MRI Evaluation in Focal Epilepsy. *Neurographics*, 3(2), 60–69.
- Gamss, R. P., Slasky, S. E., Bello, J. A., Miller, T. S., & Shinnar, S. (2009). Prevalence of hippocampal malrotation in a population without seizures. *AJNR Am J Neuroradiol*, 30(8), 1571–3.
- Gerardin, E., Chételat, G., Chupin, M., Cuingnet, R., Desgranges, B., Kim, H.-S., Niethammer, M., Dubois, B., Lehericy, S., Garnero, L., et al. (2009). Multidimensional classification of hippocampal shape features discriminates Alzheimer’s disease and mild cognitive impairment from normal aging. *Neuroimage*, 47(4), 1476–1486.
- Glaunès, J. A. (2005). *Transport par difféomorphismes de points, de mesures et de courants pour la comparaison de formes et l’anatomie numérique*. PhD thesis, Université Paris 13.
- Glaunès, J. A. & Joshi, S. (2006). Template estimation from unlabeled point set data and surfaces for Computational Anatomy. In X. Pennec & S. Joshi (Eds.), *Proc. of the International Workshop on the Mathematical Foundations of Computational Anatomy (MFCA-2006)* (pp. 29–39).
- Glaunès, J. A., Troune, A., & Younes, L. (2004). Diffeomorphic matching of distributions: a new approach for unlabelled point-sets and sub-manifolds matching. In *Computer Vision and Pattern Recognition, 2004. CVPR 2004. Proceedings of the 2004 IEEE Computer Society Conference on*, volume 2 (pp. II–712–II–718 Vol.2).
- Gori, P., Colliot, O., Worbe, Y., Marrakchi-Kacem, L., Lecomte, S., Poupon, C., Hartmann, A., Ayache, N., & Durrleman, S. (2013). Bayesian Atlas Estimation for the Variability Analysis of Shape Complexes. In *MICCAI 2013 - 16th International Conference on Medical Image Computing and Computer Assisted Intervention* (pp. P1–21). Nagoya, Japan. To appear.

- Grenander, U. (1995). General pattern theory: a mathematical theory of regular structures. *Journal of the Royal Statistical Society-Series A Statistics in Society*, 158(3), 629.
- Grenander, U. & Miller, M. I. (1998). Computational anatomy: An emerging discipline. *Quarterly of applied mathematics*, 56(4), 617–694.
- Hänggi, J., Streffer, J., Jäncke, L., & Hock, C. (2011). Volumes of lateral temporal and parietal structures distinguish between healthy aging, mild cognitive impairment, and Alzheimer’s disease. *Journal of Alzheimer’s Disease*, 26(4), 719–734.
- Hanke, J. (1997). Sulcal pattern of the anterior parahippocampal gyrus in the human adult. *Annals of Anatomy-Anatomischer Anzeiger*, 179(4), 335–339.
- Hastie, T., Tibshirani, R., Friedman, J., Hastie, T., Friedman, J., & Tibshirani, R. (2009). *The elements of statistical learning*. Springer.
- Hogan, R. E., Moseley, E. D., & Maccotta, L. (2014). Hippocampal Surface Deformation Accuracy in T1-Weighted Volumetric MRI Sequences in Subjects with Epilepsy. *Journal of Neuroimaging*.
- Humphrey, T. (1967). The development of the human hippocampal fissure. *Journal of anatomy*, 101(Pt 4), 655.
- Huntgeburth, S. C. & Petrides, M. (2012). Morphological patterns of the collateral sulcus in the human brain. *European Journal of Neuroscience*, 35(8), 1295–1311.
- Insausti, R., Tunon, T., Sobreviela, T., Insausti, A., & Gonzalo, L. (1995). The human entorhinal cortex: a cytoarchitectonic analysis. *Journal of Comparative Neurology*, 355(2), 171–198.
- Jenkinson, M., Bannister, P., Brady, M., & Smith, S. (2002). Improved optimization for the robust and accurate linear registration and motion correction of brain images. *Neuroimage*, 17(2), 825–841.
- Jenkinson, M. & Smith, S. (2001). A global optimisation method for robust affine registration of brain images. *Medical image analysis*, 5(2), 143–156.
- Karcher, H. (1977). Riemannian center of mass and mollifier smoothing. *Communications on pure and applied mathematics*, 30(5), 509–541.

- Kendall, W. S. (1990). Probability, convexity, and harmonic maps with small image I: uniqueness and fine existence. *Proceedings of the London Mathematical Society*, 3(2), 371–406.
- Kier, E. L., Fulbright, R. K., & Bronen, R. A. (1995). Limbic lobe embryology and anatomy: dissection and MR of the medial surface of the fetal cerebral hemisphere. *American journal of neuroradiology*, 16(9), 1847–1853.
- Kier, E. L., Kim, J. H., Fulbright, R. K., & Bronen, R. A. (1997). Embryology of the human fetal hippocampus: MR imaging, anatomy, and histology. *American journal of neuroradiology*, 18(3), 525–532.
- Kim, H., Bernasconi, N., Bernhardt, B., Colliot, O., & Bernasconi, A. (2008). Basal temporal sulcal morphology in healthy controls and patients with temporal lobe epilepsy. *Neurology*, 70(22 Pt 2), 2159–2165. PMID: 18505994.
- Kim, H., Chupin, M., Colliot, O., Bernhardt, B. C., Bernasconi, N., & Bernasconi, A. (2012). Automatic hippocampal segmentation in temporal lobe epilepsy: impact of developmental abnormalities. *Neuroimage*, 59(4), 3178–3186.
- Laakso, M., Soininen, H., Partanen, K., Helkala, E.-L., Hartikainen, P., Vainio, P., Hallikainen, M., Hänninen, T., & Riekkinen Sr, P. (1995). Volumes of hippocampus, amygdala and frontal lobes in the MRI-based diagnosis of early Alzheimer's disease: correlation with memory functions. *Journal of Neural Transmission-Parkinson's Disease and Dementia Section*, 9(1), 73–86.
- Le, H. (2004). Estimation of Riemannian barycentres. *LMS J. Comput. Math*, 7, 193–200.
- Lehéricy, S., Dormont, D., Sémah, F., Clémenceau, S., Granat, O., Marsault, C., & Baulac, M. (1995). Developmental abnormalities of the medial temporal lobe in patients with temporal lobe epilepsy. *AJNR. American journal of neuroradiology*, 16(4), 617–626.
- Lorente de Nó, R. (1934). Studies on the structure of the cerebral cortex. II. Continuation of the study of the ammonic system. *Journal für Psychologie und Neurologie*.
- Ma, J., Miller, M. I., Trouvé, A., & Younes, L. (2008). Bayesian template estimation in computational anatomy. *NeuroImage*, 42(1), 252–261.
- Maguire, E. A. (2001). Neuroimaging studies of autobiographical event memory. *Philosophical Transactions of the Royal Society of London. Series B: Biological Sciences*, 356(1413), 1441–1451.

- Maguire, E. A., Gadian, D. G., Johnsrude, I. S., Good, C. D., Ashburner, J., Frackowiak, R. S., & Frith, C. D. (2000). Navigation-related structural change in the hippocampi of taxi drivers. *Proceedings of the National Academy of Sciences*, 97(8), 4398–4403.
- Mangin, J.-F., Poupon, F., Duchesnay, É., Rivière, D., Cachia, A., Collins, D. L., Evans, A. C., & Régis, J. (2004). Brain morphometry using 3D moment invariants. *Medical Image Analysis*, 8(3), 187–196.
- Mansi, T., Voigt, I., Leonardi, B., Pennec, X., Durrleman, S., Sermesant, M., Delingette, H., Taylor, A. M., Boudjemline, Y., Pongiglione, G., et al. (2011). A statistical model for quantification and prediction of cardiac remodelling: Application to tetralogy of fallot. *Medical Imaging, IEEE Transactions on*, 30(9), 1605–1616.
- Michaelson, D. M. (2014). ApoE4: The most prevalent yet understudied risk factor for Alzheimer’s disease. *Alzheimer’s & Dementia*.
- Minkel, J. (2007). Brain pathway may underlie depression: a crescent of electrical activity spotted in rats may allow researchers to map the depressed brain. *Scientific American Mind News*.
- Nadel, L. & Moscovitch, M. (2001). The hippocampal complex and long-term memory revisited. *Trends in cognitive sciences*, 5(6), 228–230.
- Nadel, L., Samsonovich, A., Ryan, L., & Moscovitch, M. (2000). Multiple trace theory of human memory: computational, neuroimaging, and neuropsychological results. *Hippocampus*, 10(4), 352–368.
- Nelson, M. D., Saykin, A. J., Flashman, L. A., & Riordan, H. J. (1998). Hippocampal volume reduction in schizophrenia as assessed by magnetic resonance imaging: a meta-analytic study. *Archives of general psychiatry*, 55(5), 433–440.
- Novak, K., Czech, T., Prayer, D., Dietrich, W., Serles, W., Lehr, S., & Baumgartner, C. (2002). Individual variations in the sulcal anatomy of the basal temporal lobe and its relevance for epilepsy surgery: an anatomical study performed using magnetic resonance imaging. *Journal of neurosurgery*, 96(3), 464–473.
- O’Dwyer, L., Lamberton, F., Matura, S., Tanner, C., Scheibe, M., Miller, J., Rujescu, D., Prvulovic, D., & Hampel, H. (2012). Reduced hippocampal volume in healthy young ApoE4 carriers: an MRI study. *PloS one*, 7(11), e48895.

- Okada, Y., Kato, T., Iwai, K., Iwasaki, N., Ohto, T., & Matsui, A. (2003). Evaluation of hippocampal infolding using magnetic resonance imaging. *Neuroreport*, 14(10), 1405.
- O'Keefe, J. & Dostrovsky, J. (1971). The hippocampus as a spatial map. Preliminary evidence from unit activity in the freely-moving rat. *Brain research*, 34(1), 171–175.
- Ong, D., Walterfang, M., Malhi, G. S., Styner, M., Velakoulis, D., & Pantelis, C. (2012). Size and shape of the caudate nucleus in individuals with bipolar affective disorder. *Australian and New Zealand Journal of Psychiatry*, 46(4), 340–351.
- Ono, M., Kubik, S., Abernathy, C. D., et al. (1990). *Atlas of the cerebral sulci*. Thieme.
- Pardoe, H. R., Pell, G. S., Abbott, D. F., & Jackson, G. D. (2009). Hippocampal volume assessment in temporal lobe epilepsy: how good is automated segmentation? *Epilepsia*, 50(12), 2586–2592.
- Parent, J. M., Timothy, W. Y., Leibowitz, R. T., Geschwind, D. H., Sloviter, R. S., & Lowenstein, D. H. (1997). Dentate granule cell neurogenesis is increased by seizures and contributes to aberrant network reorganization in the adult rat hippocampus. *The Journal of Neuroscience*, 17(10), 3727–3738.
- Peltier, B., Hurtevent, P., Trehan, G., Derambure, P., Pruvo, J.-P., & Soto-Ares, G. (2005). IRM des malformations de l'hippocampe dans l'épilepsie temporale réfractaire. *neuroradiologie*, 86, 69–75. *Journal de radiologie - Vol. 86 - N° 1-C1 - p. 69-75.*
- Penec, X. (2006). Intrinsic statistics on Riemannian manifolds: Basic tools for geometric measurements. *Journal of Mathematical Imaging and Vision*, 25(1), 127–154.
- Pizer, S. M., Fritsch, D. S., Yushkevich, P. A., Johnson, V. E., & Chaney, E. L. (1999). Segmentation, registration, and measurement of shape variation via image object shape. *Medical Imaging, IEEE Transactions on*, 18(10), 851–865.
- Pouch, A. M., Yushkevich, P. A., Jackson, B. M., Jassar, A. S., Vergnat, M., Gorman, J. H., Gorman, R. C., & Sehgal, C. M. (2012). Development of a semi-automated method for mitral valve modeling with medial axis representation using 3D ultrasound. *Medical physics*, 39(2), 933–950.

- Radoš, M., Judaš, M., & Kostović, I. (2006). In vitro MRI of brain development. *European journal of radiology*, 57(2), 187–198.
- Raininko, R. & Bajic, D. (2010). Hippocampal Malrotation: No Real Malrotation and Not Rare. *American Journal of Neuroradiology*, 31(4), E39–E39.
- Righini, A., Zirpoli, S., Parazzini, C., Bianchini, E., Scifo, P., Sala, C., & Triulzi, F. (2006). Hippocampal infolding angle changes during brain development assessed by prenatal MR imaging. *American journal of neuroradiology*, 27(10), 2093–2097.
- Rosenbaum, R. S., Köhler, S., Schacter, D. L., Moscovitch, M., Westmacott, R., Black, S. E., Gao, F., & Tulving, E. (2005). The case of KC: contributions of a memory-impaired person to memory theory. *Neuropsychologia*, 43(7), 989–1021.
- Roweis, S. T. & Saul, L. K. (2000). Nonlinear dimensionality reduction by locally linear embedding. *Science*, 290(5500), 2323–2326.
- Rueckert, D., Sonoda, L. I., Hayes, C., Hill, D. L., Leach, M. O., & Hawkes, D. J. (1999). Nonrigid registration using free-form deformations: application to breast MR images. *Medical Imaging, IEEE Transactions on*, 18(8), 712–721.
- Sato, N., Hatakeyama, S., Shimizu, N., Hikima, A., Aoki, J., & Endo, K. (2001). MR evaluation of the hippocampus in patients with congenital malformations of the brain. *American journal of neuroradiology*, 22(2), 389–393.
- Schölkopf, B., Smola, A., & Müller, K.-R. (1997). Kernel principal component analysis. In *Artificial Neural Networks—ICANN'97* (pp. 583–588). Springer.
- Schumann, G., Loth, E., Banaschewski, T., Barbot, A., Barker, G., Büchel, C., Conrod, P., Dalley, J., Flor, H., Gallinat, J., consortium, t. I., et al. (2010). The IMAGEN study: reinforcement-related behaviour in normal brain function and psychopathology. *Molecular psychiatry*, 15(12), 1128–1139.
- Schwartz, L. (1952). Théorie des distributions. *Bull. Amer. Math. Soc.*, 58, 78–85.
- Scoville, W. B. & Milner, B. (1957). Loss of recent memory after bilateral hippocampal lesions. *Journal of neurology, neurosurgery, and psychiatry*, 20(1), 11.
- Sederberg, T. W. & Parry, S. R. (1986). Free-form deformation of solid geometric models. In *ACM Siggraph Computer Graphics*, volume 20 (pp. 151–160): ACM.

- Semah, F., Picot, M.-C., Adam, C., Broglin, D., Arzimanoglou, A., Bazin, B., Cavalcanti, D., & Baulac, M. (1998). Is the underlying cause of epilepsy a major prognostic factor for recurrence? *Neurology*, 51(5), 1256–1262.
- Sheline, Y. I., Gado, M. H., & Kraemer, H. C. (2003). Untreated depression and hippocampal volume loss. *American Journal of Psychiatry*, 160(8), 1516–1518.
- Sheline, Y. I., Wang, P. W., Gado, M. H., Csernansky, J. G., & Vannier, M. W. (1996). Hippocampal atrophy in recurrent major depression. *Proceedings of the National Academy of Sciences*, 93(9), 3908–3913.
- Shen, K.-k., Fripp, J., Mériaudeau, F., Chételat, G., Salvado, O., & Bourgeat, P. (2012). Detecting global and local hippocampal shape changes in Alzheimer's disease using statistical shape models. *Neuroimage*, 59(3), 2155–2166.
- Shenton, M. E., Kikinis, R., Jolesz, F. A., Pollak, S. D., LeMay, M., Wible, C. G., Hokama, H., Martin, J., Metcalf, D., Coleman, M., et al. (1992). Abnormalities of the left temporal lobe and thought disorder in schizophrenia: a quantitative magnetic resonance imaging study. *New England Journal of Medicine*, 327(9), 604–612.
- Shi, Y., Thompson, P. M., de Zubicaray, G. I., Rose, S. E., Tu, Z., Dinov, I., & Toga, A. W. (2007). Direct mapping of hippocampal surfaces with intrinsic shape context. *NeuroImage*, 37(3), 792–807.
- Smith, S. M., Jenkinson, M., Woolrich, M. W., Beckmann, C. F., Behrens, T. E., Johansen-Berg, H., Bannister, P. R., De Luca, M., Drobnjak, I., Flitney, D. E., et al. (2004). Advances in functional and structural MR image analysis and implementation as FSL. *Neuroimage*, 23, S208–S219.
- Spencer, S. S., Spencer, D. D., Williamson, P. D., & Mattson, R. (1990). Combined depth and subdural electrode investigation in uncontrolled epilepsy. *Neurology*, 40(1), 74–74.
- Squire, L. R. (2009). The Legacy of Patient HM for Neuroscience. *Neuron*, 61(1), 6.
- Stiers, P., Fonteyne, A., Wouters, H., D'Agostino, E., Sunaert, S., & Lagae, L. (2010). Hippocampal malrotation in pediatric patients with epilepsy associated with complex prefrontal dysfunction. *Epilepsia*, 51(4), 546–555.

- Styner, M., Lieberman, J. A., Pantazis, D., & Gerig, G. (2004). Boundary and medial shape analysis of the hippocampus in schizophrenia. *Medical image analysis*, 8(3), 197–203.
- Tangelder, J. W. & Veltkamp, R. C. (2008). A survey of content based 3D shape retrieval methods. *Multimedia tools and applications*, 39(3), 441–471.
- Tenenbaum, J., Silva, V., & Langford, J. (2000). A Global Geometric Framework for Nonlinear Dimensionality Reduction. *Science*, 290(5500), 2319–2323.
- Tepest, R., Wang, L., Miller, M. I., Falkai, P., & Csernansky, J. G. (2003). Hippocampal deformities in the unaffected siblings of schizophrenia subjects. *Biological psychiatry*, 54(11), 1234–1240.
- Trouvé, A. (1998). Diffeomorphisms Groups and Pattern Matching in Image Analysis. *International Journal of Computer Vision*, 28(3), 213–221.
- Tulving, E. (1995). Organization of memory: Quo vadis. *The cognitive neurosciences*.
- Tulving, E. (2002). Episodic memory: from mind to brain. *Annual review of psychology*, 53(1), 1–25.
- Vaillant, M. & Glaunès, J. A. (2005). Surface matching via currents. In *Information Processing in Medical Imaging* (pp. 381–392).: Springer.
- Vaillant, M., Miller, M. I., Younes, L., & Trouvé, A. (2004). Statistics on diffeomorphisms via tangent space representations. *NeuroImage*, 23, S161–S169.
- Vargha-Khadem, F., Gadian, D. G., Watkins, K. E., Connelly, A., Van Paesschen, W., & Mishkin, M. (1997). Differential effects of early hippocampal pathology on episodic and semantic memory. *Science*, 277(5324), 376–380.
- Von Luxburg, U. (2007). A tutorial on spectral clustering. *Statistics and computing*, 17(4), 395–416.
- Wang, L., Beg, F., Ratnanather, T., Ceritoglu, C., Younes, L., Morris, J. C., Csernansky, J. G., & Miller, M. I. (2007a). Large deformation diffeomorphism and momentum based hippocampal shape discrimination in dementia of the Alzheimer type. *Medical Imaging, IEEE Transactions on*, 26(4), 462–470.

- Wang, L., Lee, D. Y., Bailey, E., Hartlein, J. M., Gado, M. H., Miller, M. I., & Black, K. J. (2007b). Validity of large-deformation high dimensional brain mapping of the basal ganglia in adults with Tourette syndrome. *Psychiatry Research: Neuroimaging*, 154(2), 181–190.
- Warrington, E. K. (1975). The selective impairment of semantic memory. *The Quarterly journal of experimental psychology*, 27(4), 635–657.
- Wheeler, M. A., Stuss, D. T., & Tulving, E. (1997). Toward a theory of episodic memory: the frontal lobes and autonoetic consciousness. *Psychological bulletin*, 121(3), 331.
- Wiebe, S. (2003). Brain surgery for epilepsy. *The Lancet*, 362, 48–49.
- Wiebe, S., Blume, W. T., Girvin, J. P., & Eliasziw, M. (2001). A randomized, controlled trial of surgery for temporal-lobe epilepsy. *New England Journal of Medicine*, 345(5), 311–318.
- Yang, X., Goh, A., & Qiu, A. (2011a). Locally Linear Diffeomorphic Metric Embedding (LLDME) for surface-based anatomical shape modeling. *neuroimage*, 56(1), 149–161.
- Yang, X. F., Goh, A., & Qiu, A. (2011b). Approximations of the Diffeomorphic Metric and Their Applications in Shape Learning. In *Information Processing in Medical Imaging:IPMI* (pp. 257–270).
- Zhang, Z.-y. & Zha, H.-y. (2004). Principal manifolds and nonlinear dimensionality reduction via tangent space alignment. *Journal of Shanghai University (English Edition)*, 8(4), 406–424.

RESUME

Statistical shape analysis of anatomical structures is a key challenge for many applications: modelling of the normal and pathological variability, prediction of clinical or biological parameters from anatomical data... Recent years have seen the emergence of large databases in neuro-imaging, potentially increasing the statistical power of new studies.

This thesis is about the statistical analysis of the anatomical variability of hippocampi in large populations. After a state of the art, the first part of the thesis focuses on the study of an anatomical variant named Incomplete Hippocampal Inversion (IHI). We developed a new robust scale for IHI assessments. We then applied the evaluation to 2000 young healthy subjects from the European database IMAGEN. Results show that IHI are frequent on healthy population, with a left side predominance. This is the first time that IHI are studied on a large database composed of healthy subjects.

The second part of this thesis develops a method for the statistical analysis of shapes based on Large Diffeomorphic Deformations Metric Mapping and mathematical currents, applicable for the analysis of large datasets. In particular we have introduced a new fast approach for the estimation of anatomical templates. This approach has been validated on 1000 young healthy subjects of the IMAGEN database and on 294 subjects from the ADNI database (healthy ageing subjects and patients with Alzheimer disease). Results show that the method allows the modelling of the anatomical variability of hippocampi with a reasonable number of dimensions.